Characterization of a new pixelated diamond detector for fast neutron diagnostics on fusion reactors

Ph.D. Thesis

Antonella Tamburrino

Advisor   Co-Advisor

Prof. Renato Gatto   Dr. Gerardo Claps

A.A. 2022-2023

Contents

ABSTRACT

This research activity focuses on characterizing an innovative pixelated diamond detector utilizing Timepix3 (TPX3) chip technology. This detector combines a polycrystalline diamond with the TPX3 chip. Future versions will feature a monocrystalline diamond covering a 14 × 14 mm² area, achieving a remarkable spatial resolution of 55 μm. The TPX3 chip empowers pixel-wise simultaneous counting, charge measurement, and time recording, enabling precise monitoring of neutron interactions within the diamond, which are manifested as tracks. This capability proves invaluable for multiparametric analysis along a designated line of sight in a Tokamak machine. This is a central objective of this research. We aim to investigate the detector's response to neutrons within the 1-20 MeV energy range, which is critically relevant in nuclear fusion. Furthermore, TPX3's capacity to discriminate against signals from intense background sources, primarily gamma rays and scattered neutrons, is of paramount importance for designing diagnostic systems and the interpretation of data. Equally significant is the detector's ability to capture the temporal evolution of neutron emissions, offering real-time monitoring prospects that can be seamlessly integrated into feedback systems. A pivotal facet of this research involves the development of an algorithm. This algorithm, informed by laboratory measurements and Monte Carlo simulations, elucidates the distribution of pixel patterns generated in the diamond by primary neutron reactions. Its application to experimental data will facilitate the determination of the neutron spectrum. Specifically, the thesis is organized as follows. The first two chapters introduce the scientific context in which this research unfolds, presenting essential insights into the fundamental properties of neutron emissions from fusion plasmas. Chapter 3 reviews neutron detection systems, focusing on the Timepix3 detector. Its unique capabilities are showcased through two applications: radon decay product and thermal neutron

monitoring using a ^{6}LiF converter. These applications highlight the potential of these detectors as track detectors, particularly their ability to discriminate particles through morphological track analysis. Chapter 4 provides a comprehensive overview of the Diamondpix detector. The chapter discusses the properties of diamonds and presents the results of characterization studies of the Diamondpix detector. Finally, in Chapter 5, the potential of Diamondpix as a detector for fast neutrons is explored. Measurements were conducted at FNG (ENEA Frascati) and n_TOF (CERN). At FNG, the response of Diamondpix to 2.5 and 14 MeV neutrons from D-D and D-T reactions was characterized. The neutron efficiency at the two energies was also estimated. At n_TOF, time-of-flight measurements with Diamondpix were performed. Track analysis was carried out at different neutron energies, and Diamondpix was energy calibrated. The Diamondpix charge response was analyzed, and the FNG and n_TOF results were compared. Charge profiles were analyzed and compared with Monte Carlo simulations.

Chapter 1

Introduction and scientific context

1.1 Nuclear fusion and environmental sustainability

The present research work is placed in the highly topical and prospective context of studies on controlled thermonuclear fusion. In particular, first experimental evidence of nuclear fusion was obtained in the 1920s when the astronomer Arthur Eddington put forward the hypothesis that the energy emanating from the Sun was due to fusion reactions [1], and in 1929, the physicists Atkinson and Houtermans, in agreement with the equivalence between mass and energy postulated by A. Einstein in 1905, predicted that from the fusion of light nuclei, (for example hydrogen) a large amount of energy would be obtained [2]. In the 1930s, scientists also began to consider the possibility of obtaining energy from nuclear fusion on Earth. Starting from Ernest Rutherford's experiments on nuclear transmutation, Mark Oliphant achieved for the first time the fusion of heavy hydrogen isotopes in laboratories in 1932 up to the quantitative elaboration of the theory of thermonuclear fusion developed by the physicist H.A. Bethe [3]. Furthermore, following the first nuclear explosions (A-bomb and H-bomb) with the production of fusion energy in an explosive, i.e., uncontrolled form, research on controlled thermonuclear fusion began. It was in the 1950s that thermonuclear fusion began to be perceived as a potential source of clean energy. However, research on nuclear fusion energy for peaceful purposes immediately highlighted the great difficulty in being able to create the right conditions for such fusion reactions to occur with a sufficiently high frequency to be able to use the energy produced, lacking on earth the enormous force of gravity which characterizes the interior of the sun and stars, where a gas of light nuclei is confined with very high density and temperatures (the fourth state of matter: plasma) [4]. The research, therefore, focused on alternative

confinement schemes to the gravitational one, identifying the two paths of inertial and magnetic confinement. The production of energy through nuclear fusion reactions provides an essential boost to research, the ultimate goal of which is constructing a fusion reactor that can produce electricity to be fed into the network. This type of energy is fed with readily available fuel. It has a low environmental impact: it does not produce pollution gases (SO_2, NO_2), greenhouse effect (due to emission of CO_2 and CO), and direct radioactive nuclear waste with a long decay time. Finally, a fusion reactor would operate in entirely safe conditions without the risk of a severe accident (no uncontrolled reaction). For these reasons, fusion energy is a candidate as a critical element in the energy transition process currently underway.

1.2 Nuclear fusion for energy production

Nuclear fusion is a form of nuclear energy that involves the fusion of light elements, primarily hydrogen (H), and its isotopes deuterium (D) and tritium (T). Thanks to the high energy yield of these nuclear reactions, the main interest in nuclear fusion concerns the efficient energy production that can contribute to the worldwide energy supply. However, there are still challenges to be faced. It will be necessary to find concrete solutions to the leading scientific, engineering, and economic limitations inherent in the fusion process and integrate them into an economically competitive power plant. In particular, to provide the fusion reaction between deuterium and tritium, the two nuclei must overcome the Coulomb electrostatic repulsive force and reach a minimal distance of about 10^{-12} cm [5]. Then, it is necessary to supply the colliding nuclei with kinetic energy to exceed the Coulomb barrier and obtain an optimal fusion rate. The choice of fuel for fusion is limited to hydrogen isotopes since the plasma, which will be discussed in more detail below, does not constitute a stable system but loses energy through various mechanisms, among which the energy loss due to Bremsstrahlung and the power (P_{br}) lost due to radiation emission that is proportional to the square of the atomic number. Other nuclei give rise to much higher

P_{br} values and have a smaller fusion cross-section due to a high Z value and a higher Coulomb barrier. Therefore, to ensure that the thermal energy is sufficient to have a high probability that the two light nuclei can collide with the right energy, the currently pursued approach consists of heating the fuel to provide the appropriate kinetic energy to the nuclei. In these conditions, the fuel reaches the plasma state: a mixture of positively charged ions and negatively charged electrons that move independently and are dominated by electromagnetic forces.

As a consequence, the plasma must be confined for a long enough time with very high temperatures (10^8 K). To confine the plasma, the best solution is represented by tokamak machines that use intense magnetic fields. In addition, the constituent materials of these machines must be able to withstand the intense radiation and heat produced by the fusion reactions. Furthermore, the main environmental issue of fusion is that it produces high-energy neutrons as a byproduct of both the DD and DT reactions; these neutrons are captured in the fusion blanket, but when they pass through the structural material on their way to the blanket, the neutrons can induce activation of elements in structural material. However, radiation protection issues are limited to structural materials, and no radioactive wastes are produced during the life of the fusion reactor. As a consequence, the environmental impact of fusion is severely reduced, and the potential benefits of fusion from the point of view of fuel reserves and safety are undoubtedly significant. In particular, two main reactions of interest involve pure deuterium and an equal mixing of D and T; D is present in enormous abundance in seawater (1 atom of deuterium every 6700 atoms of hydrogen) and can be easily extracted at a meager cost. At the same time, as far as tritium is concerned, since it is a radioactive isotope with a half-life of only about 12 years, there is no natural tritium on Earth [6]. However, it can be produced artificially from Lithium, for example, using the neutrons produced by the D-T fusion reaction. In conclusion, despite the difficulties, the possibility of using fusion to produce energy is currently the subject of intense study and research.

The critical part of the nuclear fusion plant is represented by diagnostic systems that allow monitoring of the fundamental physical processes essential to the correct behavior of the plasma and, therefore, of the reactor. The present research project focuses on the field of nuclear fusion technologies that are dedicated to neutron monitoring. In particular, different types of neutron detectors are used to measure the fast component or the thermal components of the neutron spectrum coming from the burning plasma. Among the various types of neutron diagnostics, diamond detectors play an essential role, and the object of this research work is devoted to implementing and characterizing a new diamond detector.

Chapter 2

Fusion plasma in magnetic confinement reactors

2.1 Introduction to fusion plasma

At the temperatures necessary to trigger the fusion reactions, the atoms are ionized (the ionization energy of a hydrogen atom is 13.6 eV) [7]. Therefore, the fuel is a hot "cloud" called plasma. In 1947, a team of scientists led by James Tuck created the first (entirely unstable) plasma jet in a torus-shaped high-vacuum glass vessel at the Imperial College London laboratories; in 1950, the Soviet physicists I. Tamm and A. Sakharov proposed the tokamak, a magnetic confinement fusion device. In particular, the T-3 tokamak, the first larger and more powerful version of the tokamak, was built in 1964 [8]. In 1968, at the conference held in Novosibirsk, it was announced that the T-3 tokamak had reached a temperature of 10 million degrees Celsius, producing electron temperatures of 1000 eV and confinement time at least 50 times the Bohm limit, demonstrating the potential of fusion energy exploitation [9].

The plasma state is the fourth state of matter: heating a gas makes a plasma. The word plasma comes from the Greek "πλάσμα", meaning "something formed or molded," and it was introduced to describe ionized gases by Tonks and Langmuir. More than 99% of the known universe is in the plasma state [10]. In its simple treatment, a plasma is composed of equal numbers of ions and electrons, each with an average density of n (particles per cubic cm). Plasma is a partially or fully ionized gas; however, weakly ionized gases behave very similarly to fully ionized ones, and if the ionization is larger than 1%, a medium behaves more like a plasma than a gas. Then, it is a globally neutral set of positive (ions) and negative (electrons) charges, and it is subject to collective

behavior. Currently, two schemes for plasma confinement are being pursued. Fusion plasmas can be divided into two types: those produced by the compression of small fuel capsules containing light ions through a set of high-power lasers (inertial fusion confinement) and those confined by strong magnetic fields created around appropriate containing vessels like tokamaks or stellarators (fusion magnetic confinement). This work is focused on the neutron diagnostic on magnetically confined plasma. Because a fusion plasma, as mentioned above, is a fully ionized gas, its behavior is primarily influenced by long-range electric and magnetic fields rather than Coulomb-type collisions between nearby particles. This makes the plasma a very efficient conductor of electricity and allows confinement by magnetic fields in a fusion reactor. At high temperatures and low densities, Coulomb-type collisions between electrons and ions are rare, resulting in low resistance to current flow and allowing the interaction with continuous external magnetic fields. It is, therefore, precisely the action of these fields that ensures the confinement of the plasma. Over the years, several configurations to realize a fusion reactor containing plasma through magnetic confinement have been considered. So far, the tokamak configuration (Figure 1) demonstrated the best performances [11].
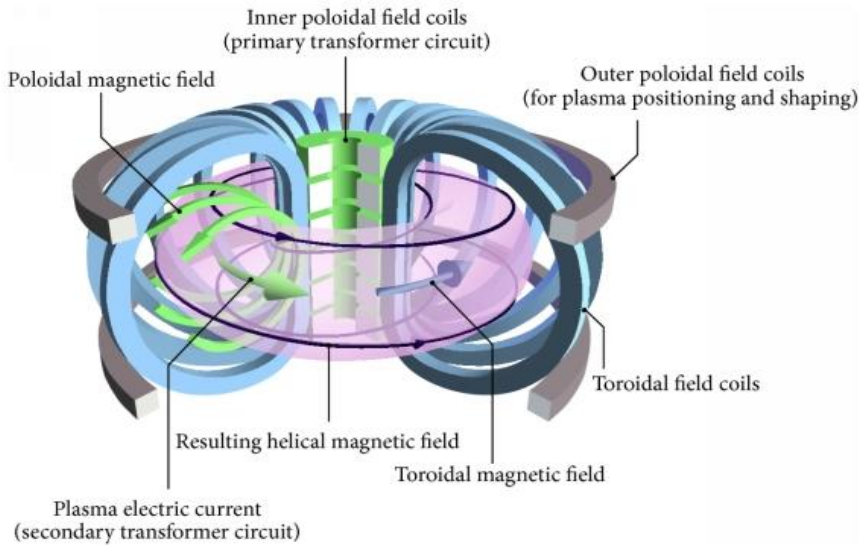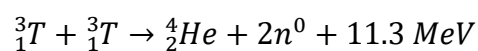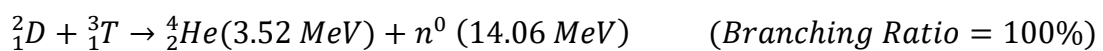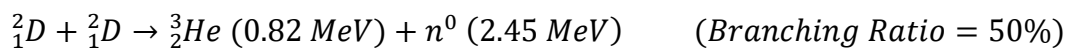

Figure 1: The layout of a typical Tokamak reactor: the scheme shows the inner, toroidal and poloidal coils that create the magnetic confined field.

In particular, in the Tokamak (toroidal chamber magnetic) configuration, the magnetic field is generated by coils around the torus. The magnetic field lines are arranged in such a way as to confine the charged particles of the plasma to the interior of the torus. The toroidal magnetic field, created by the external coils equally spaced around the torus, ensures the primary confinement because charged particles gyrate around the magnetic field lines (Larmor radius) [12]. The toroidal magnetic field decreases radially, so it is insufficient to compensate for radial instabilities involving the presence of particle drifts and, consequently, a charge separation. A toroidal plasma current (induced by the central solenoid) is used to create a stabilizing poloidal magnetic field (twisted B-lines) to confine the plasma. The resulting magnetic field, composed of the toroidal and poloidal magnetic fields, has intertwined B lines that develop in a helical pattern, allowing particles to short-circuit the electric field; the particles orbit in closed loops [13].

2.2 Fusion plasma as a neutron source

The fusion plasma produced in Tokamak (TOroidalnaya KAmera MAgnitnaya Katushka, Kurchatov USSR) machines can be considered an extended and continuous source of neutrons. As the typically used fuels are light ions like deuterium (D) and tritium (T), the fusion reactions include the D-D reaction, the D-T reaction, and the T-T reaction, all with the production of neutrons:

$$_{1}^{2}D + {}_{1}^{2}D \rightarrow {}_{2}^{3}He\ (0.82\ MeV) + n^{0}\ (2.45\ MeV) \qquad (Branching\ Ratio = 50\%)$$

$$_{1}^{2}D + {}_{1}^{3}T \rightarrow {}_{2}^{4}He(3.52\ MeV) + n^{0}\ (14.06\ MeV) \qquad (Branching\ Ratio = 100\%)$$

$$_{1}^{3}T + {}_{1}^{3}T \rightarrow {}_{2}^{4}He + 2n^{0} + 11.3\ MeV$$

Then, there are three neutron characteristic energies depending on the reagent ions. In particular, most of the working fusion reactors exploit the D-T reaction, and the neutron flux with the ~2.5 and ~14.0 MeV energies is proportional to the number of triggered reactions, which in turn depend on the fuel concentration, the reached temperature, the additional heating, and so on. D-T is the most interesting reaction both from the point of view of the energy gain because of the large amount of energy released and the high value of the cross-section. Furthermore, for the D-T reaction, the energy lost by irradiation is negligible compared to that produced by fusion, and for this type of reaction, also the alpha particles dissipate their energy in the plasma itself, contributing to its heating and then to self-sustain the system without the need for external power. Therefore, systems based on the D-T fuel, characterized by higher reaction cross section and a high energy yield (17.6 MeV), require a relatively lower plasma temperature (> 4 keV). For a reaction in which the two species of colliding nuclei, whose densities are characterized by distinct continuous rate distributions, the local fusion reaction rate R [m^{-3}s^{-1}] depends on the density of the fusing ions (n_i and n_j) and the reactivity $\langle \sigma v \rangle$:

$$R = n_i n_j \langle \sigma v \rangle$$

The reactivity is calculated as the integral over the velocity distributions of the fusing ions and their relative velocities, weighted by the fusion cross sections.
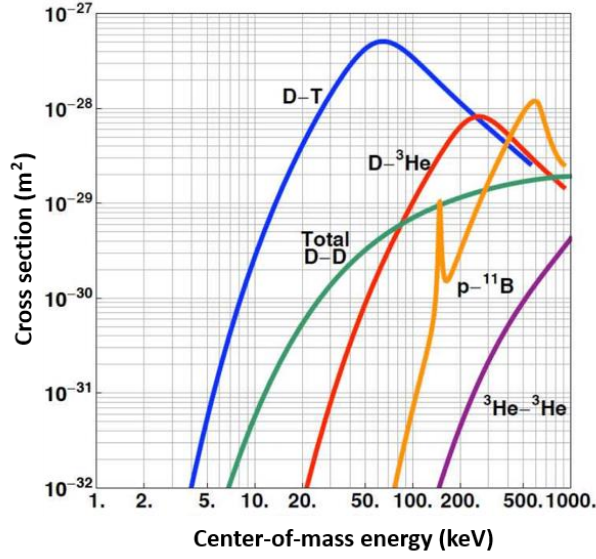
Figure 2: Cross sections of conventional nuclear fusion reactions as a function of center-of-mass energy.

To compare the various reactions, observing cross-section's trend is beneficial. Figure 2 [14] shows that the D-T reaction reaches the highest cross-section value. Direct fusion reactions can be induced by ions in thermal equilibrium (thermonuclear reactions) or by the interaction of neutral atoms (or negative ions) of deuterium, used as additional heating, with the plasma ions ("beam-plasma" source). In this second case, these are fusion reactions that involve deuterium nuclei with velocity components that deviate from the thermal distribution as they come from the beam of neutrals or negative ions accelerated to high energy. In particular, reactions can occur between the ions of the thermal bulk and those of the neutral beam from NBI (Neutral Beam Injection) or between the ions of the thermal bulk and the ions accelerated by RF (Radio Frequency). In the case of a plasma in thermal equilibrium, the velocity distribution of the reactants follows the Maxwell-Boltzmann distribution, and the neutron emission spectrum $f_{th}(En)$ follows a distribution that a Gaussian function can approximate:

$$f_{th}(E_n) \approx \left(\sigma_w (2\pi)^{1/2}\right)^{-1} exp\left(- (E_n - \langle E_n \rangle)^2 / 2\sigma_w^2\right)$$

This distribution describes the thermal component of the plasma of the neutron spectrum that results from the fusion reactions of the nuclear fuel elements; the function is centered around $\langle E_n \rangle$ and has a width (σ_w) that depends on the ionic temperature ($\sigma_w \approx C\sqrt{k_B T_i}$). The width of the neutron energy distribution can be used to estimate the plasma temperature Ti, and this is a crucial information that can be obtained through neutron spectrometry. Unlike these direct emissions, there are also neutron sources that do not come from nuclear fuel but from impurities in the plasma (such as ^{9}Be and ^{12}C) originating in surrounding walls and other internal structures; indeed, in the plasma, there are accelerated ions with sufficient energy (> 1 MeV) that can interact with impurities in the plasma, producing high-energy neutrons. In addition to these, neutrons produced by photo-production reactions triggered by runaway electrons impact the structures of the vacuum chamber. For magnetically confined fusion reactors, the primary source of information by neutron monitoring relies on direct neutron emission. In order to isolate the direct component and select the emission from a specific region that observes the plasma along a well-defined line of sight, appropriate collimation systems are commonly integrated, as schematically represented in Figure 3a [15].

(a)   (b)
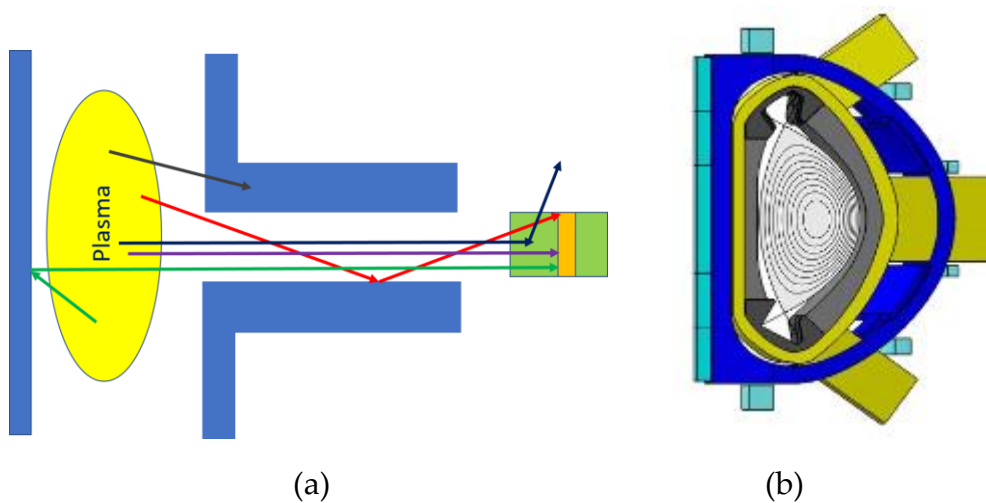
Figure 3: (a) Schematic illustration of neutron interactions along a port structure in a tokamak; (b) 3D models of a typical cross-section of a vacuum vessel including ports for diagnostic location (olive green).

Figure 3a shows a simplified representation of the neutron flux at a detector. The different colors of the arrows represent the different types of neutron flux at the detector (the orange zone is the detector's active volume). The purple arrow represents neutrons that come directly from the source and reach the detector without interacting with any other material (direct flow); red, neutrons that other materials have scattered before reaching the detector; green, neutrons that have been scattered by the detector itself and then backscattered out of the detector (backscattered neutron flux); blue, neutrons that have been scattered by other materials but have not been absorbed; black, neutrons that have been stopped or absorbed by port structure. Figure 3b [16] shows the schematic section of the tokamak chamber in which openings is also used to insert and remove the diagnostic instruments, called "port" cells. Considering that the measurement of neutrons is typically done using collimated lines-of-sight or fields of view, the results will be an integral measurement in the field of view of the instrument. Specifically, the realization of the collimation systems requires reliable shielding systems to reduce exposure to any potentially harmful background radiation at the measurement location. The type of shielding is influenced by the proximity to the plasma, the space required by a given diagnostic, and the need for intervention and replacements; in some cases, the neutron detector can be incorporated into a more complex system, such as neutron chambers. This background is primarily composed of gammas (from the activation of component materials surrounding the location of the detector), capture gammas (gamma radiation due to the absorption of a neutron in a nucleus), and scattered neutrons (i.e., non-direct neutrons). As shown in Figure 4 [15], its contribution has an important weight that must be understood and controlled to improve the design of the collimation system and the interpretation of data coming from neutron diagnostics. The plot shows a simulated typical scenario for a Tokamak machine. The black line shows the total neutron spectrum, including the scattered neutrons from DD and DT reactions. As can be observed, its contribution is important

concerning the direct neutron emission (thermal and beam thermal components), and its characterization is required to obtain high-quality results.
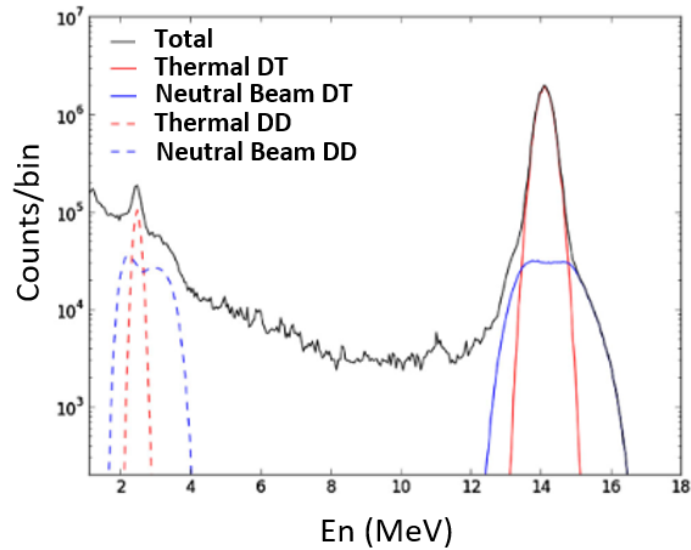
Figure 4: MCNP simulation result of direct and scattered neutron emission spectra in ITER-like 90:10 DT plasma: dashed colored lines show the DD reactions, the continuous colored lines show the DT reaction, while the black line shows the total spectrum due to direct and scattered emission.

Because the experimental conditions around the reactor are characterized not only by very high levels of neutron and gamma background radiation but also by high temperatures, high magnetic fields, high-frequency, electromagnetic noise interference, and so on, the detector must be characterized by resistance to harsh environments conditions. Often, it is necessary to shield and protect the entire diagnostic system or at least the most delicate part of it, such as the control electronics. Finally, as mentioned above, the neutron diagnostic system installed at the outlet of the collimation system must guarantee some specific requirements: the ability to separate the contributions from a mixed field of neutron and gamma background, an excellent signal-to-background ratio, a time resolution down to μs, and then a rate capability in the MHz region.

2.3 Plasma parameters measurable by neutron diagnostics

Neutron diagnostic systems are becoming increasingly crucial for future fusion devices. In large fusion experiments, neutron diagnostics will play an even more important role, as many other conventional diagnostic methods cannot operate nearly continuously under high neutron and gamma-ray fluxes. The main purpose of a neutron diagnostic system for fusion plasma is the measurement of the neutron emission from the plasma that provides valuable information on plasma performance and fusion reactions. In particular, the main goal is to measure the spatial and energy distribution of the direct neutron component. Then neutron measurements on fusion experiments must evaluate the total emission, its relative spatial distribution, and the energy spectra of neutrons emitted from small plasma volumes or selected lines of sight through the plasma. Neutrons play a crucial role in fusion reactions, and their measurement can provide important information about plasma temperature, density, and composition; neutron diagnostics can determine the total neutron yield, neutron energy spectrum, and neutron fluence. These measurements are crucial for understanding plasma stability, fusion power, and reaction rates. They can help optimize plasma conditions and validate theoretical predictions of fusion performance. Furthermore, neutron diagnostics can also be used for safety purposes: neutrons can induce radioactivity in surrounding materials, and therefore, monitoring the neutron emission is essential for radiation protection and to ensure that a fusion reactor is safe to operate. The main parameters that these measurements can provide are fusion reaction rate (i.e., the number of fusion reactions per unit volume and unit time) that is determined through detectors that detect the neutron flux (counting mode), thermal fuel ion temperatures (T_i) which can be deduced from the width of the thermal neutron emission component, fuel ion densities, and ratio n_T/n_D (between Tritium and Deuterium), information on ion diffusivities, the intensities of different neutron components, and their weight concerning the thermal component.

Consequently, neutron diagnostics can provide reliable information on basic plasma parameters, such as density and temperature, and can also offer information on particle transport and MHD activity. Potentially, neutron spectroscopy would also allow the measurement of the toroidal rotation speed of the plasma. Moreover, by referencing the additional heating sources, specific parameters such as heating efficiency, RF temperature effects, velocity distribution functions, etc. can be determined [17]. However, since only for a limited number of plasma conditions, it is possible to directly obtain information about the plasma parameters from the measured neutron signals, in most cases, a dedicated numerical simulation will be needed to deduce the plasma parameters from the measured signals. In conclusion, plasma parameters measured by neutron diagnostics are crucial for understanding the behavior and characterization of fusion plasmas in fusion research experiments and reactors.

Chapter 3

Instruments and methodologies

3.1 Detector systems currently used for neutron measurement

A neutron is a nucleon, i.e., a constituent of the atomic nucleus. As a free particle, it is unstable but has a long lifetime of about 11.7 minutes at rest. A neutron is made of 2 DOWN quarks and 1 UP quark; each with its electric charge, and the resulting electric charge of the neutron is equal to zero. For this reason, it is unaffected by the electromagnetic force and can approach the atomic nucleus. Consequently, even so-called "slow" neutrons with the same average kinetic energy as ordinary gas molecules, e.g., about 0.03 eV at ordinary temperatures, can easily interact with atomic nuclei. Neutrons interact only when they collide with a nucleus through the short-range "strong" force, and since the matter is made almost exclusively of vacuum, neutrons have a low interaction probability; that is, similarly to photons, they interact in a stochastic (probabilistic) manner and are characterized by high values of the mean free path: the distance between two successive interactions. As mentioned, the interaction of neutrons is a probabilistic concept, and the physical quantity that describes it is the cross-section, measured in barn (1 barn = 10^{-24} cm^2). The larger the cross-section, the larger the probability of reacting with the target. The reactions induced by neutrons can occur at any energy, and the variation of the cross-section for a given material with neutron energy is an essential factor. Radiation must interact with matter to be detected, and the material with which it interacts must produce quantifiable information in some way: the information must be transduced as a measurable quantity. As mentioned previously, neutrons cannot be detected through electromagnetic interactions. In the case of charged particles, several materials produce a given amount of charge after interaction with particles, and this charge is

then properly transported and detected. Neutrons must exploit nuclear force to interact with matter and usually exploit other reactions that have charge particles as products. Neutrons interact with matter through different mechanisms that can be divided into scattering and absorption nuclear reactions (Figure 5) [18]. In the first case, scattering can be elastic or inelastic and, as a result, a given amount of the incident neutron energy is transfered to the recoil nucleus that, in the case of inelastic scattering, can be in an excited state with consequent emission of a secondary particle (typically a gamma photon). In the second case, the nucleus absorbs the incident neutron and becomes unstable with the consequent production of other particles. In particular, neutron absorption reactions are classified as radiative (radiation capture and gamma emission), charged particle-out (transmutation reactions), neutral (with the production of neutrons), and fission reactions (the nucleus splits in fragments).
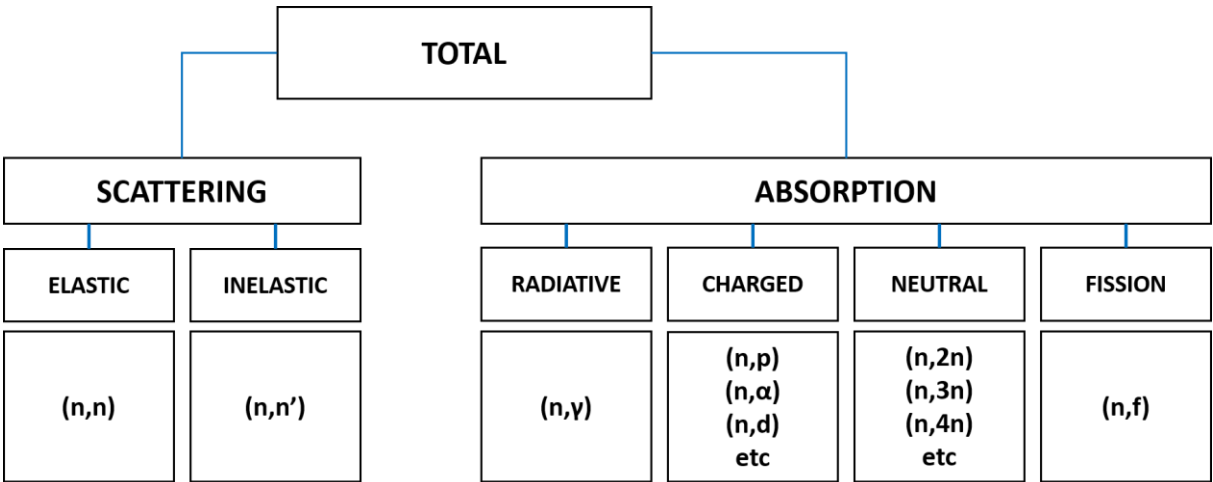
Figure 5: The different categories of neutron interaction with matter and the corresponding nuclear reactions that can be used to detect neutrons.

Neutron detection exploits specific interaction mechanisms, and detector systems can be classified according to the corresponding reaction. Table 1 resumes the main reactions to the type of detector that exploits them. Table 1 focuses mainly on the

detection systems for fast neutrons because this work is devoted to detecting fast neutrons in nuclear fusion.

NUCLEAR REACTIONS FOR NEUTRON DETECTION	DETECTOR SYSTEMS
Nuclear elastic scattering	- Scintillators - Thin-foil proton recoil and - Time-of-flight systems
Nuclear inelastic scattering	- Activation foils - Systems dedicated to prompt gamma-rays activation analysis
Nuclear reactions	- Diamond semiconductor ^{3}He tubes - Li glass scintillators
Fission reactions	- Fission chambers (FC) - Parallel plate avalanche counters (PPAC)

Table 1: Main nuclear neutron reactions and the typical diagnostic devices that exploit them for neutron detection.

Among the detection systems that are based on nuclear elastic scattering reactions, there are proton recoil scintillators that exploit hydrogen-containing materials. It is essential that the volume of the scintillator material is adequately extended so that all the energy of the recoil proton will be deposited and measured. The typically used hydrogen materials can be organic crystals (anthracene and stilbene), plastic and liquid scintillators that can use organic scintillators dissolved in hydrogenated solvents. Methods based on thin-foil proton recoils are telescopic systems where neutrons interact on a thin target of organic polymer. The recoil protons are observed by a detector or multiple detectors in coincidence in order to avoid unwanted signals

coming from the background and other neutron interactions. These detectors can be usual solid-state detectors. Time-of-flight systems are based on the measurement of the neutron time of flight (ToF) and can be used for pulsed neutron sources. In this case, the used detectors must be fast and provide a time resolution of a few ns or lower depending on the energies of the observed neutrons. This is not possible on neutron sources like nuclear fusion plasmas; in contrast, a double scattering configuration is used where a single neutron interacts in two consecutive detectors to measure its ToF. Since the distance between these two detectors is defined, it is possible to measure the neutron energy. The activation foils method uses some sheets of particular materials (^{115}In, ^{198}Au) that become radioactive after capture or inelastic scattering with neutrons with gamma and beta particles emission. The neutron flux and relative released energy are measured by detecting the activation foil's decay products.

Methods based on fission reactions regard fission chambers and Parallel Plate Avalanche Counters (PPAC). A PPAC detector is a proportional gas chamber of two conducting parallel plates that work as electrodes [19]. Often, these electrodes are segmented in strips; in particular, one has a strip orthogonal with respect to the other to obtain 2D information about the position of a neutron. A strong electric field is generated between the plates by applying a high voltage bias between them. One typically used gas is octafluoropropane C_3F_8 at a pressure of a few mbar. In order to observe neutrons, PPAC chambers are combined with neutron converters ^{6}Li, ^{10}B, and ^{235}U targets.

Two main detector systems will be briefly presented between the methods based on nuclear reactions: Lithium scintillators and ^{3}He gas tubes. Usual diamond detectors will be discussed more extensively in the next section. Li scintillators and ^{3}He tubes exploit the nuclear reactions ^{6}Li (n, α) ^{3}H and ^{3}He (n, p) ^{3}H, respectively [18]. The reaction products have a total kinetic energy that is the sum of the kinetic energy of the incoming neutron minus the Q-value of the reaction. Then, by measuring the kinetic energy of the reaction products, it is possible to obtain an energy measurement

of the incoming neutron. Due to the high value of the ^{6}Li reaction Q-value (4.78 MeV), the spectroscopy of neutrons is limited to several hundreds of keV. Li scintillators can be lithium iodide (europium-activated) scintillator crystals, the same used for thermal neutrons or lithium glass scintillators that can also be realized as small-diameter optical fibers. Another possible configuration is represented by the lithium sandwich spectrometer, a thin layer of lithium fluoride or lithium-containing material placed between two semiconductor diode detectors. Detectors exploiting the ^{3}He (n, p)^{3}H reactions can work in different configurations: in general, they are proportional gas tubes using a mixture of ^{3}He and other gases like argon, methane, etc., but they are also realized as ionization chambers. In addition, ^{3}He gas and other noble gases like Xenon, can have sufficient light yield so that the ^{3}He chamber is used as a scintillator detector. For the ^{3}He tube, the response function that would be a single peak due to the ^{3}He (n, p)^{3}H shows other undesirable contributions due to the wall effect and elastic scattering on ^{3}He ions. In this case, signal shape due to these effects is used to select and remove these unwanted events.

3.2 CMOS detectors based on the Timepix3 chip

In the last years, many solid-state particle detectors in high-energy physics experiments are based on hybrid pixel technology. It is similar to complementary metal-oxide semiconductor (C-MOS) technology [20], in which the charges produced by particle interactions are amplified and detected as they are produced (direct detection). This represents a significant advantage over CCD (Charge-Coupled Device) systems in terms of processing times. Indeed, CCD systems accumulate charges and then discharge them through a slower charge transfer process, especially if the sensor has many pixels [21]. Hybrid technology does not need a scintillator material to convert particle interaction into visible light because it is based on the direct detection of charge. Typically, it is made of a micro-soldered sensor layer with a step-size of 1 pixel to an electronic chip by the bump-bonding technique, an operation

called hybridization. Each pixel thus consists of a sensor part that detects the particle and a readout electronics that processes and digitizes the signal. TPX-based detectors represent an important family of the new hybrid detectors. In the present chapter, attention will be focused on hybrid semiconductor detectors based on the TPX3 chip, a recent development of TPX detectors. The TPX3 [22,23], the successor to the TPX1 detector, is a new-generation pixel detector belonging to the family of semiconductor detectors developed in the context of Medipix collaboration [24] that includes CERN, research centers, and universities. As mentioned, it is a hybrid pixel detector because it consists of the coupling of two components: a TPX3 ASIC reading chip and an active volume formed by a semiconductor (usually silicon) sensor layer, having an area of 14 × 14 mm² and uniformly divided into a matrix of 256 × 256 pixels with a pitch of 55 μm (Figure 6a). The coupling between the sensor and the chip is made using the bump-bonding technique, and the resulting assembly is mounted on a PCB board [25]. Similarly to other hybrid pixel detectors, the whole pixel matrix can be managed with greater flexibility and lower energy consumption.


(a)   (b)
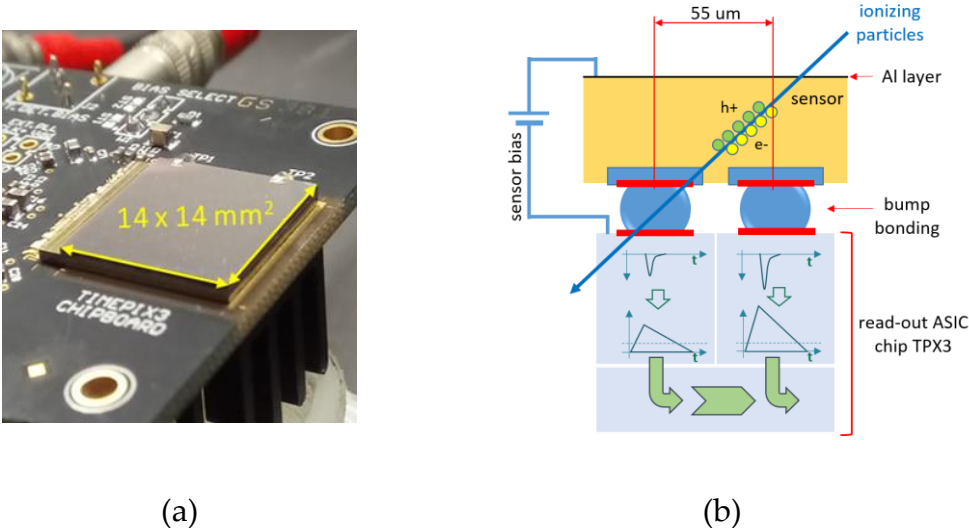
Figure 6: (a) A picture of a TPX3 detector that shows the surface dimensions of the active area and the PCB board; (b) a diagram of the TPX3 section that highlights the active layer, the bump-bonding spheres, and the underlying read-out chip channels for signal processing.

The sensor layer is realized with a block of semiconductors with different thicknesses (from 100 μm to 2 mm) depending on the applications. The semiconductor is doped n or p, and, in correspondence with each bump-bonding, there is a small layer doped with opposite sign, p+ or n+, respectively. Consequently, a depletion region is created close to the side facing the bump-bonding spheres. In general, it has a defined extension that does not cover all the semiconductor thickness and depends on the amount of doping. The depletion region can be increased by applying an appropriate reverse bias voltage, and, in this case, it is made through an aluminum layer of 100 nm deposited on the opposite face of the semiconductor block, as shown in Figure 6b. Then, applying a bias voltage, the detector's active volume increases until it extends across the entire available semiconductor volume. This is important because the appropriate bias defines the optimal working point to maximize the counting performances and to provide the correct charge measurements. The pixel is connected to its readout electronics chain at the opposite side of each bump-bonding sphere. A sensitive charge preamplifier (CSP) with a tunable feedback capacitor is the main component necessary to process the input signal. The CSP configuration in its most basic simplified form is shown in Figure 7 below.
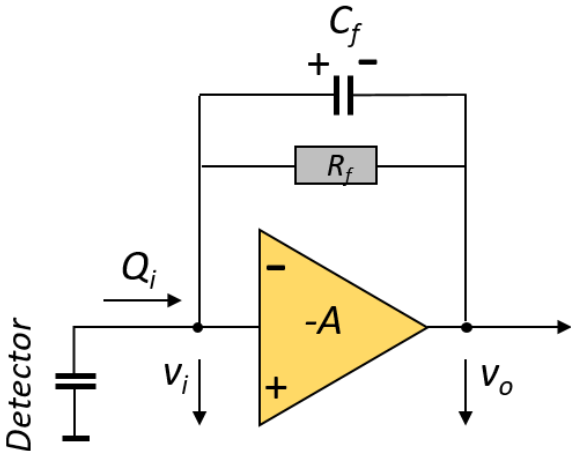

Figure 7: A Charge Sensitive Preamplifier's scheme highlighting the feedback capacitor and resistor components.

An interacting particle produces electron and hole pairs in the semiconductor volume over a given pixel. Due to the presence of the electric field in the depletion region, electrons or holes (depending on the type of doping) drift towards the bump connection and induce a current pulse signal. CSP receives the signal and produces an amplified output voltage signal with a longer time width, as shown in Figure 8 [26].
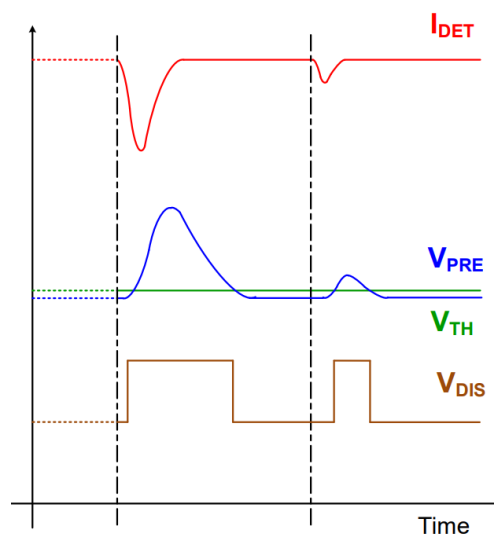
Figure 8: A qualitative scheme showing the main processing steps of two typical current signals (I_{DET}) induced on pixels: the CSP increases the signal amplitudes and time width (V_{PRE}), which are then compared to a threshold level (V_{TH}) by a discriminator that provides a square signal (V_{DIS}) having a time width proportional to the signal amplitude. It can be observed that the two output time widths are proportional to the original current signal amplitudes.

If Q is the charge transported by the current signal and C_f is the feedback capacity, the output voltage signal has a maximum amplitude of Q/C_f. The output CSP signal can be outlined as a triangular signal with a fast-rising edge and a slow-falling edge. Then, this signal is processed by a comparator that compares it to a threshold-level voltage and produces an output constant signal having a time width equal to the time the triangular signal is over the threshold (Figure 9).
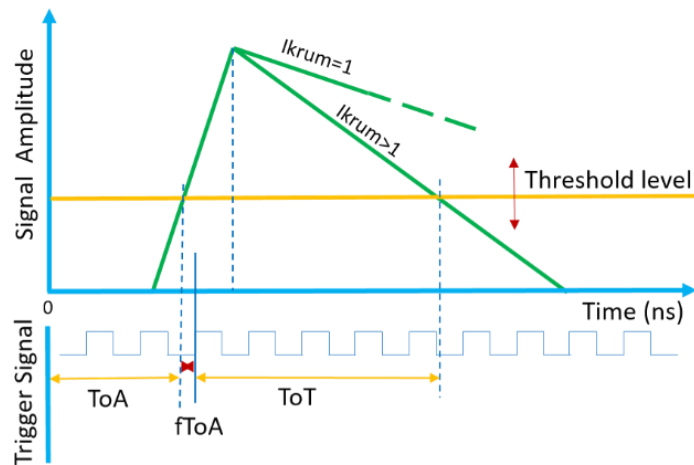
Figure 9: A schematic layout of a signal measurement on TPX3. After the triangular signal produced by CSP is compared to a threshold level, the Time-of-Arrival (ToA) is measured by the number of clocks from the start until the signal skips over the threshold. At the same time, Time-over-Threshold (ToT) is given by the number of clocks registered when the signal is over the threshold.

This time interval is measured as digital counts by an internal clock working to the frequency of 40 MHz [27]. This is the Time over Threshold (ToT) mode and provides a digital measurement of the released charge, because the time the triangular signal is over the threshold depends on its maximum amplitude and it is proportional to the collected charge, allowing to take full advantage of the digitization and to improve the dynamic range of the charge. The falling edge of the CSP signal can be adjusted acting on the feedback capacitor and changing its value. This can be tuned through the Ikrum parameter on the control panel of the acquisition software. Simultaneously, the time when the rising edge of the CSP signal exceeds the threshold is recorded and provides the Time of Arrival (ToA) of the signal to a software or hardware reference time. This is a measurement of the particle's arrival time. The TPX3 chip provides a maximum time resolution for ToA of 1.6 ns because, to measure ToA, it has an auxiliary internal clock working at 640 MHz. TPX3 provides two acquisition modes: frame-based and data-driven. In frame-based mode, the acquisition is managed as a sequence of time windows, and, for a defined time window, all events can be registered in ToT mode

28

and are integrated into that time window. In addition, the activated pixel is no longer available for the entire frame capture time; the stored data must first be transferred at the end of the frame, only then the whole pixel matrix is ready for a new acquisition. In this configuration, recorded ToA times are limited to 14 bits and cannot span long time intervals as required in our measurements. Therefore, frame-based mode can be used to distinguish single particles but only when fluxes are sufficiently low not to have superimposed signals. Instead, in the data-driven mode, it is no longer a sequence of frames but a single extended interval in which data relating to an activated pixel is transferred immediately. The pixel becomes available after a minimum of about 475 ns. In addition, the control module allows for managing large ToA values to cover longer time intervals from the start of the measurement. In this case, the detector can sustain the flow of incident particles. A timestamp can be helpful for more detailed analysis like lifetime evaluation and ToF measurements. Among the several improvements of TPX3 compared to its precursor TPX1, it must be noted that TPX3 can acquire simultaneously in counting, charge, and time and that its acquisition can be in data-driven mode, both characteristics being missing for TPX1.

3.3 Timepix3 working condition set-up

Before measuring with a TPX3 detector, some important acquisition parameters must be analyzed and properly set. Recently, a new readout module has been realized by the Institute of Experimental and Applied Physics in Pilsen (Czech Republic), together with a new software interface: the Katherine module [28] and the MMTrack software [29]. In this work, both have been used to characterize and set the appropriate acquisition parameters for the measurements that will be shown. Before a standard acquisition operation, TPX3 detectors must undergo a threshold equalization procedure. As expected, all the pixel channels of the matrix have different threshold levels optimized to cut the electronic noise; a Gaussian statistical distribution of

thresholds is expected with a mean value and a given sigma. It is necessary to perform a threshold equalization to find the best thresholds, pixel by pixel, and to reduce the spread of thresholds distribution to the minimum possible value. To set the threshold, the control panel has two parameters: a 4-bit coarse scale plus a 10-bit fine-tuning scale. In general, threshold equalization is performed automatically by the control software and finds the optimal distribution by searching a configuration mediated between those obtained with the extreme values of the coarse scale (0 and 15). After this procedure, the mean value found corresponds to the maximum electronic noise, and the optimal minimum threshold level is obtained by applying a common additional value to all pixels to minimize the number of noisy pixels. Should particularly noisy channels remain, they are masked out, mainly because they can over-contribute to the output data and are unnecessary. This threshold equalization procedure is performed with a 0 bias value on the semiconductor sensor. Once a threshold has been set, finding the optimal bias voltage to exploit the available active semiconductor volume in terms of counting and charge measurements is necessary. In order to demonstrate this procedure, a bias scan will be shown for one TPX3 semiconductor detector that has been adequately characterized to have a valid reference for the new diamond detector based on TPX3. For this study, a Cadmium Telluride (CdTe) semiconductor TPX3 detector was used; it has a thickness of 500 μm and is an n-on-p semiconductor, therefore it is polarized with negative bias. Table 2 lists the main properties of CdTe semiconductors.

| Semiconductor	Si	CdTe
Density [g/cm³]	2.33	5.85
Z	14	48,52
Band gap energy - E_{gap} [eV]	1.12	1.44
An ionization potential - ε [eV]	3.6	4.43
Radiation length - X_0 [cm]	9.37	1.52

Table 2: The main characteristic physical parameters for the Silicon and CdTe semiconductors, typically used for particle detection.

After threshold equalization and the set of the optimal minimal threshold, the detector has been irradiated with [241]Am alpha source, changing the bias from zero down to -150 V in steps of 25 V. Alpha particles from [241]Am source have a maximum energy of 5.49 MeV and absorption of these particles is expected in few tens on microns in CdTe. The charge is released close to the surface. The acquisition was set in data drive-mode for each point on a time window of 600 s. A plot of the number of alphas as a function of the applied bias (Figure 10) clearly shows that a plateau region has been reached.
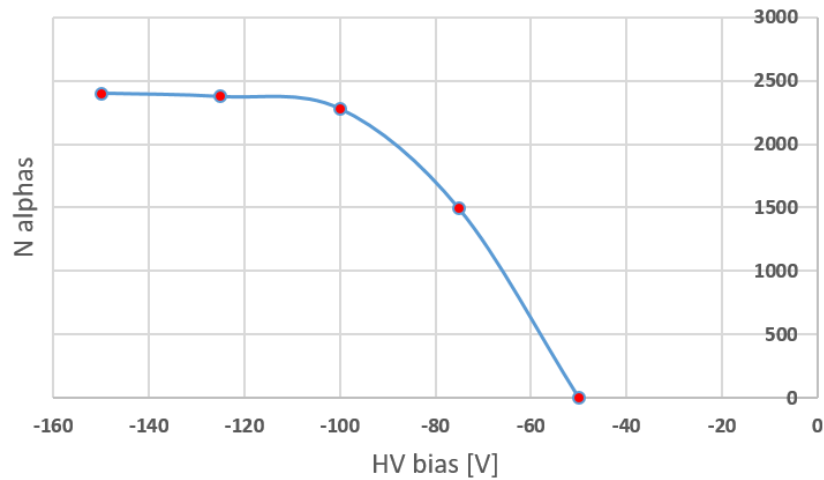
Figure 10: Counting plateau plot of the 500 μm CdTe TPX3 for a bias voltage scan between -150 and -50 V with 25 V steps.

At the same time, the mean ToT released by alphas as a function of the applied bias increases. Consequently, setting the working bias at -150 on the plateau region of the counting plot, the maximum amount of charge is collected without breakdown risks for the CdTe semiconductor. The next important step is energy calibration pixel by pixel. In general, the standard applied procedure is based on irradiation of the detector to define mono-energetic X-ray lines to find the correspondence between photon energy and the measured ToT [30]. Low-energy X-rays interact locally so that, in most cases, a given photon interaction fires only a single pixel. It is expected to have a calibration curve for each pixel with a given spread of values all over the pixel matrix. Before proceeding to energy calibration pixel by pixel, it was advantageous to evaluate the spatial uniformity response of the detector in ToT mode. This study can be performed for different photon energies using X-ray fluorescent lines and irradiating the entire detector area [31]. Figure 11 shows the experimental setup, consisting of an X-ray source, a target, a Silicon Drift Detector (SDD) spectrometer, and the CdTe TPX3.
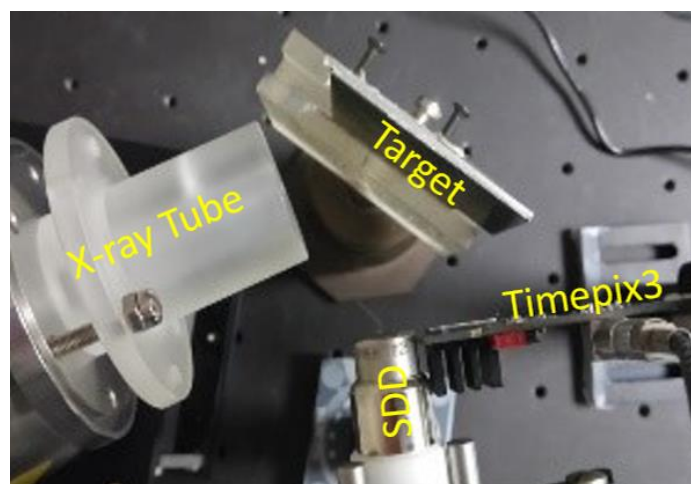
Figure 11: Experimental set-up for X-ray calibration of the CdTe TPX3: the X-ray tube irradiates a material target, and TPX3 is placed on the front side to detect the fluorescent spectra.

The source consists of an Oxford Instrument X-ray tube operating at a maximum voltage of 50 kV and a filament current from 5 to 1000 nA. Targets of different materials (Fe, Cu, Pb, and Mo) have been excited through the X-ray tube. The SDD spectrometer is used to verify fluorescent emission lines and measure the mean photon energy for each target. In contrast, the TPX3 measures the same spectra in ToT units. Figure 12 shows the results obtained for copper X-ray lines with the SDD spectrometer and TPX3 detector.

(a)   (b)
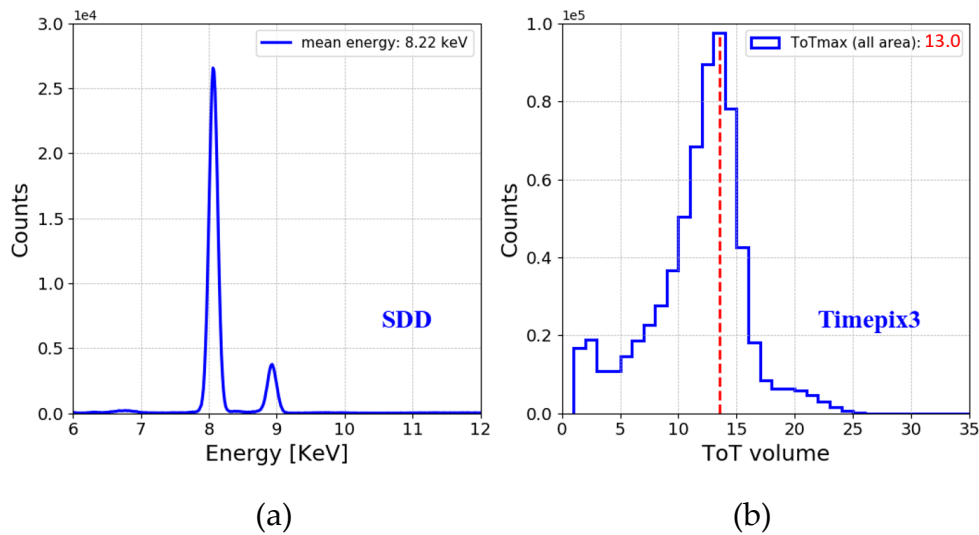
Figure 12: Energy spectrum measured by the SDD spectrometer (keV) and TPX3 detector (ToT counts).

The average energy calculated from the measured SDD spectrum is approximately 8.2 keV, a weighted average between the copper kα (8.04 keV) and kβ lines(8.9 keV). At the same time, TPX3 provides a global ToT histogram with an average ToT value equal to 13, which measures the average energy of the fluorescent photons that interact over the entire detector area. TPX3 has a lower energy resolution than SDD, and it cannot distinguish the two copper lines. The ToT uniformity response was evaluated by dividing all TPX3s detectors in a matrix of 16x16 sub-areas (Figure 13a). Then, the maximum of the ToT distribution for each sub-area was evaluated. Figure 13b shows

33

the mean values of ToT and sigma obtained from a Gaussian fit on the ToT distributions on all 16 sub-areas.

(a)   (b)
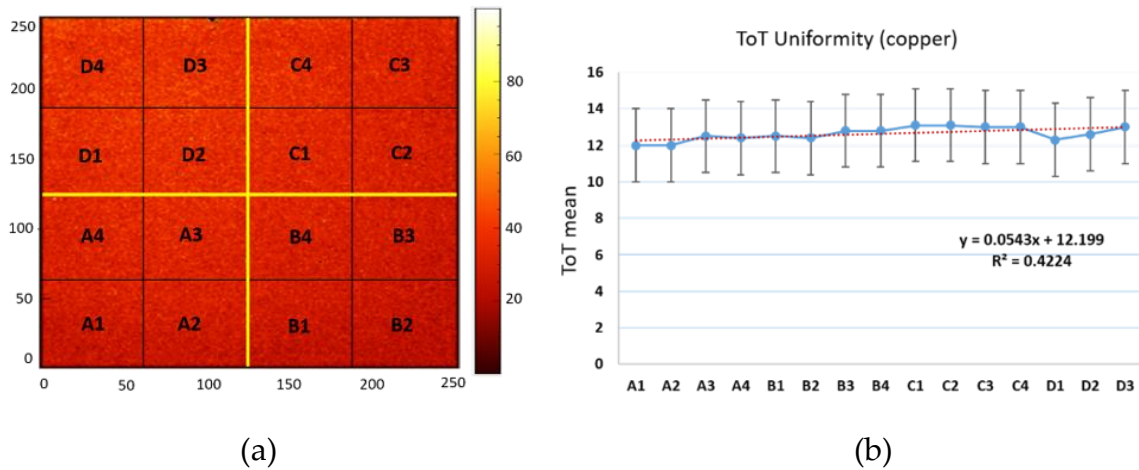
Figure 13: (a) Image of the TPX3 when irradiated by the Cu fluorescence spectrum selecting all single pixels; (b) ToT distribution obtained on the 16 selected areas.

Based on these results and repeating a similar analysis on the other materials, the TPX3 showed uniformity within 15% of the measured mean value. This means that the same energy calibration curves all over the pixels have a limited spread, and a global calibration curve can be used for all channels without applying a time-consuming energy calibration procedure pixel by pixel. According to the performed X-ray measurement the global calibration curve, obtained with different X-ray fluorescence lines, is shown in Figure 14. This represents an added value to the performance characteristics of the detector itself.
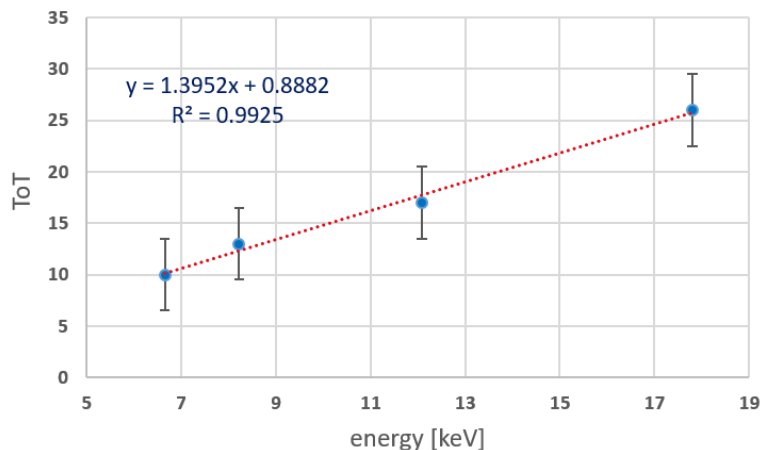
Figure 14: ToT vs.energy calibration of the CdTe TPX3 using the Fe, Cu, Pb and Mo fluorescent lines.

Because CdTe TPX3, as well as the new TPX3 with diamond, will be used mainly with heavy charge particles as those produced by the neutron interactions, a crucial point was the measurement of charge released by these particles and their energy. As will be shown extensively in Chapter 4, after the interaction of an alpha particle with TPX3, the produced charge distributes on a group of adjacent pixels (cluster); thus, alpha energy must be calculated by converting each ToT pixel to energy according to the global calibration curve and then summing all the energy values of the cluster.

However, using alpha particles of defined energy showed a significant discordance with the energy measured according to the global calibration curve obtained with X-rays. This discordance was also observed for TPX1, with a different calibration curve between low and high charge ranges. In order to verify if a similar behavior is present also for TPX3, a high energy calibration was performed using a source of alpha particles because of the much larger quantity of charge they release [32,33].

An alpha energy scan with a [214]Am source has been used. It is placed on a linear stage to vary the alpha's energy by varying its distance from the detector surface; as the distance between the detector and the source increases, alpha particles must travel through more air. This means that they are more likely to lose energy by interacting

35

with air and be scattered. Therefore, the probability of detecting an alpha particle decreases as the distance between the detector and the source increases, and so does the spread of energy. By scanning the source-to-detector distance, we can produce different energies. Furthermore, a PVC mask with a 1 mm hole was used to select only the perpendicular outgoing alphas. Figure 15a shows the ToT distributions (in black the normalized histograms of the experimental data and in other colors, the Gaussian fits) at the different alpha energies obtained by varying the position of the source with respect to the detector surface from a minimum of 7 mm to a maximum of 37 mm in step of 5 mm.
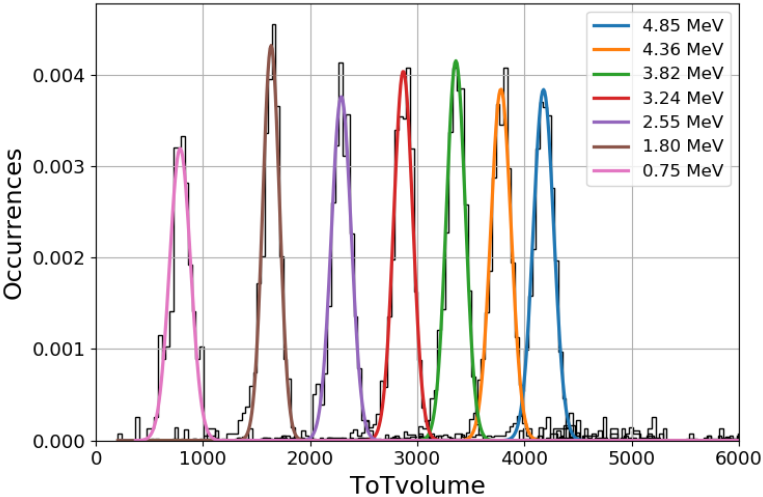
(a)
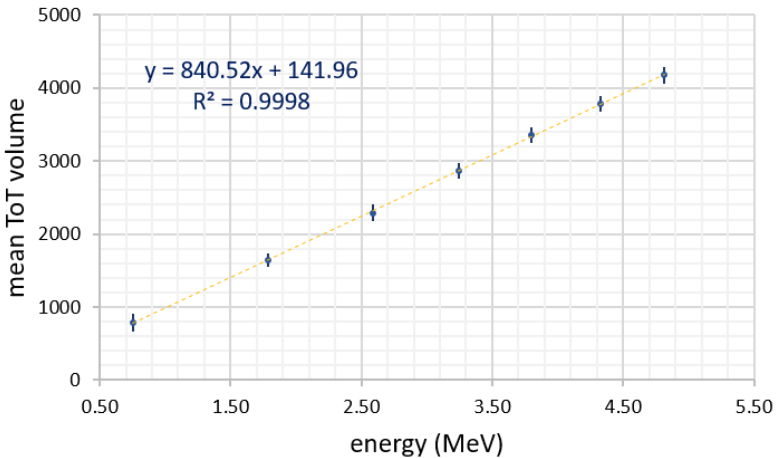
(b)

Figure 15: (a) Distance scan with [241]Am alpha source; (b) high charge energy calibration of mean ToT values.

A single alpha interaction lights up a group of pixels, and the total charge released is measured as the sum of all the pixels' ToT contributions. The result is defined as ToT volume (ToTv) and is measured in clock counts. The experimental setup was also simulated with the CERN version of the Fluka Monte Carlo software [34] to estimate the energy of the alphas reaching the detector. As a result, a calibration curve is obtained for high ToT values (Figure 15b), and an apparent discrepancy is observed for the curve obtained through X-ray calibration.

3.4 Particle interaction and track analysis

TPX3 is a 2D high spatial resolution detector, and a particle's interaction is recorded as a group of adjacent pixels (cluster) that can produce a characteristic spatial distribution also called "track". Using the time window concept (Δt), a more precise definition can be stated as follows. Let Δt represent a positive real number called the 'time window size.' Consider a set of pixels, denoted as X. For each pixel p within X, ToAp represents its time of arrival. We define a subset C of X as a 'cluster' if it satisfies the following two conditions:

1. |ToAp - ToAp'| < Δt, where |ToAp - ToAp'| means that the time of arrival difference between any pair of pixels p and p' within the cluster C is less than Δt. The specific value of Δt depends on factors such as expected drift times of charge carriers and responses of pixel electronics.

2. a path of pixels within the set X must exist, connecting pixel p to pixel p'. This path is defined as a sequence of connected pixels in X that initiates at p and terminates at p'.

Some passive detectors register a track due to particle interactions (e.g., CR39). However, TPX3 provides a digital measurement pixel by pixel of the charge, and dedicated algorithms can analyze data. One of the main objectives of the research work is to characterize the response of the TPX3 to the incident radiation not only in terms

of energy and time but also through morphological analysis of the clusters. Depending on the type and energy of the interacting particle and the diffusion of the charge inside the sensitive volume, for each interaction, the produced cluster of pixels of a given shape will be observed, and, for each cluster, a variety of physical and morphological characteristics parameters can be defined. Among them, there are: "Cluster Size" (CS), defined simply as the number of adjacent pixels in a single cluster, and "ToT volume" (ToTv), the sum of all the Time over Threshold (ToT) count values belonging to the cluster where ToT counts is defined as the number of the clocks over the threshold for a particular pixel. These are the most obvious, and similar definitions are typical for other pixelated detectors. In this context, however, it will be helpful to introduce appropriate morphological parameters that can better identify specific cluster shapes: roundness, linearity, and cluster height. In addition, it is possible to consider no strictly morphological parameters like the centroid coordinates and first ToA. It is worth mentioning that sometimes there are no unique definitions for a parameter. However, we have used the following definitions:

- The Roundness (Rnd) parameter measures how round a cluster is. It can be defined in several ways depending on the discrimination capabilities for some particular clusters. In this work, two definitions will be presented and used in the reported data analysis. The following expression defines the first one:

$$Rnd = \frac{\sqrt{\frac{4\,CS}{\pi}}}{fd}$$

where the numerator represents the diameter of a circular cluster having an area equal to the CS and the denominator is "Feret's maximum diameter" (f_d), i.e., the maximum distance between points around the convex hull contour of a region. The Rnd parameter ranges from 0 to 1 and it is equal to 1 for an ideal circle. The second definition can be stated considering the minima and maxima

38

values of the cluster pixel coordinates (Figure 16). If (X_{min}, X_{max}) and (Y_{min}, Y_{max}) are the couples of the minima and maximum X and Y coordinates, respectively, Rnd is also defined according to the following expression:

$$Rnd = \frac{CS}{\pi \cdot (D/2)^2}$$

where

$$D = \sqrt{(X_{max} - X_{min} + 1)^2 + (Y_{max} - Y_{min} + 1)^2}$$

Again, Rnd can range from 0 to 1, and circular clusters have values near to 1. This second definition will be used to analyze clusters on Diamondpix, because it allows to assign a more reliable value to smaller CS clusters.
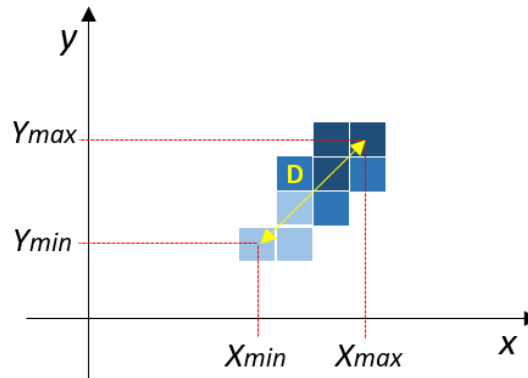
Figure 16: Roundness definition considering the coordinates of the minima and maxima values of the cluster.

▪ Linearity (L) is a measurement of how linear a cluster is. It is computed by dividing the length of the linear line going through the most distant pixels of the cluster (adding up pixels that have a distance to the line less or equal to 1.0) by the number of pixels in a cluster; single pixels have Linearity equal to 1.

An alternative definition to the previous one defines the linearity parameter (a dimensionless number from 0 to 1) as one minus the ratio between the sum of the weighted square distances of all pixels from the cluster axis (s1) and the same weighted sum calculated for the line perpendicular to the axis of the cluster (s1) axis that crosses it in the center of gravity, the co-axis, (s2). As shown in Figure 17.
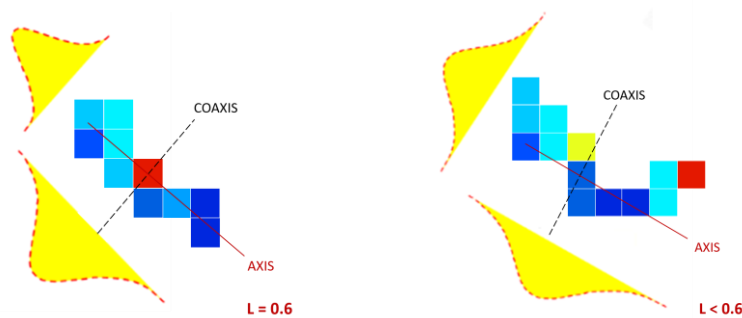
Figure 17: Scheme of linearity definition of two typical tracks: the second is curly-shaped, and linearity is lower than the first.

- Cluster height (ToTh) measures how tall a cluster is, and it is defined by the maximum ToT pixel value in a cluster.

Instead, a more detailed explanation of the two non-morphological parameters is described in the following:

- Centroid coordinates are the coordinates of the cluster's center of mass, and they are calculated by taking the ToT-weighted mean of the x and y coordinates of all the pixels in the cluster.
- First ToA is the Time of Arrival of the first pixel in the cluster (the earliest pixel, see Figure 9).

3.5 Case studies of morphological analysis with Timepix3

3.5.1 Track analysis on radon decay products

The first case study concerns a work that led to my first publication in a journal (A. Tamburrino, G. Claps, F. Cordella, F. Murtas, D. Pacella, "Timepix3 detector for measuring radon decay products", JINST 17 P06009) [31] and the presentation of this work at the 2022 National Congress of the Italian Association for Radiation Protection (AIRP) allowed me to win the PREMIO GIOVANI AIRP 2022 competition. In particular, it describes the application of a TPX3-based test system on a TPX3 ASIC chip to identify the different decay signatures of the radon decay chain through an accurate morphological track analysis that allows the identification of the particles produced by the complex decay chain of ^{222}Rn (Figure 18).
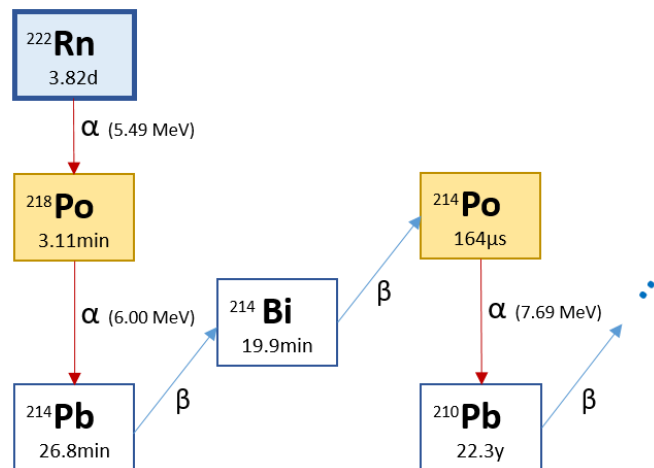
**Figure 18**: Part of ^{222}Rn decay chain and its decay products (alpha particle emitters in yellow).

The measurements were carried out at the NIXT Laboratory (ENEA Frascati) exploiting the presence of natural radon gas by collecting its decay products on the sensor surface. In particular, the detector used in this work is an n-on-p type CdTe

TPX3 with an active volume of CdTe layer thickness of 500 μm and covered by a 100 nm Al layer, which acts as a polarization electrode. The sensor has been biased at - 150V, the optimal observed value to ensure efficient charge collection and minimize electronic noise. The negative bias of this detector produces an electric field near the Al electrode, which can collect positive ions from the radon decay chain [35]. Also, CdTe has a higher density then Si, and this increases the absorption efficiency of more high-energy particles such as beta electrons. TPX3 was used in the frame-based mode that involves a sequence of frames, and each one lasts for a long enough time to distinguish particle tracks on the TPX3 area. Figure 19 shows tracks, in the planes X, and Y of the detector, produced by charged particles; ^{222}Rn is deposited on the detector's surface through dust, and the particles produced in the decays chain are then observed in the same area of the detector. We identified in particular four types of shapes: A) alpha track (circular or "blob-like"); B) gamma or beta track (wavy and thin or "curly"); C) soft and X rays track (point-like track) and D) complex track.
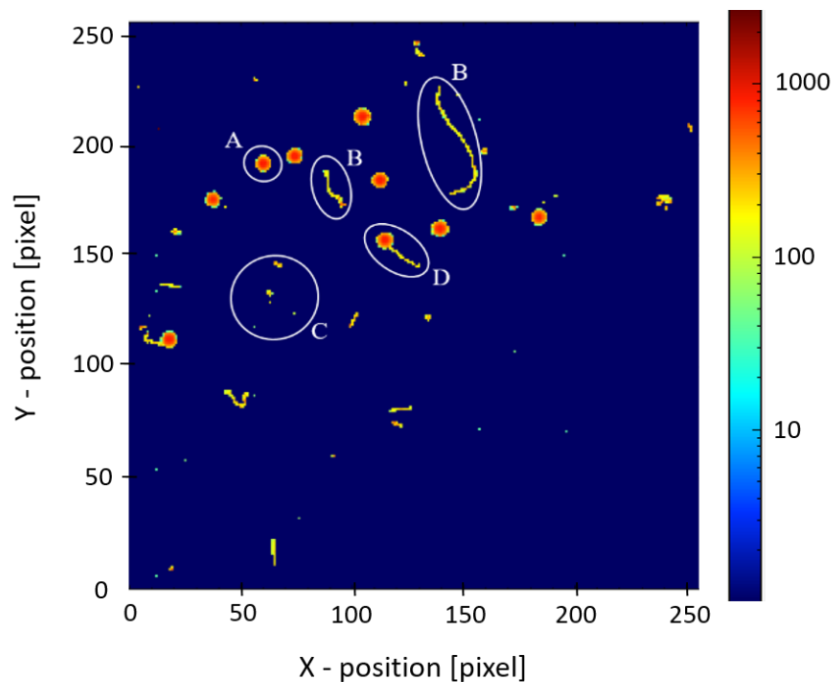

Figure 19: Tracks detected by TPX3: Alpha (A), gamma/beta (B), X-ray (C), and complex tracks (D).

Figure 20 shows a 2D plot of ToT v versus CS in which three distinct populations can be noticed: the first with low CS and low ToTv, due to tracks like B and C in Figure 19. The second and the third correspond to tracks A and D of the same Figure.
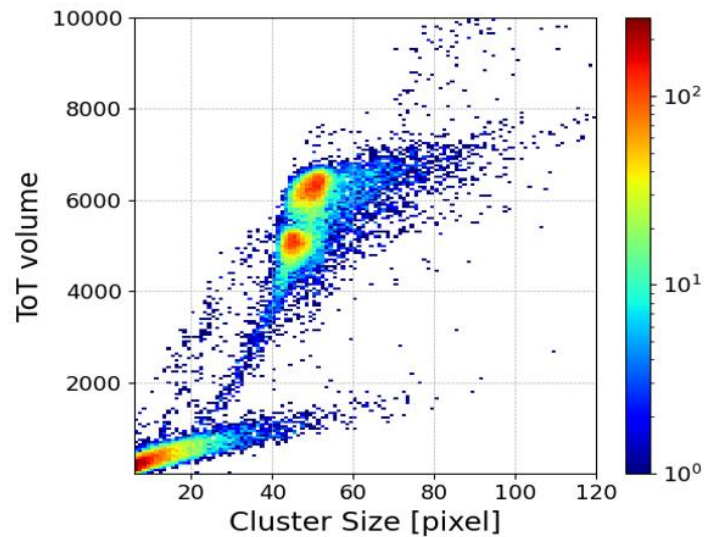

Figure 20: 2D plot of alpha particles from ^{214}Po and ^{218}Po.

In Figure 21, for these last two populations, two peaks in the ToTv distribution can be observed, and they correspond to alpha decays from ^{214}Po and ^{218}Po.
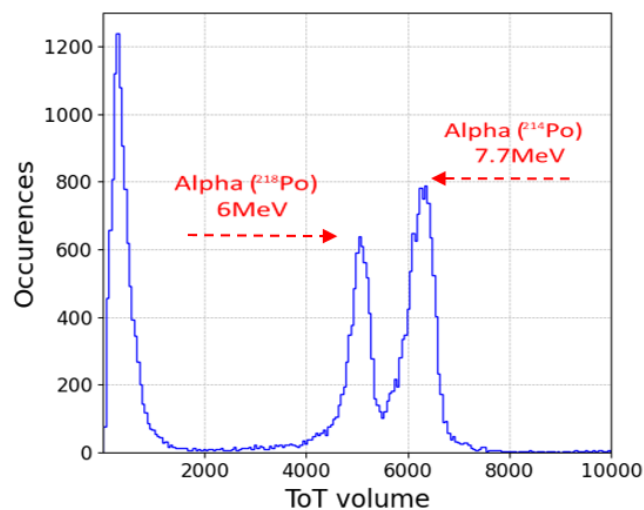
Figure 21: ToT volume distributions show peaks due to alphas of ^{214}Po and ^{218}Po.

Using the detector response in time, it has also become possible to further discriminate the tracks with a relative energy resolution in the 5-10 % range for energies higher than 1.5 MeV. In particular, it has been observed that tracks with tails (such as D) correspond to overlapping two consecutive tracks with a time difference of some hundreds of µs. Thus, using the time differences, it is possible to divide the above single cluster into two distinct clusters: one for the beta track and the other for the alpha track. This is due to the beta decay of ^{214}Bi, followed by the rapid alpha decay of ^{214}Po (Figure 22a). Radon gas is heavier than air and tends to be trapped in confined environments. It reached the TPX3 surface in gas or attached to atmospheric dust [36]. In addition, the produced Po ions are positively charged and are easily collected by the TPX3 surface electric field. In order to investigate this decay, the time differences were calculated for each of these traces, observing how the distribution of Δt follows the typical exponential decay curve with a half-life of 166 ± 4 µs (Figure 22b), in excellent agreement with the half-life of the decay of ^{214}Po, of 160 µs.

(a)   (b)
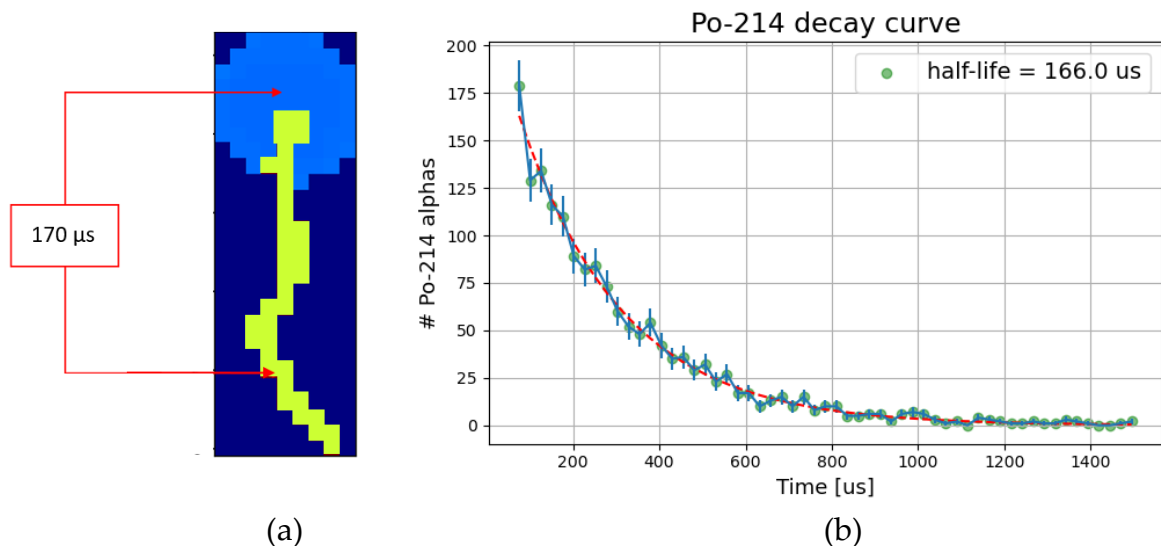
Figure 22: (a) Close-up of a single, highlighted complex track with tail; (b) the half-life of ^{214}Po is 166 ± 4 µs and the dashed red line shows the exponential decay fit of ^{214}Po.

The presented work highlights the performance of the TPX3, showing the significant results that emerge from the morphological and time analysis of the traces; in particular, the time evolution of the events can also be followed for very short intervals, as it has been demonstrated for the decay of the [214]Bi isotope, thanks to the exceptional time resolution of 1.6 ns.

## 3.5.2 Tracks of reaction products by thermal neutrons on [6]LiF converter

The second case study refers to the content of my second paper (A. Tamburrino, G. Claps, G.M. Contessa, A. Pietropaolo, F. Cordella, V. De Leo, R.M. Montereali, M.A. Vincenti, V. Nigro, R. Gatto & D. Pacella, "Thermal neutron detection by means of Timepix3") accepted by the EPJP journal (DOI: 10.1140/epjp/s13360-023-04583-0) [37]. This work shows how the morphological analysis effectively detects thermal neutrons by identifying the products of the $^6Li(n,\alpha)^3H$ reaction [38, 39]. In this case, the TPX3 detector equipped with a converter consisting of a lithium fluoride ([6]LiF) film enriched to 95% with [6]Li (Figure 23) installed at the HOTNES facility [40] in ENEA was used.

(a)   (b)
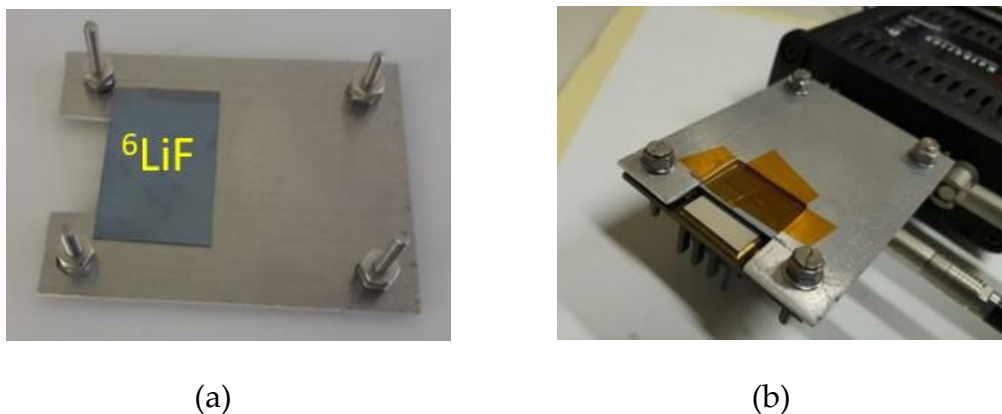
Figure 23: (a) Aluminum mask with [6]LiF layer-coated silicon sheet.; (b) TPX3 with aluminum mask.

The analysis carried out highlighted the performance of the TPX3, showing how the implemented system allows the identification of neutrons through the products of

reactions on ^{6}Li (alphas and tritons). The morphological analysis of the tracks produced by these particles and the measurement in charge allows the evaluation of the presence of neutrons with accurate discrimination from the gamma background, usually due to the neutron activation of the surrounding materials. The image shown in Figure 24 highlights the tracks recorded on the surface of the TPX3 covered by the converter; each appears as a group of adjacent pixels (cluster) and has been identified, choosing the CS, ToTv, and Rnd cluster analysis parameters.
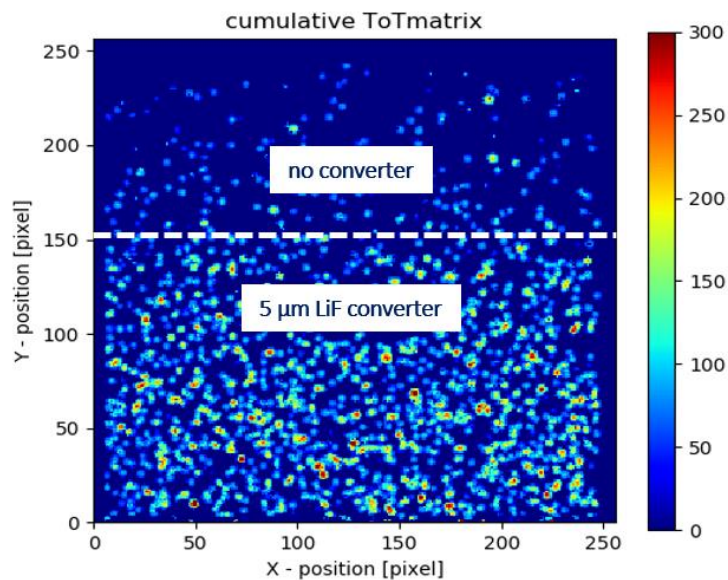

Figure 24: TPX3 image showing the integrated response due to alpha and triton tracks with and without converter.

The 2D histogram of the ToTv as a function of the CS (Figure 25) shows two distributions: one due to the simultaneous presence of tracks from alpha and tritons and the other relative to the presence of tritons tracks only.

46
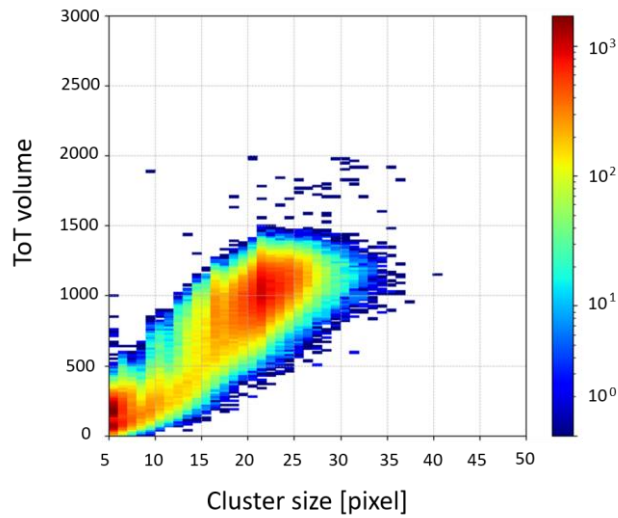
Figure 25: 2D plot distribution after application of filter cluster criteria.

Finally, the 1D histogram of the ToTv (Figure 26) highlights the presence of the two contributions in energy.
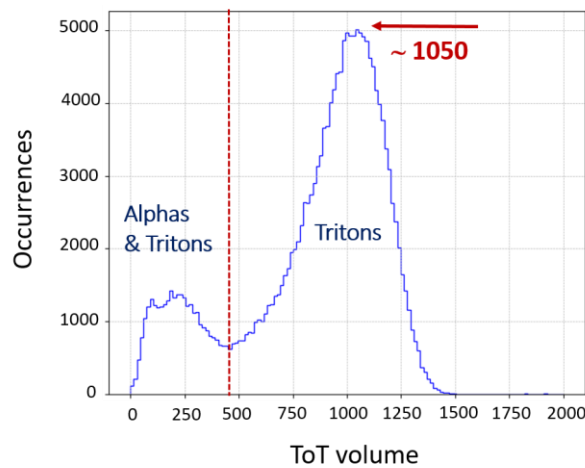
**Figure 26**: ToT volume distributions showing alpha and triton peaks.

With the help of Monte Carlo simulations, it has been shown that the main peak is due to the contribution of tritons. This feature can be used effectively in thermal neutron identification. In the configuration used for this work, the converter has been placed at a 3 mm distance from the detector, obtaining an efficiency of 0.9 % for neutrons of 25 meV.

Chapter 4

Diamond detectors for fast neutron detection

4.1 Diamond properties

Diamond is a very interesting material in neutron diagnostics for fusion reactors. The high radiation resistance and fast response times make it an excellent candidate for environments with a high level of radiation, such as in the vicinity of thermonuclear fusion plants; for the new DTT Tokamak, for example, neutron fluxes up to 2×10^{11} n cm^{-2} s^{-1} are predicted close to the machine. Natural diamond is characterized by inherent variability and scarcity, limiting its use in industrial applications. However, the chemical vapor deposition (CVD) technique makes it possible to produce outstanding synthetic crystal diamonds (both polycrystalline and monocrystalline) [41]. The properties of a diamond derive from its structure: tetrahedral covalent bonds between an atom and its four closest neighbors connected in a cubic lattice. This compact and rigid structure (Figure 27) gives rise to its exceptional properties, in addition to being inert to many chemicals and mechanically robust.
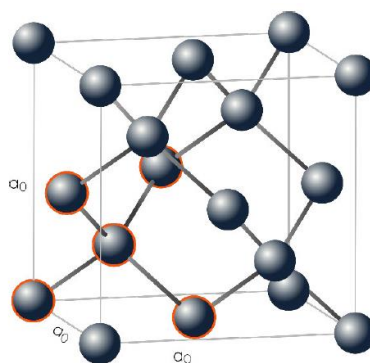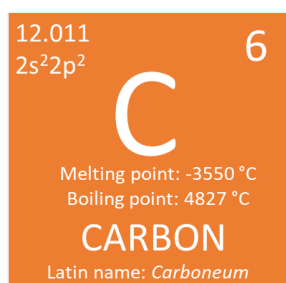
Figure 27: Properties of Carbon chemical element (left) and its schematic solid structure (right).

Diamond can be considered a semiconductor with a high-energy gap (5.5 eV) that enables intrinsic carrier density, which results in a high resistivity (10^{13} Ωcm) and low dark current (less than 1 nA/cm²); therefore, it does not require the realization of a p-n junction, as in the case of conventional semiconductors. It can be polarized with high voltages. It is also characterized by high carrier mobility (e.g., larger than silicon), a high breakdown field, and good charge transport properties (higher electron/hole mobility and fast signals, e.g., compared to silicon). As mentioned, it is a radiation hard material, resistant to high temperatures due to its higher thermal conductivity, and low capacitance due to the low values of the dielectric constant. As a consequence, it has a good signal-to-noise ratio. Table 3 outlines the main outstanding properties of CVD diamond together with those of silicon, the main competitor.

| PROPERTY	SILICON	DIAMOND	DIAMOND
Material	MCz, FZ, epi	Polycrystalline	Single crystal
Displacement [eV]	13-20	43	43
Energy gap [eV]	1.12	5.5	5.5
$E_{breakdown}$ [V/cm]	3×10^6	10^7	10^7
μ_e [cm²/Vs]	1450	1800	>1800
μ_h [cm²/Vs]	450	1200	>1200
Saturate drift velocity [cm/s]	0.8×10^7	2.2×10^7	2.2×10^7
Atomic number Z	14	6	6
Relative dielectric constant (ε_r)	11.9	5.7	5.7
e-h energy [eV]	3.6	13.0	13.0
Density [g/cm3]	2.33	3.51	3.51
e-h/μm for mips	~ 80	36	36
Max *ccd* [μm]	>500	300	800
Thermal conductivity [W/(mK)]	150	~1900	~1900

Table 3: Comparison of characteristic physical parameters for Silicon and Diamond.

Radiation hardness is the most critical property among those summarized in the table. In particular, diamond's radiation hardness comes from its high atomic displacement energy (42 eV/atom) and low atomic number. So, it can demonstrate stable high-sensitivity to radiation compared to other solid states detector materials. Contrary to metals, the high diamond's thermal conductivity is dominated by lattice vibrations (phonons), which also determines a low electrical conductivity. Therefore, its thermal conductivity is ruled by how these are scattered and, at room temperature, related to "Umklapp processes" (phonon-phonon scattering) and defect/impurity dispersion. Moreover, its low atomic number downplays particle scattering and absorption. Since the energy required to produce an electron-hole pair is higher than in diamond, smaller signals are to be expected. Finally, it is necessary to introduce an important figure of merit that characterizes a diamond as a particle detector called "charge collection distance" (*ccd*) which takes into account the defects present in the crystalline structure of the diamond. In the case of polycrystalline diamonds characterized by the presence of defects between the various crystalline grains, this factor has a lower value then the monocrystalline diamond [27]. The *ccd* is related to carrier mobility, and the possible presence of charge traps in the active volume can influence the detector's response with a consequent smaller induced signal. The interaction of a particle inside the diamond produces electron-hole pairs that, due to the polarization field (1 V/μm), move in opposite directions and separate by a characteristic distance that defines the *ccd*. In the case of the polycrystalline diamond, the *ccd* parameter can vary a lot from point to point, and this determines a spread in the measurement of charge that can reduce energy resolution; in these cases, monocrystalline CVD diamond is preferable.

4.2 Diamond as a fast neutron detector

Diamond detectors are among the most used diagnostic devices for fast neutrons. In particular, due to their high radiation hardness, they are proposed for monitoring fast

neutrons on Tokamak machines. Typically, they are artificial CVD single crystal diamonds (briefly SCV) of small volume; at the moment, among the most extended SCV, there are those produced by the Element Six company [42] that can cover an area of 10×10 mm² with a thickness of 500 µm. The most straightforward scheme of a single-channel diamond detector is shown in Figure 28.
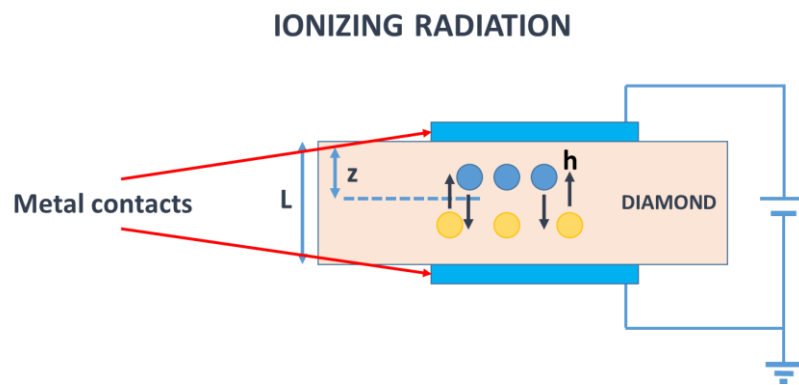
Figure 28: Lay-out of a typical diamond detector with two-terminal device and an intrinsic diamond layer sandwiched between two metal contacts.

The diamond plate is sandwiched between two metal contacts that represent the electrodes where a biasing voltage is applied with typical values from 0.5 to 2 V/µm. The realization of this layout is facilitated by the high resistivity of diamond, and often, the electrodes are made through the combination of different metal layers (Ti/Pt/Au, Cr/Au, and so on) with thicknesses that can range from a few tens to hundreds of nm. The metal–diamond junction can form either Schottky or ohmic contacts; in the second case, the diamond sample must be annealed, and the metal react with the diamond surface and form carbides that realize the contacts [43,44]. For such detectors, a conventional analog electronic circuit was used; typically, it is composed of a preamplifier, a spectroscopic modeling amplifier, and a PC-based multi-channel acquisition system (MCA) with an analog-to-digital converter.

51

In the field of neutron diagnostic for fusion reactors, diamond detectors are also preferred because of the number of reaction channels with charge products that can be exploited. Table 4 highlights the main neutron reactions with diamonds, together with their Q values and threshold energies [45]. Q is defined positive if energy is released by the nuclear reaction, negative if the energy is required; in this second case, a threshold energy is required, higher than the Q values, because of the mass balance of the reactants.

Neutrons - ^{12}C REACTIONS		
Types of reactions	**Q-value (MeV)**	**Threshold energy (MeV)**
^{12}C(n, n)^{12}C	**0.0**	**0.0**
^{12}C(n, γ)^{13}C	4.95	0.0
^{12}C(n, α)^{9}Be	**-5.70**	**6.18**
^{12}C(n, n' 2α)^{4}He	**-7.27**	**7.89**
^{12}C(n, n' α)^{8}Be	-7.37	7.99
^{12}C(n, 2α)^{5}He	-8.16	8.85
^{12}C(n, p)^{12}B	-12.59	13.64
^{12}C(n,d)^{11}B	-13.73	14.89
^{12}C(n, n'p)^{11}B	-15.96	17.30
^{12}C(n, 2n)^{11}C	-18.72	20.30
^{12}C(n, T)^{10}B	-18.93	20.52

Table 4: Neutron-^{12}C reactions for neutron energy up to 20 MeV.

As shown in the table, some of these reactions produce only charged particles in the final state, which is an excellent advantage for spectroscopic analysis.

The neutron-carbon scattering reactions are shown in Table 4, and it has also presented a scale of increasing activation energy levels required to initiate the different reactions in diamond. Of these reactions, the most used ones are elastic neutron scattering (the first one in the table 4) for 2.5 MeV neutrons and the fourth and fifth for 14.1 MeV neutrons. The first reaction involves the recoil of the carbon atom, which then ionizes the diamond. In contrast, in the fourth and fifth reactions, the reaction products (alpha and Be) transfer their kinetic energy to the diamond, causing ionization. Besides these, other reaction channels that have charged particles as products, with energies up to 20 MeV, can be exploited. For example, the pulse height spectrum (PSH) as measured for 13.8 MeV neutrons is shown in Figure 29 [46].
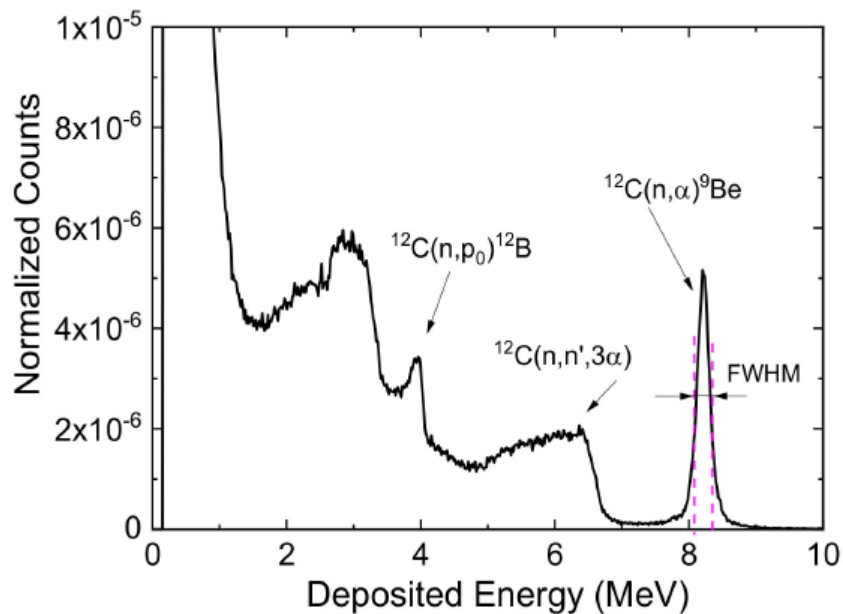
Figure 29: Pulse height spectrum (PHS) with highlighted main reactions for a diamond detector irradiated by 13.8 MeV neutrons.

Different reaction contributions can be observed, in particular, the peak due to the α and ^{9}Be products that typically is used for spectroscopy of neutron energies higher than 6.2 MeV, the edge due to 3α reaction, and the small peak due to p and ^{12}B reaction

products superimposed to a continuum coming from the elastic interaction with carbon ions. A crucial point for this type of detector regards its capability to discriminate neutron signals from other possible background contributions, especially to gamma. Often, n/γ discrimination is based on the pulse shape analysis (PSA): it has been observed that the current pulse induced from the drifting electrons and holes produced in the crystal after a particle interaction has a shape that depends on the distribution of ionization inside the crystal. Comparing n and γ interaction, some authors [47] distinguish between "point-like" and "track-like" ionization: the first refers to short-range charge particles like those produced by some nuclear reaction in diamond, the second refers to long-range charge particles like the Compton electron produced after gamma interaction. As shown by several authors, the corresponding measured signals have different characteristic shapes. Consequently, appropriate algorithms have been developed to distinguish them and separate the gamma contribution. PSA is a methodology commonly used for other neutron detectors to separate the gamma component and distinguish charged products from different neutron reactions.

4.3 "Diamondpix" prototype realization

The new diamond detector arises from the idea to combine the well-known peculiar characteristic of the diamond as a neutron detector with the electronic performances of the TPX3 chip. In particular, as explained extensively in paragraph 3.2, the peculiarity of the TPX3 chip is that, pixel by pixel, it can provide a simultaneous measurement of counting, charge, and time of arrival (for a reference time) of the particle that interacts and releases a given amount of charge. Similar to semiconductor TPX3 detectors, coupling between diamond and chip is realized through the bump-bonding technique. The prototype was realized with a polycrystalline diamond having an area of 10×10 mm^2 and a thickness of 500 μm. This is a standard commercial CVD diamond produced by the Element Six company, while the bump-bonding coupling

was realized by the German company IZM. One side of the diamond plate has been covered with a matrix of 20 × 20 μm² metalized areas with a pitch of 55 μm (Figure 30a). For each metallization, a tin sphere of 25 μm diameter welds the diamond to the underlying chip pixel channel. In this case, the difficulty arises from the realization of the metalized area: it was necessary to evaluate the best alloy (Cu/Cr) to have a stable contact and ensure charge transport.
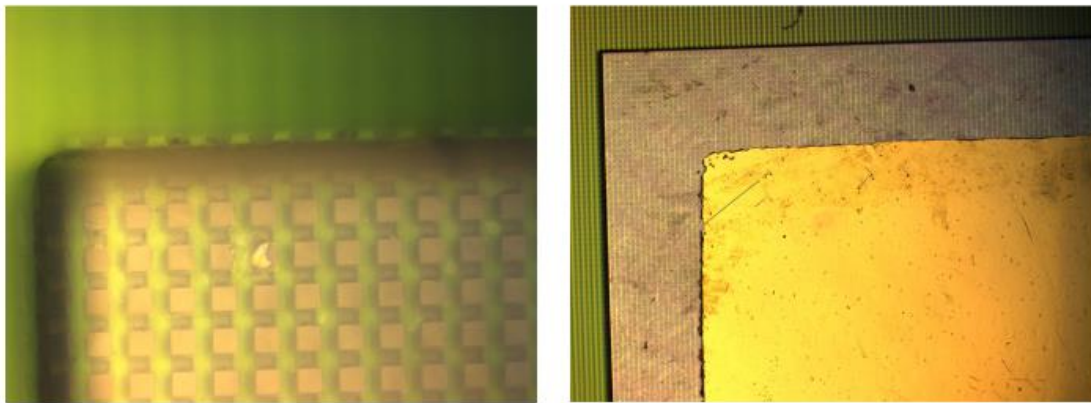

<center>(a)   (b)</center>

Figure 30: (a) One side of the diamond plate bonded to a metal grid; (b) the other side covered by a gold thin layer.

The other side of the diamond plate has been covered by a gold 300 nm thin layer (Figure 30b) to apply a polarization bias voltage to the diamond, and it covers the diamond area of 9.9 ×9.9 mm² (Figure 33a). The TPX3 chip bonded to the sensor is mounted on a PCB board which provides additional electronic components to manage the chip electronics, as shown in Figure 33b.
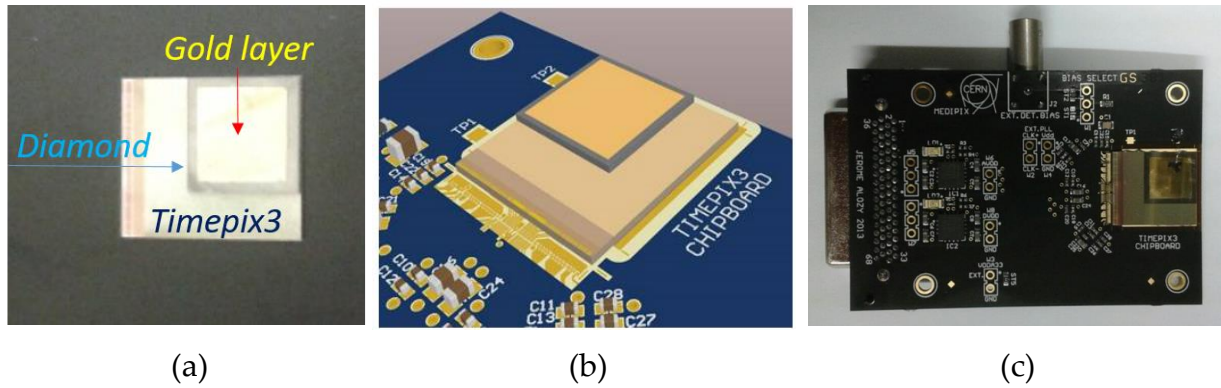
Figure 31: (a) Picture of 300 nm thin layer that covers 9.9 ×9.9 mm² of the diamond area; (b) 3D CAD drawing of the TPX3 and electronics system; (c) picture of Diamondpix.

As a result, a 2D pixelated diamond detector has been obtained with a spatial resolution of 55 μm. Even if a polycrystalline diamond could not be the optimal choice, it has been used because coupling a diamond to TPX3 was the first attempt to demonstrate the realization of a pixelated diamond and a polycrystalline diamond had a significantly lower cost.

## 4.3.1 Diamondpix working conditions and energy calibration

According to the usual standard procedure used for semiconductor TPX3, as presented in paragraphs 3.3 and 3.4, the first step was a threshold equalization procedure. It was observed that keeping all the other setting parameters as for CdTe (in particular Ikrum 5), the best optimal value to cut electronic noise had the same value as applied to CdTe. In order to evaluate the optimal bias voltage, a scan in bias has been performed under irradiation of the detector with an X-ray tube. X-ray photons are entirely stopped in the diamond, and the number of absorbed photons is the same as the injected one. After this test, it was evaluated that the best minimal bias voltage is 300 V, corresponding to an electric field of 0.6 V/μm. As observed on X-ray lines and due to the granular structure of the polycrystalline diamond, the expected

spread pixel by pixel is not negligible; then, differently from the global calibration presented for the CdTe TPX3, an energy calibration pixel by pixel was preferred. In this case, the diamond was completely irradiated by mono-energetic X-ray lines produced by the fluorescence of specific materials excited by an X-ray tube. Targets of Zirconium, Molybdenum, and Silver have been used, which provided X-ray energies of 15.8 keV, 17.5 keV, and 22.2 keV, respectively. The calculation of the pixel-by-pixel calibration curves has been performed using a dedicated analysis software developed by the group of IEAP of Pilsen University. It is a mathematical function of ToT versus energy:

$$ToT(E) = aE + b - \frac{c}{E - t}$$

where the coefficients a, b, c, and t are determined pixel-by-pixel. For example, Figure 32 shows the standard calibration curve on a selected pixel.
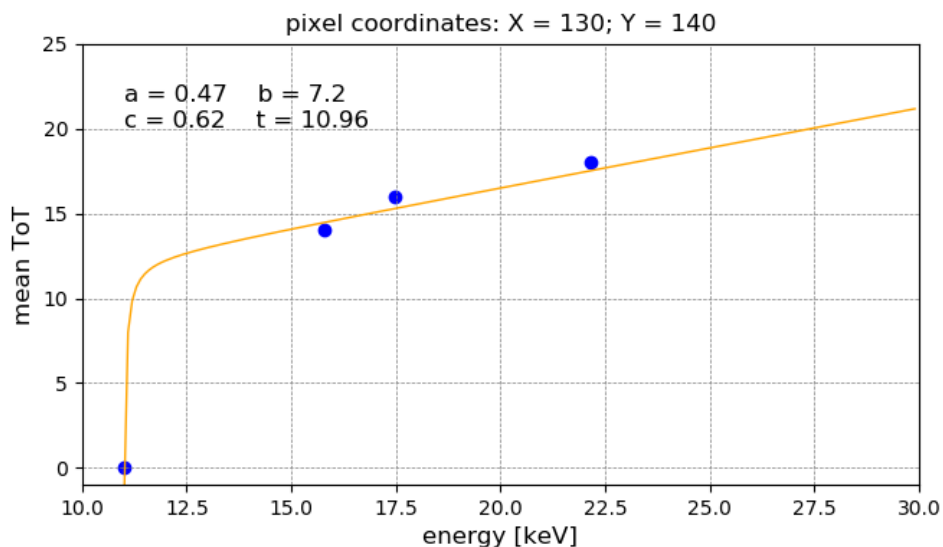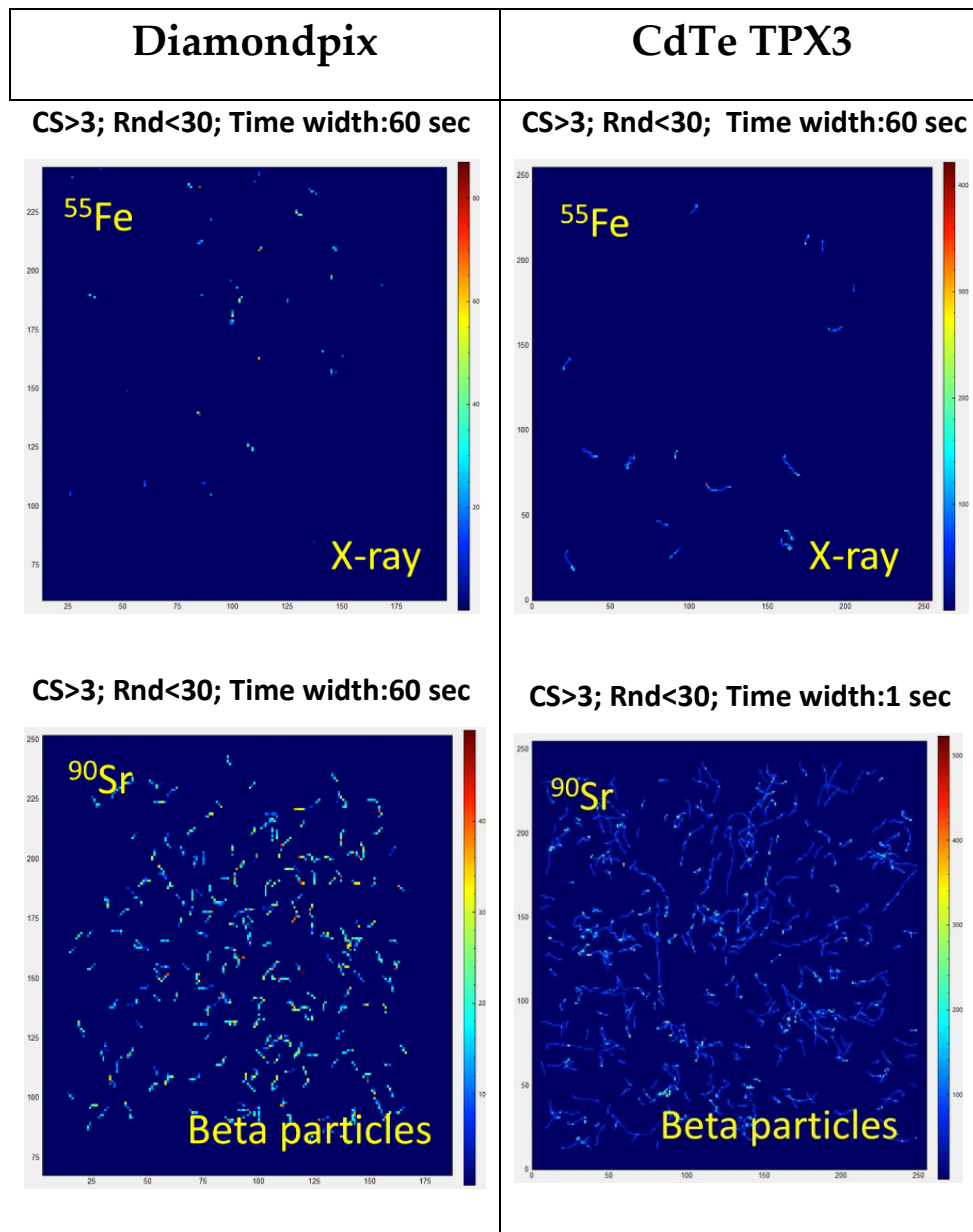

Figure 32: ToT\energy calibration of the Diamondpix using the fluorescent lines from Zr, Mo and Ag for a specific single pixel.
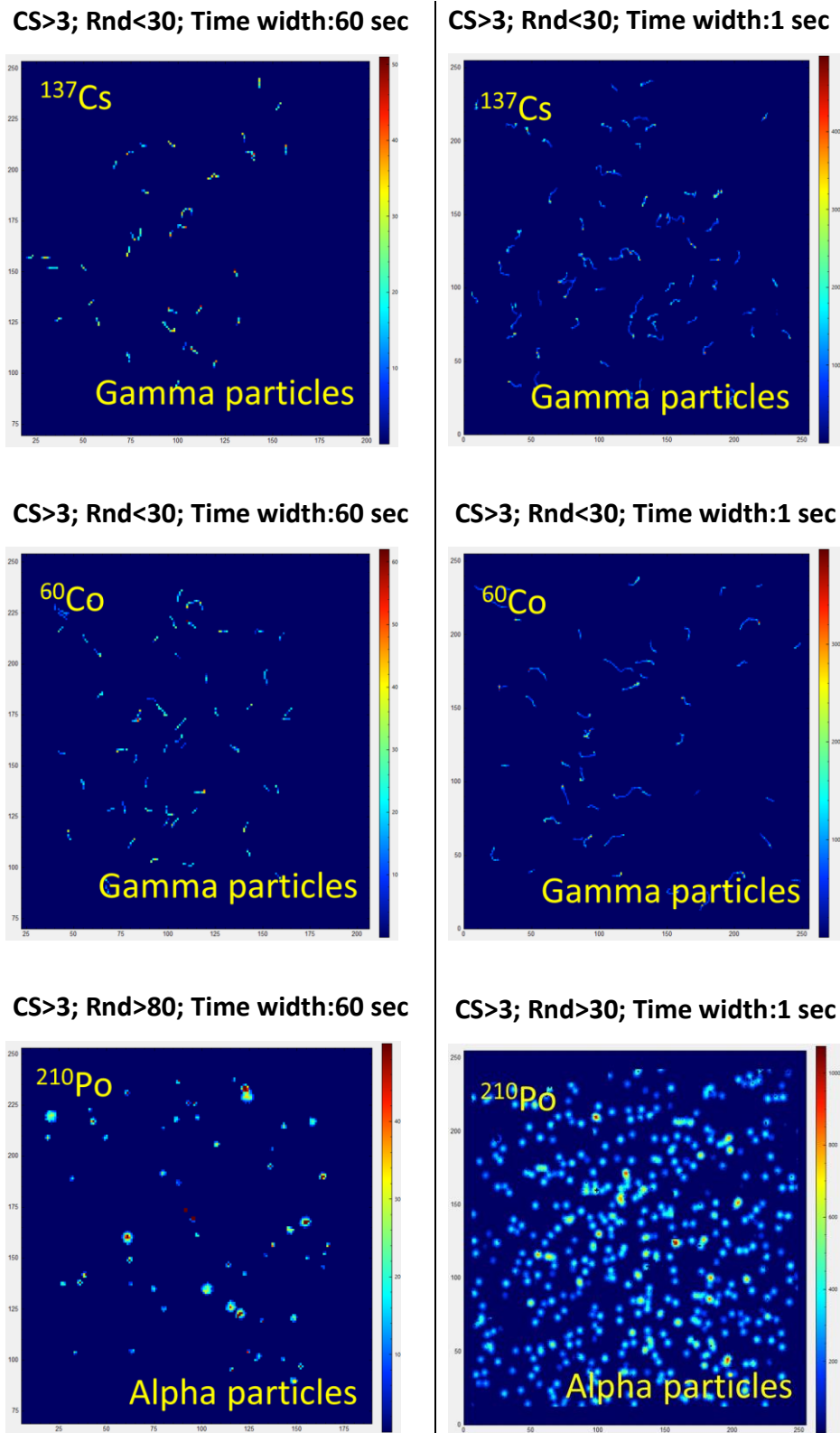
The threshold energy value at ToT = 0 has been set equal to 11 keV. This value has been calculated taking into account the ratio between the ionization energies of diamond (13 eV) and Si (3.6 eV) and multiplying this ratio with the minimum threshold energy for Si TPXs of about 3 keV. In order to check the Diamondpix response to higher energies, calibration has been applied to measure the energy of collimated alphas coming from a lab ^{210}Po source. However, the alpha measured energy is lower than the expected value; these results confirm that calibration curves obtained for low energies cannot be used for the measurement of higher charge value and then for heavy charged particles. To find the optimal calibration curve for these higher energy ranges, a procedure similar to that used for CdTe has been repeated for Diamondpix, but the corresponding ToT distributions had a very large spread, and a clear peak could not be observed. This anomalous distribution is probably due to two reasons: the presence of a non-uniform gold electrode and the granular structure of polycrystalline diamond. In the first case, the alpha particle loses a different amount of energy depending on the entrance position on the gold surface. In the second case, as alphas are absorbed in the first layers of the diamond (less than 30 µm), the released charge must drift along the whole diamond thickness, and then the probability of losing the primary charge is higher. This hypothesis is also in agreement with the lower value of *ccd* value (300 µm) with respect to the diamond thickness.

4.3.2 Track analysis with Diamondpix

Diamondpix has been conceived as a 2D diamond detector and, thanks to its high spatial resolution, it opens the possibility to alternative use with respect to the standard single-channel diamond detectors. Like the usual semiconductor TPX3, depending on the type and energy of the interacting particle and the diffusion of the charge (electrons/holes) inside the Diamond, for each interaction, a cluster of pixels of a given shape will be observed. Applying some specific morphological parameters and

adding spectroscopic information coming from charge measurements, it is possible to realize a multi-parametrical analysis that can improve the identification of different types of particles with different energies. In order to verify its track response, this prototype was initially tested with laboratory radioactive sources. Figure 33 shows some morphologies obtained with Diamondpix compared with TPX3 CdTe detector after the interaction with different types of particles.

CS>3; Rnd<30; Time width:60 sec **CS>3; Rnd<30; Time width:1 sec**

CS>3; Rnd<30; Time width:60 sec **CS>3; Rnd<30; Time width:1 sec**

CS>3; Rnd>80; Time width:60 sec **CS>3; Rnd>30; Time width:1 sec**

Figure 33: Different types of track morphologies observed with Diamondpix (left) and CdTe (right) detectors using the same particle lab sources: ^{55}Fe (5.9 keV X-rays), ^{90}Sr (546 keV beta particles), ^{137}Cs (662 keV gamma particles), ^{60}Co (1.17 e 1.33 MeV gamma particles) and ^{210}Po (5.4 MeV alpha particles).

Therefore, it is possible to exploit these morphological features to define suitable parameters that can more comprehensively characterize the detector response for the neutron spectrum of a fusion reactor. As it can be observed in the case of alpha and gamma sources, the tracks are localized in the first case and extended in the second case. This is similar to the concepts of point-like and track-like used in the PSA and Diamondpix, being a 2D detector, clearly shows the ionization distribution inside the diamond thus offering an alternative methodology to discriminate particles.

Chapter 5

# Diamondpix response characterization with fast neutrons at the FNG and n_TOF facilities

5.1 The FNG facility and the experimental set-up

FNG (Frascati Neutron Generator) is a neutron generator installed and operating at ENEA Frascati Research Centre. It is based on an electrostatic accelerator of ions (D) against a D or D-T target. It produces monochromatic 2.5 MeV and 14.0 MeV neutrons via the D-D and D-T fusion reactions, respectively. Neutron emission is isotropic and can reach an emission rate of 10^9 n/s for the first reaction and 10^{11} n/s for the second one [48,49]. The schematic layout of FNG plant with its main components is shown in Figure 34.
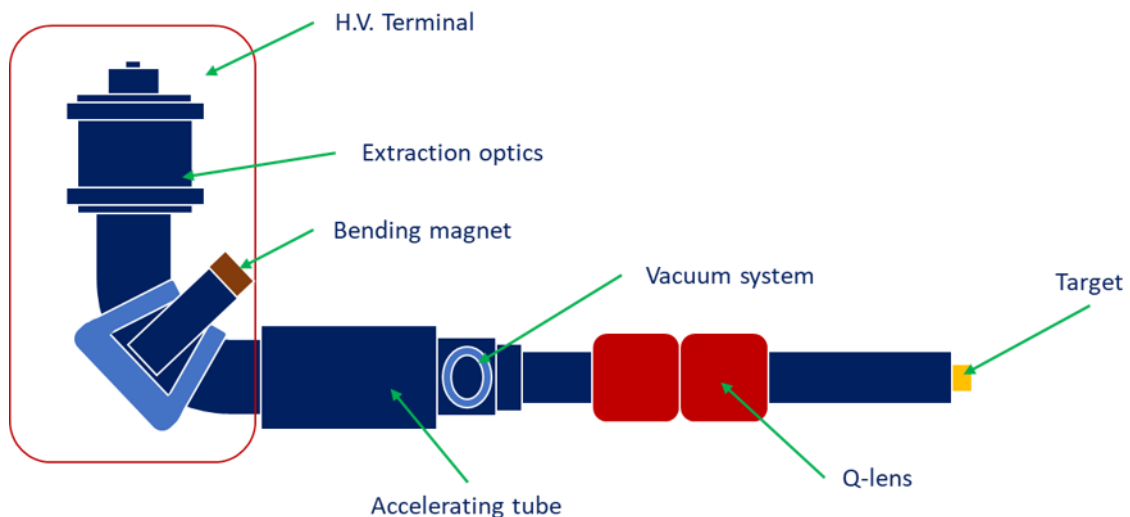
Figure 34: Schematic layout of the FNG facility showing the system's main components based on an electrostatic accelerator.

Measurements at the FNG facility have been performed in two experimental sessions, one with neutrons at 14 MeV and the other at 2.5 MeV. In both cases, the Diamondpix was placed as close as possible to the source (target) to maximize the irradiated neutron flux. Figure 35 shows the experimental setup during the 14 MeV neutron measurement campaign. The Diamondpix was placed at a distance of 11 cm with an angle less than 30° with respect to the deuterons beam direction.
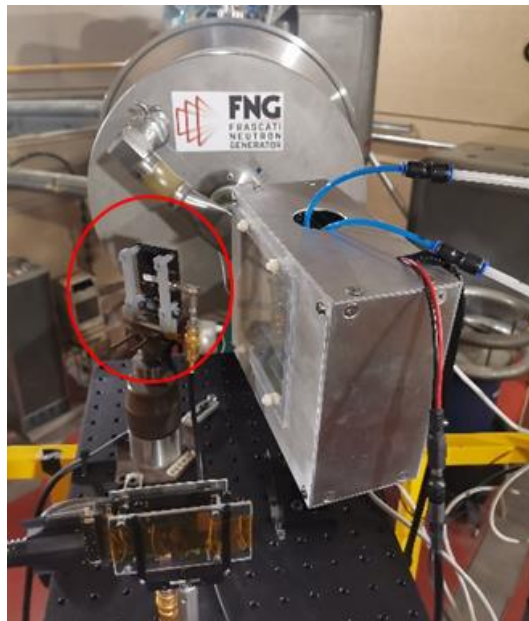

Figure 35: Experimental set-up on the FNG facility; a red circle highlights Diamondpix.

Another important consideration was the location of the Katherine control module for the neutron source. Preliminary measurements with the module directly connected to the TPX3 board showed evident acquisition problems, mainly due to the interaction of the internal FPGA board with neutrons. To avoid these problems, the Katherine module was placed about 2 m from the detector and connected through an appropriate cable. The ability to remotely read out electronics is an important advantage for fusion reactors, especially in future tokamaks where a high neutron flux is expected. Measurements on 2.5 MeV neutrons were performed in a later experimental session.

The Diamondpix was placed at a distance of 9 cm with an angle of about 0° relative to the deuteron beam direction.

5.1.1 Study of the Diamondpix response to 2.5 and 14 MeV neutrons

Measurements at the FNG facility provided indications of the track typology due to neutron interactions at energies of 2.5 and 14 MeV. For illustration purposes only, Figure 36 shows the typical observed tracks distributed on the diamond surface, after irradiation with 2.5 and 14 MeV neutrons at the FNG facility in small time windows.
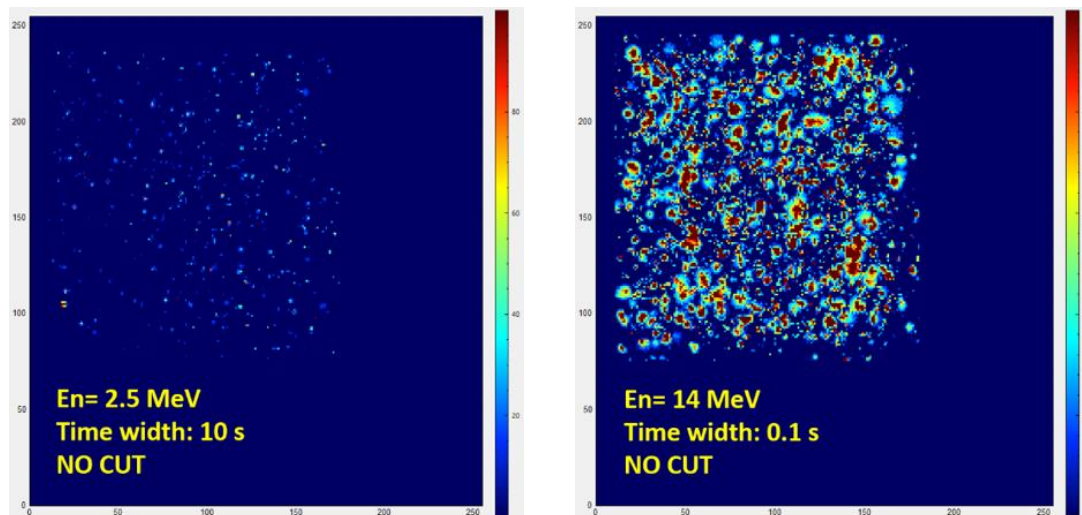

Figure 36: The typical observed tracks after neutron irradiation with 2.5 and 14 MeV neutrons on the FNG facility.

According to a previous work [27] on this same detector, tracks produced by neutron interactions can be discriminated from the gamma background by applying a cutting line in the CS-Rnd plane that defines two regions, one for neutron tracks and the other for gamma tracks. The line is defined by a value of 20 on the CS y-axis and 125 on the Rnd x-axis. These values have been defined after a separate track analysis on gamma and alpha sources. Figure 37 shows the distribution of neutron and gamma tracks in the CS-Rnd plane after applying the line cut. In the analysis presented in this chapter,

Rnd has been calculated according to the second definition of paragraph 3.4. The choice is justified by the more reasonable values assigned to low CS clusters with respect to the other presented definition. The red straight line separates the tracks due to neutrons (blue dots at the upper region) from the background (red dots at the lower region).
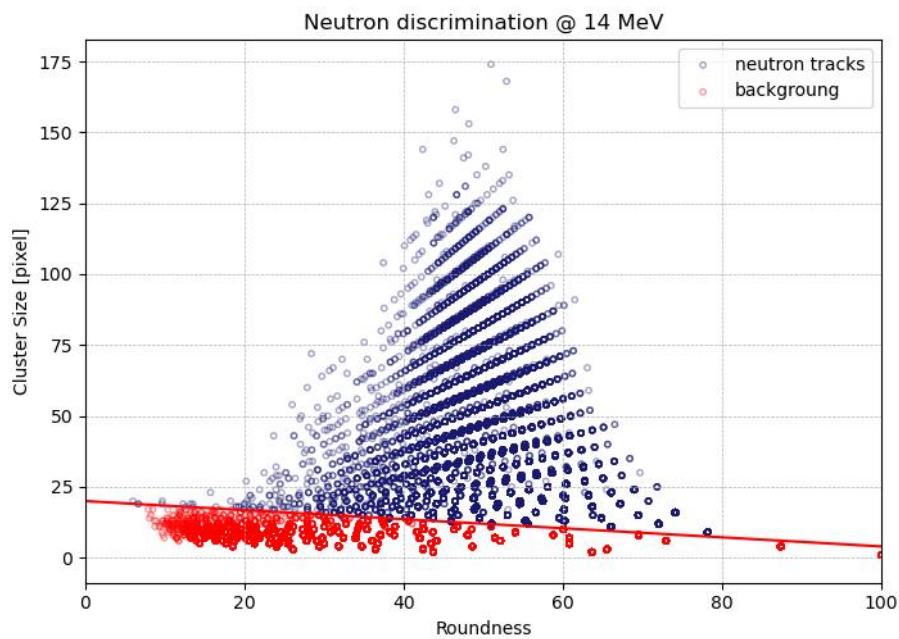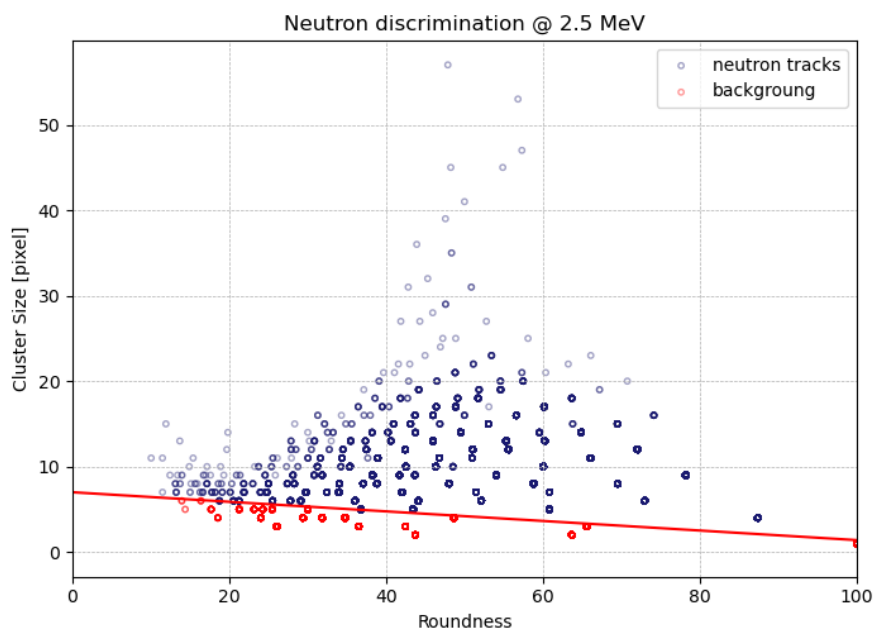

Figure 37: Distribution of 14 MeV neutron tracks in the CS-Rnd plane in the CS-Rnd plane with the defined cut line that separates the plane into two regions: background with gamma photons tracks (red points) and neutron region with tracks coming from neutron reactions (blue points).

By way of illustration, figure 38 shows the Diamondpix surface with all the detected tracks with no cuts and after applying the line cut.
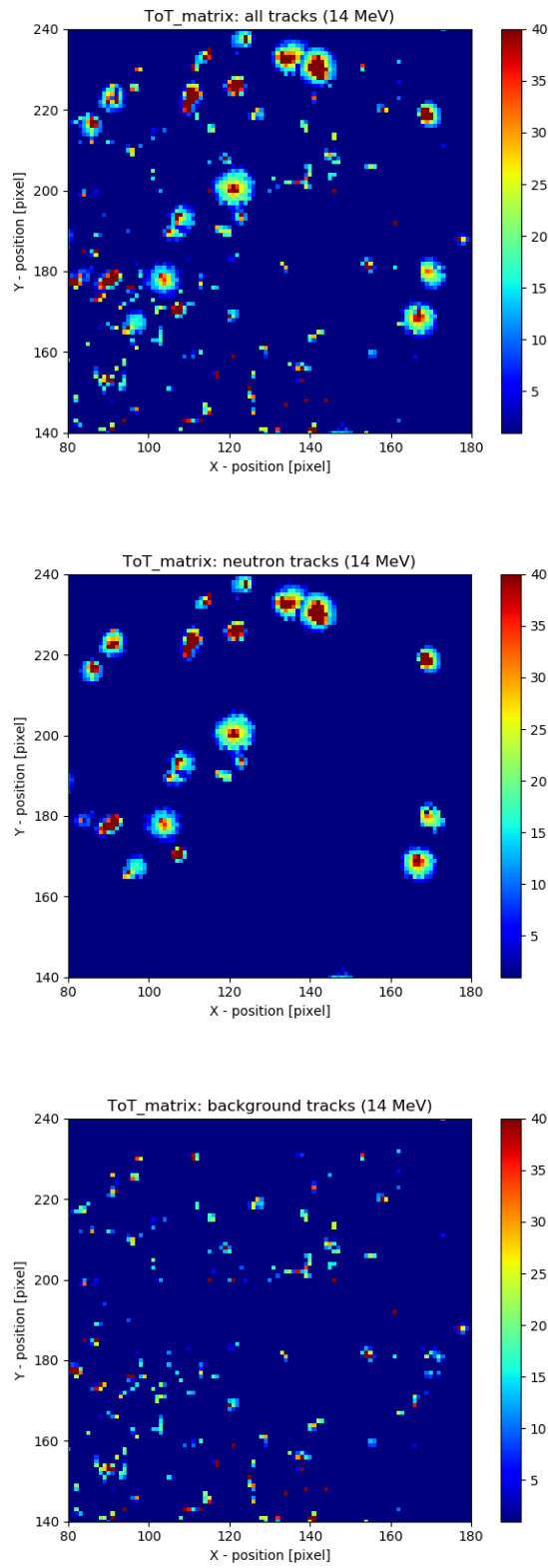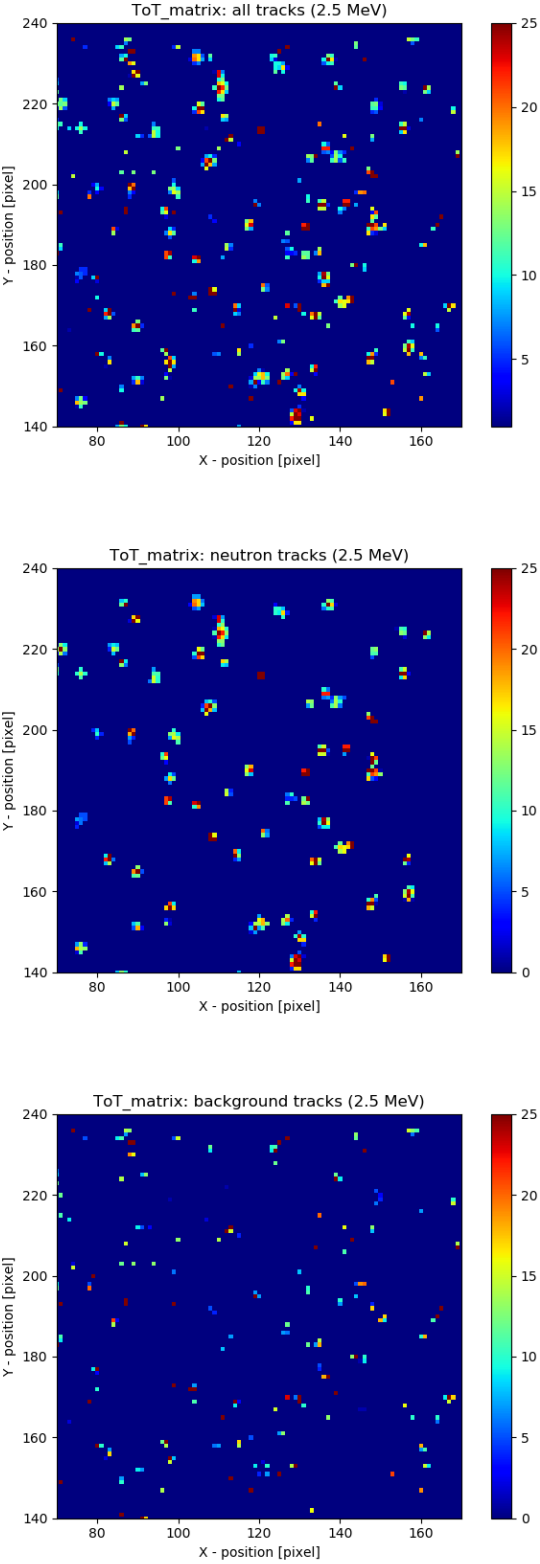
Figure 38: Cumulative ToT matrix acquired in 15 ms with all detected tracks and the same matrix in the neutron and gamma regions.

When the defined criterion is applied and only the neutron region is considered, all characteristic tracks due to neutron interactions can be observed. Consequently, when the gamma region is selected, characteristic tracks due to gamma interactions can be observed. It must be highlighted that a small fraction of neutron tracks can fall in the gamma region: some of the charged light particles (like alphas and protons) and the residual nucleons produced by neutron interactions can escape the diamond, releasing a fraction of their charge, or can have very low energy, turning on only a few pixels with low charge. In this case, these tracks cannot be easily recognized, so excluding them from the analysis was preferable. The 2-D plots in Figure 38 show the effect of applying this discrimination criterion to the data, and the difference between blob tracks (characteristic of neutron interactions) and curly and point tracks (characteristic of gamma interactions) is evident. For 2.5 MeV neutrons, a similar criterion has been applied. However, the y-intercept of the line is now 7, about three times smaller than the value used for 14 MeV neutrons. Figure 39 shows the defined neutron and gamma regions for the 2.5 MeV neutrons.

Figure 39: Distribution of 2.5 MeV neutron tracks in the CS-Rnd plane with the defined cut line that separates the plane in two regions: background with gamma photons tracks (red points) and neutron region with tracks coming from neutron reactions (blue points).

Figure 40 shows the effect of this criterion for this neutron energy similar to Figure 38.

Figure 40: Cumulative ToT matrix acquired in 500 ms with all detected tracks and the same matrix in the neutron and gamma regions.

In Figure 40, as expected, the CS and ToTv are smaller than the 14 MeV neutrons. In fact, for 2.5 MeV neutrons, interactions in diamond produce only recoil of carbon ions with a broad energy spectrum, ranging from the energy cutoff of diamond to a maximum recoil energy of about 0.7 MeV. In this case, discrimination against background is more complicated. Paragraph 5.2.2 will explain the cluster analysis that justifies the cut values applied for 2.5 MeV neutrons.

5.1.2 Estimate of the neutron efficiency at the two energies

The first tests performed with this new detector on the FNG facility not only provide a characterization of its response regarding track morphology and charge distribution, as explained in the previous paragraph, but also provide an estimate of the detector efficiency for the two neutron energies produced in conventional fusion reactors. It is crucial to outline that track analysis has been made easier and faster using the MMTrackLab data acquisition program: it acquires data in data-driven mode, and each cluster is separately recorded, making it possible to cover the high fluxes expected at the FNG facility. In particular, during the first conducted experiment, Diamondpix was installed at a distance of about 11 cm from the 14.0 MeV neutron source. The neutron flux was tuned from about 6.0×10^8 to 1.6×10^{10} neutrons/s (n/s) over the 4π solid angle. Then, the neutron flux reaches the detector surface of 9×9 mm^2 spans from 3.2×10^5 to 8.5×10^6 n/s. Taking into account these values, the experimentally measured efficiency at 14 MeV can be calculated as the slope of the straight line (Figure 41) fitting the neutron detected counting rate versus the incident neutron flux obtaining a value of *2.5 ± 0.1 ‰*. This result has been determined by applying the same cuts on CS and Rnd set by the cut line shown in Figure 37, where the upper half-plane defines the neutron identification region.
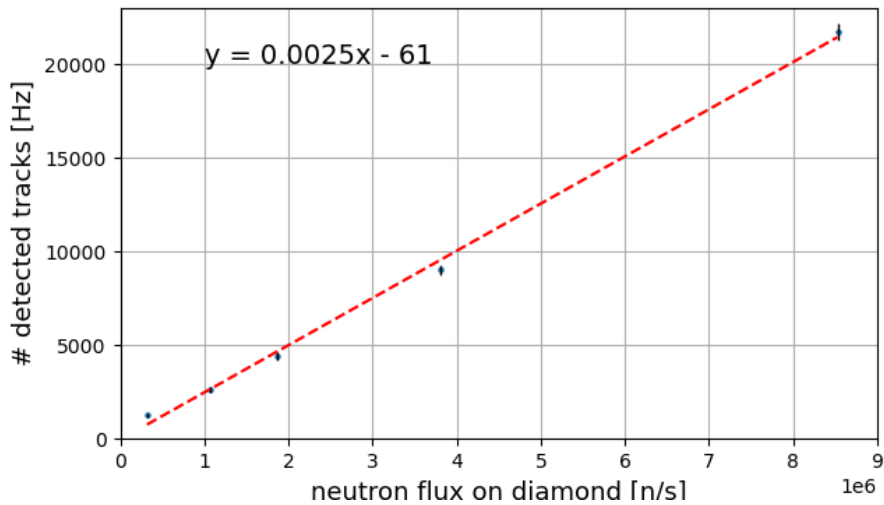
Figure 41: Occurrences of selected neutron tracks as a function of the incident neutron flux on the Diamondpix area. Tracks have been selected according to the criterion presented in Figure 38, and the error bars are calculated as the square root of the occurrences. The trend is linear, and the slope of linear fit provides the Diamondpix efficiency for 14 MeV neutrons.

A similar procedure was applied for 2.5 MeV neutron measurements. However, the maximum CS value that defines the line at 14 MeV has been properly adjusted, considering the trend of the average CS values as a function of neutron energy, as shown in paragraph 5.5.2. It has been observed that the maximum CS at 2.5 MeV is a factor of 3 lower than that observed at 14 MeV, and consequently, all the CS values that define the line in the CS-Rnd plane were scaled by a factor of 5. As a result, the experimentally measured efficiency at 2.5 MeV was *6.8 ± 0.5 ‰* as shown in Figure 42. Measurements were performed during a second experimental FNG campaign where a D target was used. In this case, the neutron flux was scanned from 2.1×10^8 to 2.5×10^8 n/s.
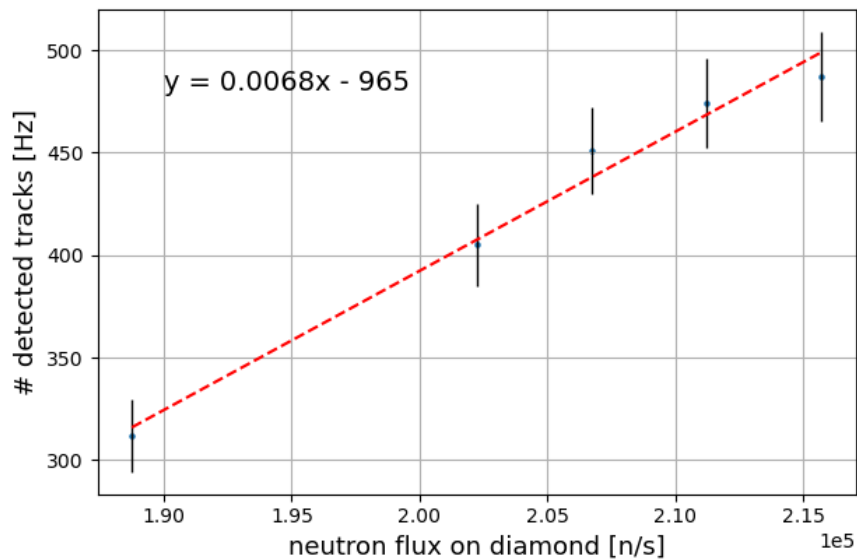
Figure 42: Occurrences of selected neutron tracks as a function of the incident neutron flux on the Diamondpix area. Tracks have been selected according to the criterion presented in Figure 38, and the error is calculated as the square root of the occurrences. The trend is linear, and the slope of linear fit provides the Diamondpix efficiency for 2.5 MeV neutrons.

As it can be observed, the efficiency for 2.5 MeV neutrons is higher than that for 14 MeV neutrons. According to typical measured values on conventional diamond detectors, a higher value was indeed expected for 2.5 MeV neutrons. In this case, however, discriminating neutron tracks from gamma photon tracks is more complex, especially for low-energy carbon recoil ions that can be confused with photon tracks. For high-energy tracks, the applied cut selects neutron tracks more effectively due to the observed higher CS, which allows more accurate discrimination. However, also this cut can result in the rejection of more neutron tracks.

5.2 The n_TOF facility and the experimental set-up

A remarkable part of the characterization work of the Diamondpix detector has been performed at the CERN n_TOF neutron facility. Measurements took place during the last two weeks of the CERN run planned for the year 2022, in which I actively participated. During my approximately two-month stay at CERN, I had the opportunity to conduct measurements and follow the experimental activity on the n_TOF facility. CERN (the European Organization for Nuclear Research) is one of the world's largest and most respected centers for scientific research consisting of a complex system of accelerators of increasing energies which, used in cascade, can produce extremely high energy particle beams (Figure 43). Each machine injects its beam into the next machine, which, in turn, accelerates it to a higher energy. The last element of this chain is the LHC, in which each of the two circulating beams, injected in opposite directions, can be accelerated up to an energy of 7 TeV. The Large Hadron Collider (LHC) is the largest and most powerful particle collider ever built. It is a collider, i.e., a ring in which two protons beams are injected, kept on circular trajectories to circulate in opposite directions and subsequently accelerated [50]. The LHC is located in a tunnel with a circumference of 27 km, located approximately 100 m underground the countryside surrounding Geneva, straddling the Franco-Swiss border.
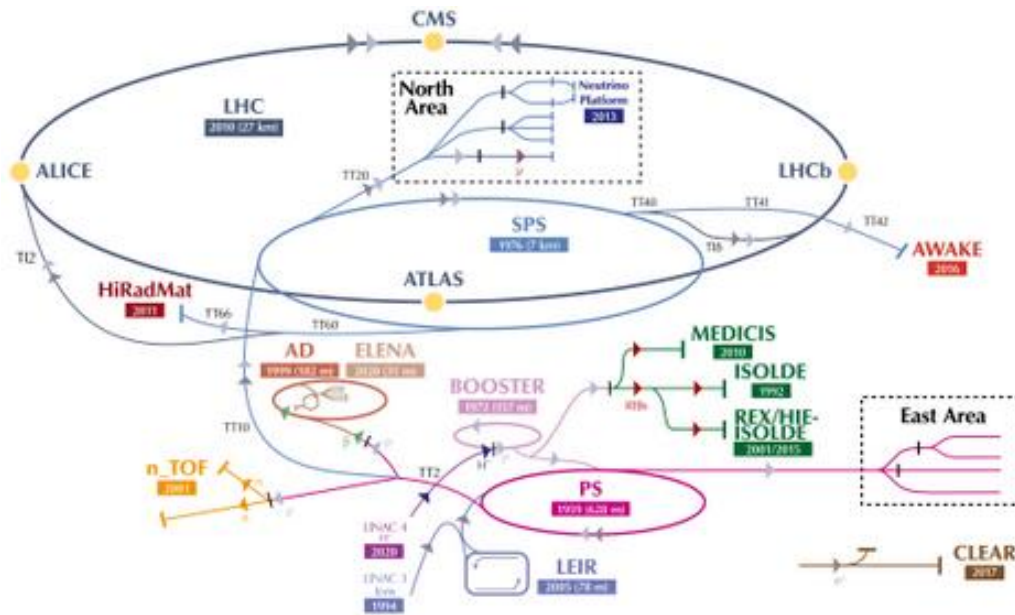
Figure 43: The CERN accelerator plants that highlight the principal experiments and the smaller ones. Among these is the n_TOF facility (in yellow) on the ProtoSynchrotron (PS) exit.

Most of the accelerators in the system have their experimental area where the beams can be extracted and used to conduct experiments at energies lower that the maximum. The beam production starts from atomic hydrogen gas, coming from a small cylinder, from which the electrons are stripped. What remains are hydrogen nuclei, i.e., protons, which are injected in packets (bunches) into a linear accelerator, bringing them to an energy of 50 MeV. These protons are then injected into a small proto-synchrotron, the PS Booster (PSB), accumulating them in four distinct overlapping rings and accelerating them up to 1.4 GeV. The beam is then transferred to the ProtoSynchrotron (PS), which brings it to 25 GeV of energy, and then injected into the Super ProtoSynchrotron (SPS), where it will be accelerated up to 450 GeV. At this point, the beam is injected into the LHC. In particular, the acceleration chain involving n_TOF is the **Linac-Booster-PS**. The n_TOF facility is a pulsed neutron source: neutrons are produced through the spallation process by a pulsed proton beam (with energy of 20 GeV/c) from CERN's PS that impinges on a lead target producing about 300 neutrons per incident proton. The target is coated with a borate water moderator layer that

moderates the initially fast neutrons. This ensures a large energy range for the neutron beam with values ranging from meV to GeV. Then, the neutron source corresponds to the target where the neutron beam is produced. N_TOF hosts two neutron beam lines with their respective measurement stations (EAR1 and EAR2), as shown in Figure 44.
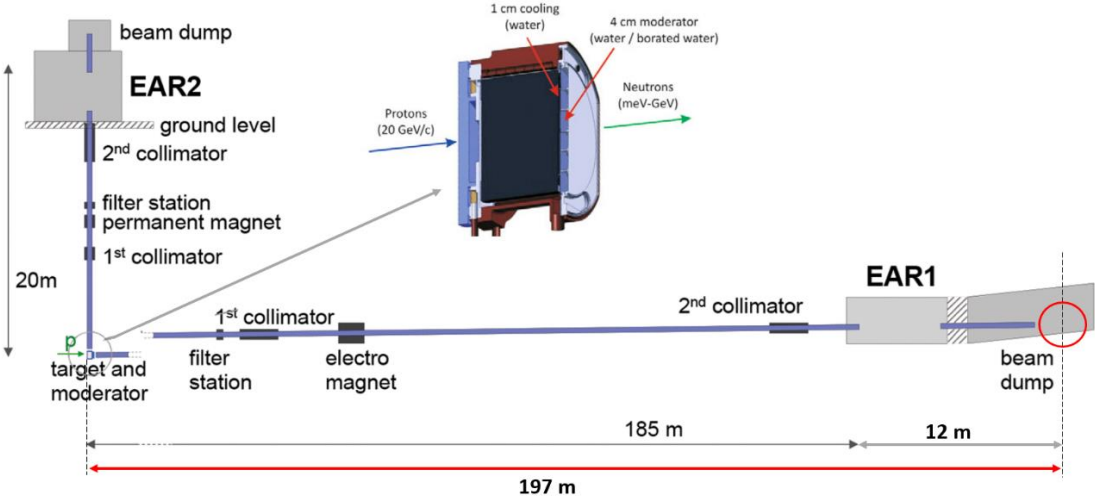
**Figure 44:** Schematic layout of the n_TOF facility with the two experimental areas and their relative distances to the target composed of a moderator to produce lower energy neutrons.

The spectrum of neutron beams produced at n_TOF extends in various orders of magnitude, ranging from 0.01 eV to about 1 GeV. Figure 45 depicts the neutron fluxes per unit of lethargy, characteristic of EAR1 and EAR2 experimental areas [51].
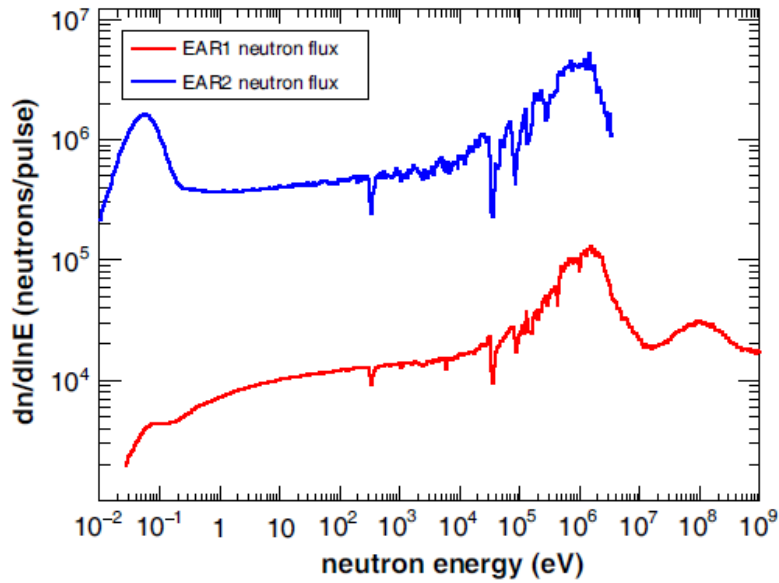
Figure 45: Neutron energy spectra on the two experimental areas of the n_TOF facility.

Moreover, n_TOF is characterized by high relative neutron energy resolution (10^{-4} to 10^{-3} $\Delta E_n/E_n$), high instantaneous neutron flux (> 10^4 n/cm^2/s), and beam transverse extension corresponding to a 0.7 cm [52]. I performed the measurements in a position located downstream to the EAR1 station, where the beam arrives after a flight path of 185 m. In particular, the experimental set-up was installed in the "beam dump" experimental area located at 12 m from the EAR1 and 197 m from the neutron production target [53]. Also, in this case, the control and data acquisition were performed through the Katherine module and the software package MMtrack. Again, the Katherine control module was placed remotely not to expose the electronics directly to the neutron beam. The module was connected through an ethernet cable to a laptop PC placed in the same dump area but far away from the beam. Diamondpix has been placed on a remotely controlled linear stage in front of the vacuum tube (Figure 46).
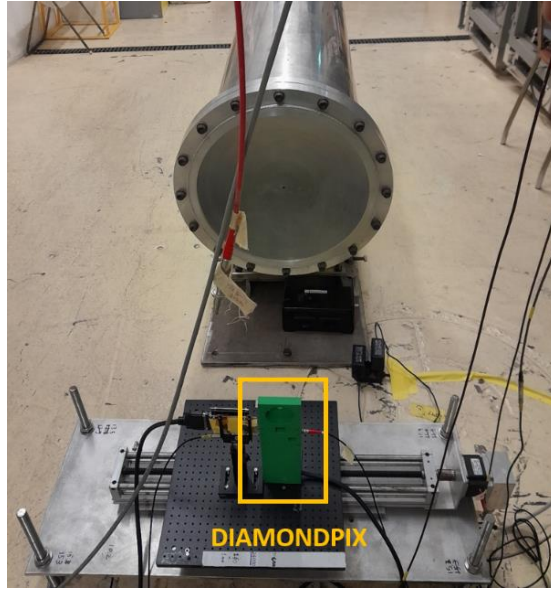
Figure 46: Experimental set-up with Diamondpix mounted on a plastic support at the end of the beam pipe in the dump area.

Also, for these measurements, the Diamondpix has been biased at 300 V, and the experimental runs were performed in data-driven mode by setting ToA&ToT acquisition mode and the Ikrum parameter equal to 5 (Figure 47).
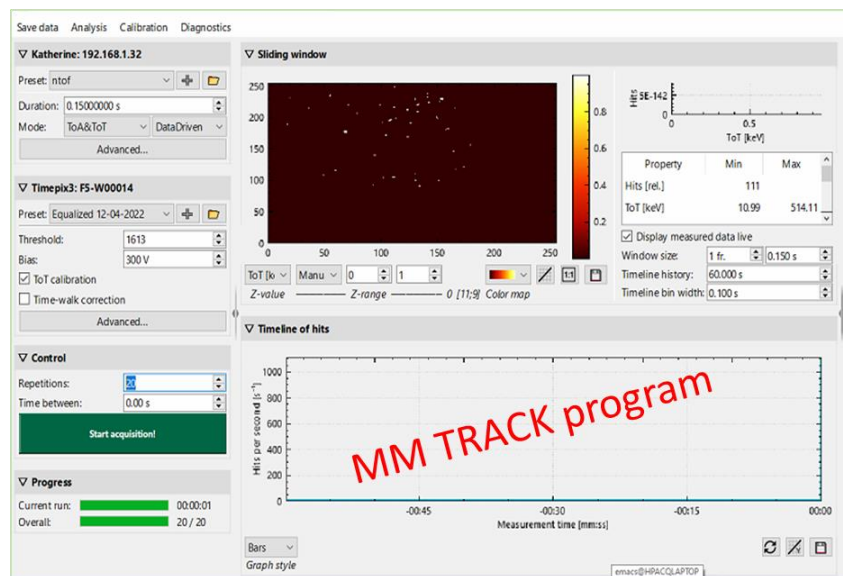

Figure 47: Control panel of the MMTrackLab software used to set acquisition parameters and acquire data. It provides a real-time screen and a track-counting 1D plot.

Acquisitions have been triggered by the standard trigger signal used as reference on the n_TOF facility. The time width of each single acquisition was set to 150 ms to cover the neutron energy range from 1 GeV to 1 meV. As a standard procedure, after a new installation of a Timepix3, the detector was subjected to a threshold equalization and noisy pixel masking procedure, as described in the previous chapters, obtaining the optimal working threshold value and a revised mask of the noisy pixels. Data acquisition took place for two weeks before the end of November 2022. I committed to following up on the acquisitions and launching new acquisitions repeatedly throughout the 24 hours each day.

5.2.1 Time of flight measurements with Diamondpix

As mentioned in the previous paragraph, Diamondpix was triggered and it acquired in data-driven mode with a time window of 150 ms. The detector support was mounted on a linear stage that allowed to scan its transverse position across the neutron beam to maximize the neutron flux on the diamond detector. After this scan, an optimal position was reached and maintained for all the experimental campaigns. The cumulative distribution of the track centroids shows that the Diamondpix area is misaligned to the neutron beam, exploiting a fraction of the beam flux (Figure 48). This configuration was preferred to avoid overloading the diamond TPX3 surface. In data-driven mode, each pixel has a dead time of approximately 470 ns. However, this time can be increased depending on the number of switched-on pixels on the matrix. This behavior can be a drawback in time-of-flight measurements. In this configuration, the effect of dead times was practically negligible.
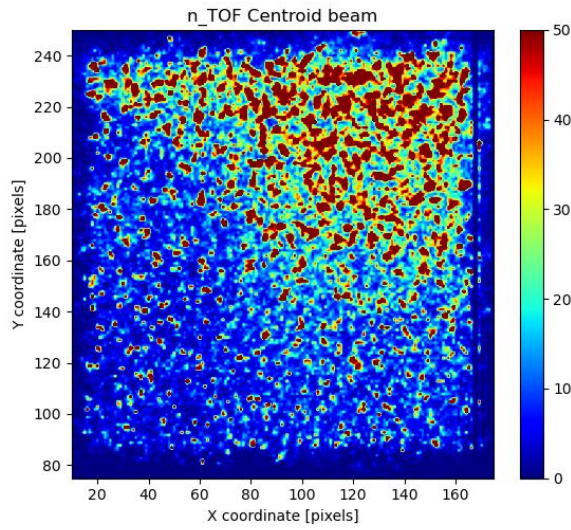
Figure 48: Cumulative 2D image of the track centroids.

Diamondpix is exposed to all the n_TOF neutron spectrum for each trigger signal, and the typical track distribution on the diamond appears as in Figure 49.
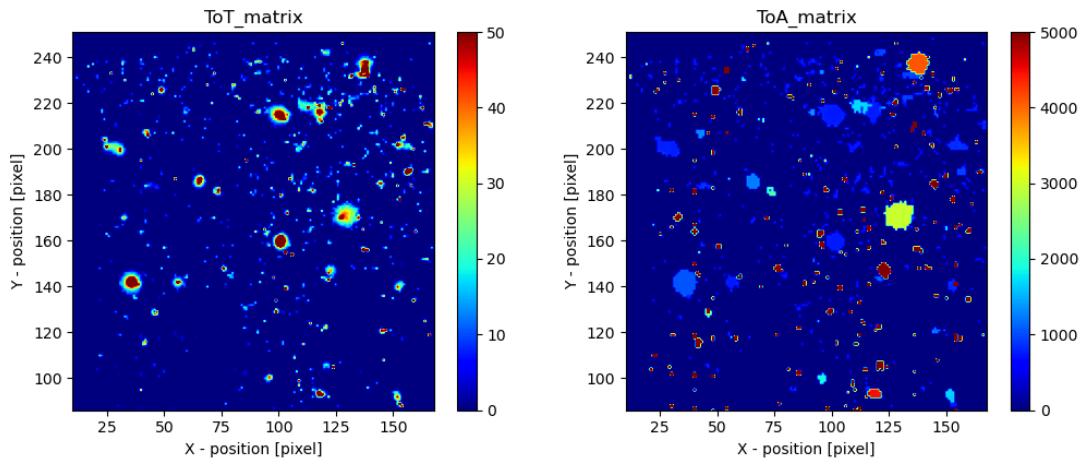
Figure 49: 2D visualization of registered ToT (left) and ToA (right) tracks after a single trigger.

In Figure 49, different track morphologies can be observed. In particular, the typical blob-shaped tracks observed for neutrons on the FNG facility and the long-shaped

tracks produced by gamma particles can be seen. The corresponding matrix with ToA values highlights that most of the long-shaped tracks produced by gammas are registered with a lower time than the neutron tracks. The heavy presence of gamma tracks is due to the gamma flash, which is a prompt burst of gamma rays emitted from the spallation target. It must be pointed out that the main trigger used in the n_TOF experimental areas occurs in advance of the interaction of the proton beam with the n_TOF target. In order to obtain a complete ToF measurement, all the tracks with CS > 3 were considered. This single cut is set to exclude some noisy pixels that can give rise to spurious values of both ToT and ToA. Then, for each track, the first registered ToA values were considered as a measurement of the track's arrival time. After a cumulative operation on 35 acquired files, each one collecting about 3000 triggers, the cumulative histogram of the first ToA times was obtained (Figure 50).
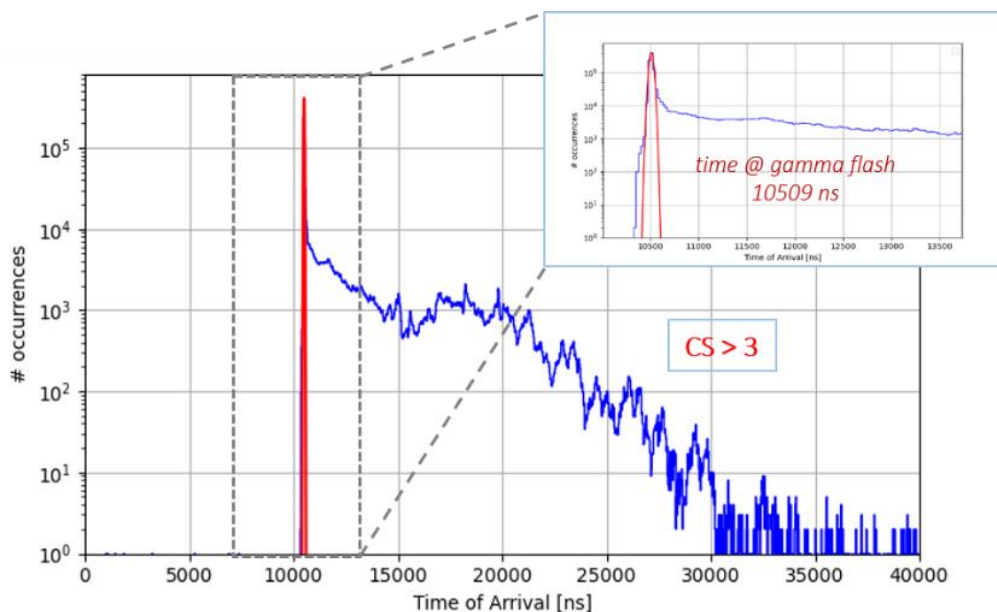
Figure 50: The time of arrival spectrum has been obtained as a histogram distribution of all first ToA values of the tracks. The peak due to the gamma flash is identified with events in the 10509 +/- 23 ns arrival time window for both dedicated and parasitic beams.

This measurement provides a first significant indication for reconstructing the neutron time-of-flight spectrum. As shown in Figure 50, the first single higher peak is evident due to the gamma flash. In addition, these results highlight that until the last days of run, no significant difference between the dedicated and parasitic beams was observed, and a single reference gamma peak can be considered. It must be noted that during the n_TOF beam runs, a parasitic beam is also exploited in addition to the dedicated proton beam. The parasitic beam always comes from the PS accelerator but is less intense. A Gaussian fit to the gamma flash distribution provides a peaked central value of 10509 ± 23 ns. This time confirms the expected delay with respect to the trigger. It provides the zero reference value to calculate the neutron energies through the ToF. As the distance of the detector from the neutron source is 197 m (L), this zero reference value has been set equal to the time Δt that the photons take to cover this distance. The measured ToF of the neutron of mass m_n, which crosses the distance L, determines the neutron kinetic energy (E_n) and its velocity ($v = L/ToF$). Taking into account all these parameters, the relativistic relation for the neutron kinetic energy is given by the following expression:

$$E_n = E_{tot} - m_n c^2 = mc^2 \, (\gamma - 1) = m_n c^2 \left(\frac{1}{\sqrt{1 - \left(L / \left(ToF \cdot c \right) \right)^2}} - 1 \right)$$

where $\gamma = (1 - v^2/c^2)^{-1/2}$ is the Lorentz factor, m_n is the mass at rest of the neutron, and c is the speed of light. Consequently, the energy spectrum of neutrons (Figure 51) has been reconstructed from the ToF distribution. It is based on the integration of at least 10000 triggers, while a lower time cut of 700 ns has been set in order to exclude the gamma flash and the high-energy neutrons close to it, whose signals can be confused with gammas. It must be noted that Diamondpix has to be characterized in the energy

range of interest for nuclear fusion (1–20 MeV), and higher energy neutrons will not be considered.
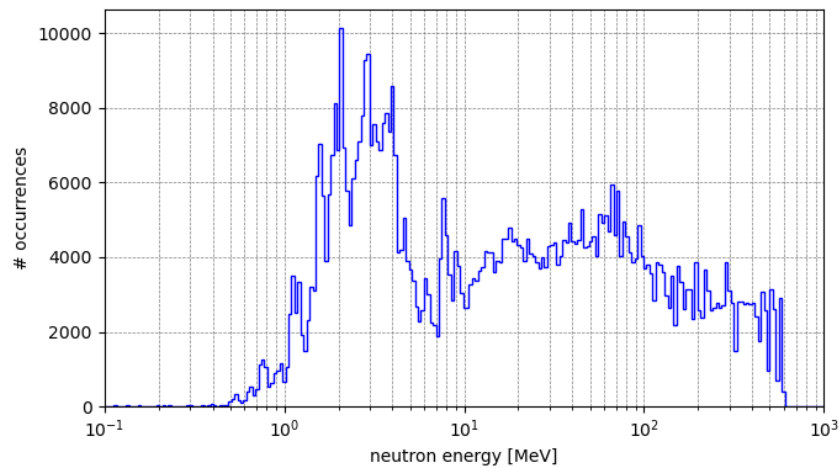
Figure 51: The time-of-flight spectrum reconstructed by Diamondpix from ToA measurements. Neutron energy is expressed in lethargy units.

The energy spectrum highlights that no tracks have been observed below 0.5 MeV. The most populated energy range extends from 1 MeV to 8 MeV, with some peaks. A broad lower continuum extends to 600 MeV. This spectrum is strictly correlated with the interaction mechanisms of fast neutrons, according to the reactions shown in Table 4, and their cross-sections (Figure 52).
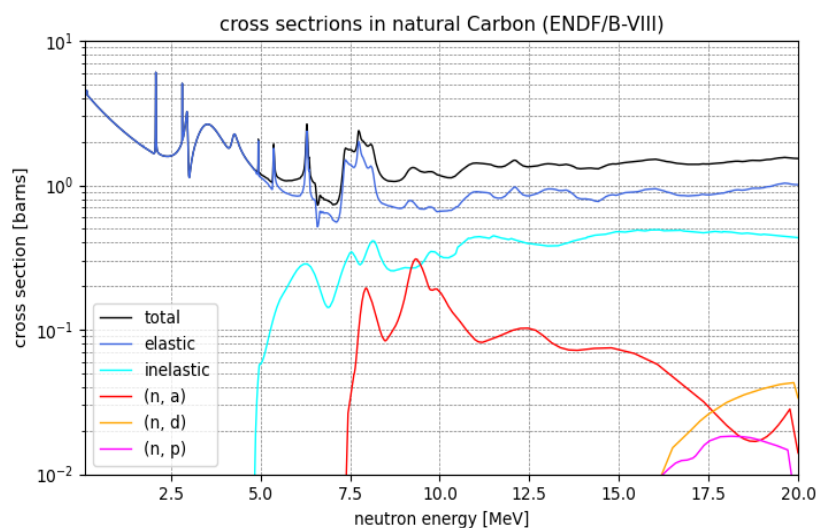
Figure 52: ^{12}C total cross-section with the main particular cross sections for inelastic interactions and for alpha, deuteron, and proton reaction products in the energy range from 1 to 20 MeV.

Figure 48 plots the cross-section values from the ENDF/B-VIII database in the energy range of interest for the main neutron reactions. The elastic interactions with carbon ions contribute to the total cross section even over the energy threshold of the inelastic and charged particle reactions. The reconstructed ToF spectrum represents a fundamental starting point for the analysis of the next measurements because, as it will be shown, it is possible to select specific energy ranges and study corresponding detector responses. ToF reconstruction based on the measured distance is insufficient because there can be some additional effects on measured times due to cable connections and ToA response. The time-walk effect [54,55] is the main one and can have a non-negligible impact. This last effect has been considered and evaluated. Results, however, show that it can be considered negligible. After evaluating this instrumental effect, a valid confirmation of the correct ToF reconstruction comes from comparing the total cross-section trend with the measured ToF spectrum (Figure 53).
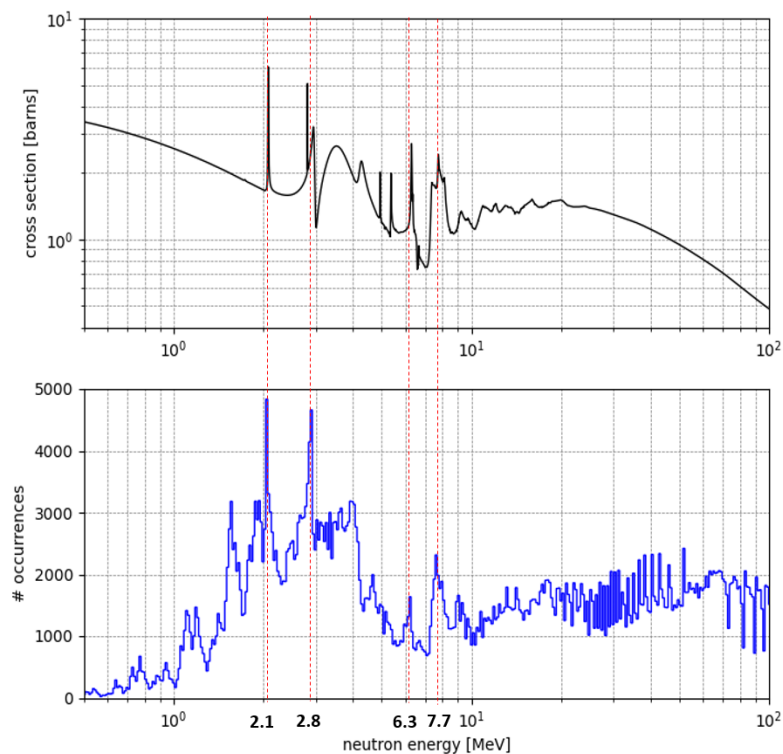
**Figure 53:** Comparison between the 12C total cross section and the ToF spectrum measured by Diamondpix. Neutron energy is expressed in lethargy units. Dashed red lines show the correspondence between some cross-section resonances and experimental peaks.

Many of the observed peaks on the spectrum measured by Diamondpix correspond to well-defined resonances on the plot of the total cross section plot for ^{12}C. This also represents a significant result of the data analysis, as it highlights the contribution of the main cross-section resonances to the reconstructed spectrum.

5.2.2 Track analysis at different neutron energies

As explained in the previous section, the ToF spectrum obtained on the n_TOF facility allows for a more refined analysis of the detector response. In particular, some specific cluster parameters can be studied as a function of specific neutron energies. This paragraph will investigate the distributions of some of the CS and Rnd parameters as a function of different energy ranges. The study of charge response will be treated in subparagraph 5.3.1 after Diamondpix energy calibration is performed. The histograms of morphological CS and Rnd parameters are plotted in Figure 54, separately for five energy bands of neutrons ranging from 2 to 20 MeV.
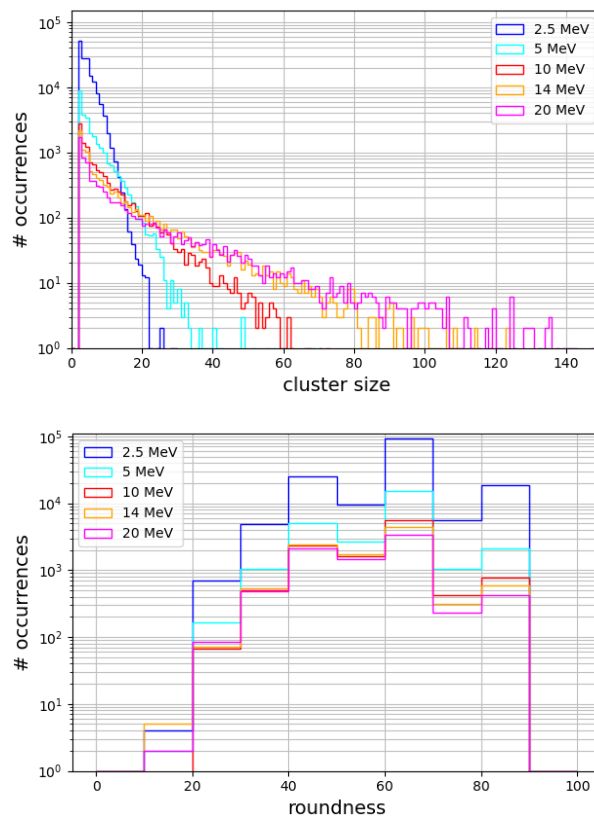
Figure 54: CS (upper) and Rnd (below) distributions at different neutron energies.

All the histograms have been obtained, excluding all clusters with CS = 1 to cut out noisy pixels (Figure 63). Two main effects can be observed on the two distributions: the population of CS shifts towards higher values. In contrast, the Rnd distributions remain mostly unchanged. This behavior for CS is correlated with the increasing value of the energy delivered from neutrons to charge products, particularly carbon ions, with a consequent increasing amount of released charge. Consequently, the effect of Coulomb repulsion becomes stronger and, together with charge diffusion in the diamond, generates a spread of charge over more pixels. In addition, it is expected that, for neutrons energies higher than 6.18 MeV, there is also a contribution from the α, ^{9}Be reaction products, which adds to the predominant carbon ions interactions. Then, at neutron energies higher than 7.89 MeV, the contribution of the 3α products is further added. The higher the charge, the higher the electrostatic repulsion and the larger its diffusion in diamond. No gamma cut has been applied in the present analysis because these results are intended to include all the particles. More energetic gamma photons are expected to produce longer tracks in terms of CS. Consequently, CS increases statistically, and its distribution exhibits tails that become longer and longer at high values. This behavior has been quantified by calculating the mean value of each distribution and studying the trend of the mean values as a function of neutron energy (Figure 55).
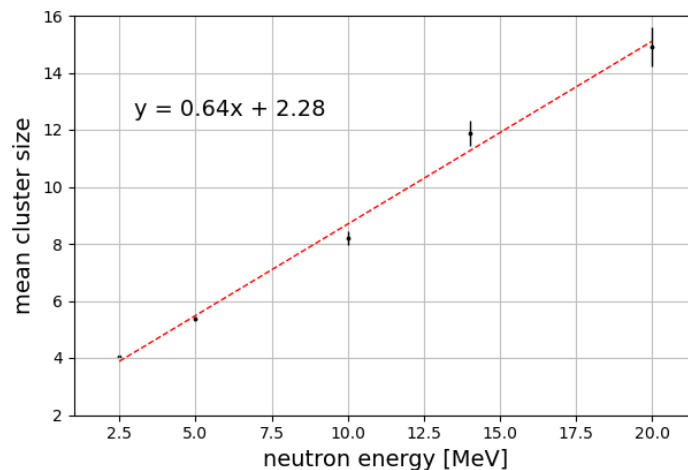

Figure 55: Mean CS values as a function of neutron energies with a linear fit. Errors have been calculated as three times the standard error of the mean.

As can be observed, the mean CS values follow a linear trend in the analyzed energy ranges. This data justifies the line cut values applied to the data for 2.5 MeV neutrons for the FNG measurements. In fact, according to the fit shown in Figure 55, the mean CS at 14 MeV is about three times the mean CS at 2.5 MeV. Therefore, following this indication, the maximum CS cut defining the cut line in subparagraph 5.1.2 has been reduced to 7, which is about one-third of 20. On the other hand, as the distributions of Rnd have not significantly changed, the x-axis value of Rnd has not been changed.

5.2.3 Energy calibration of Diamondpix

As shown in the previous chapter, energy calibration for higher energies follows a different linear trend from that obtained with x-rays at low energies. Therefore, a calibration with alpha particles has been obtained to detect heavy particles such as alpha particles and tritons. A similar method has been applied to Diamondpix, but no clear peak has been obtained in the ToT distribution. This result was expected due to two main reasons: the presence of the gold electrode layer and the polycrystallinity of diamond, which probably affects the interactions on the first layers in contact with gold more severely. The gold layer is non-uniform, as shown by X-ray measurements in a previous work. It is a high Z material and it slows down the incoming alpha particles differently from point to point. In the second case, it must be considered that alpha particles coming from the outside interact in the first tens of microns. The charge must then be transported along the entire thickness of the diamond (500 μm). However, the *ccd* is limited to a maximum value of 300 μm for this type of diamond. Consequently, an indefinite amount of the original charge is lost during the transport. An alternative procedure was obtained by studying the charge response in terms of ToT volume for neutron energies lower than 6.2 MeV by selecting neutron energies from 1 to 5 MeV with step 1 (Figure 56).
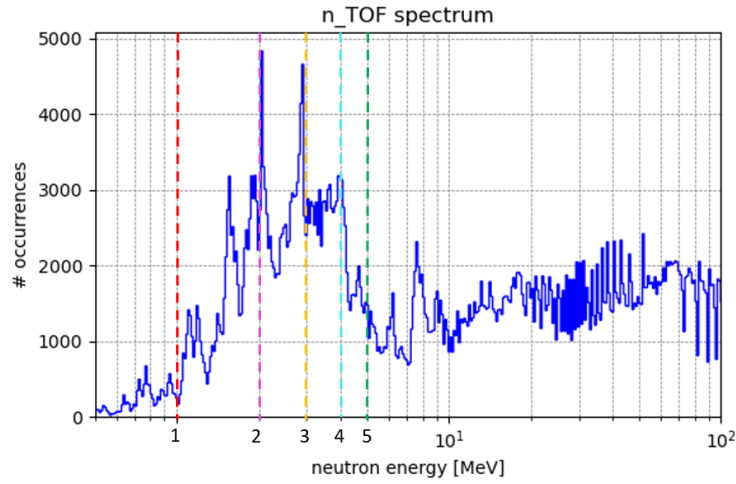
Figure 56: n_TOF spectrum measured with Diamondpix for five selected neutron energies.

Charge response analysis demonstrated a useful correlation between the incident neutron energies and the energies deposited by the recoiling carbon ions. According to the cross-section values, the elastic scattering reaction is the only significant contribution for energies lower than 5 MeV. Some characteristic shoulder distributions are observed by selecting lower energy ranges (1, 2, 3, 4 and 5 MeV). The gamma background is discriminated against in this range of energies, as discussed in the previous paragraph. The line defining the half-plane containing the neutron tracks has different slopes depending on the neutron energy. In must be pointed out that, for the maximum considered value of 5 MeV, there is also the contribution coming from the inelastic scattering reaction on ^{12}C, but its cross section is about one order of magnitude less that the elastic cross section on ^{12}C. The ToT distributions appear as asymmetric histograms with long tails proportional to the incident neutron energy (Figure 57). In order to find the maximum ToT values, the leading edge of these distributions was fitted with the following function:

$$F(ToT) = A + q \cdot ToT + \frac{B}{(1 + exp[(ToT - ToT_0)/C])}$$

The coefficients A, q, B, ToT_0 and C were determined by fitting the experimental data

and ToTv $_{max}$ has been calculated by setting the function F(ToT) equal to 1.
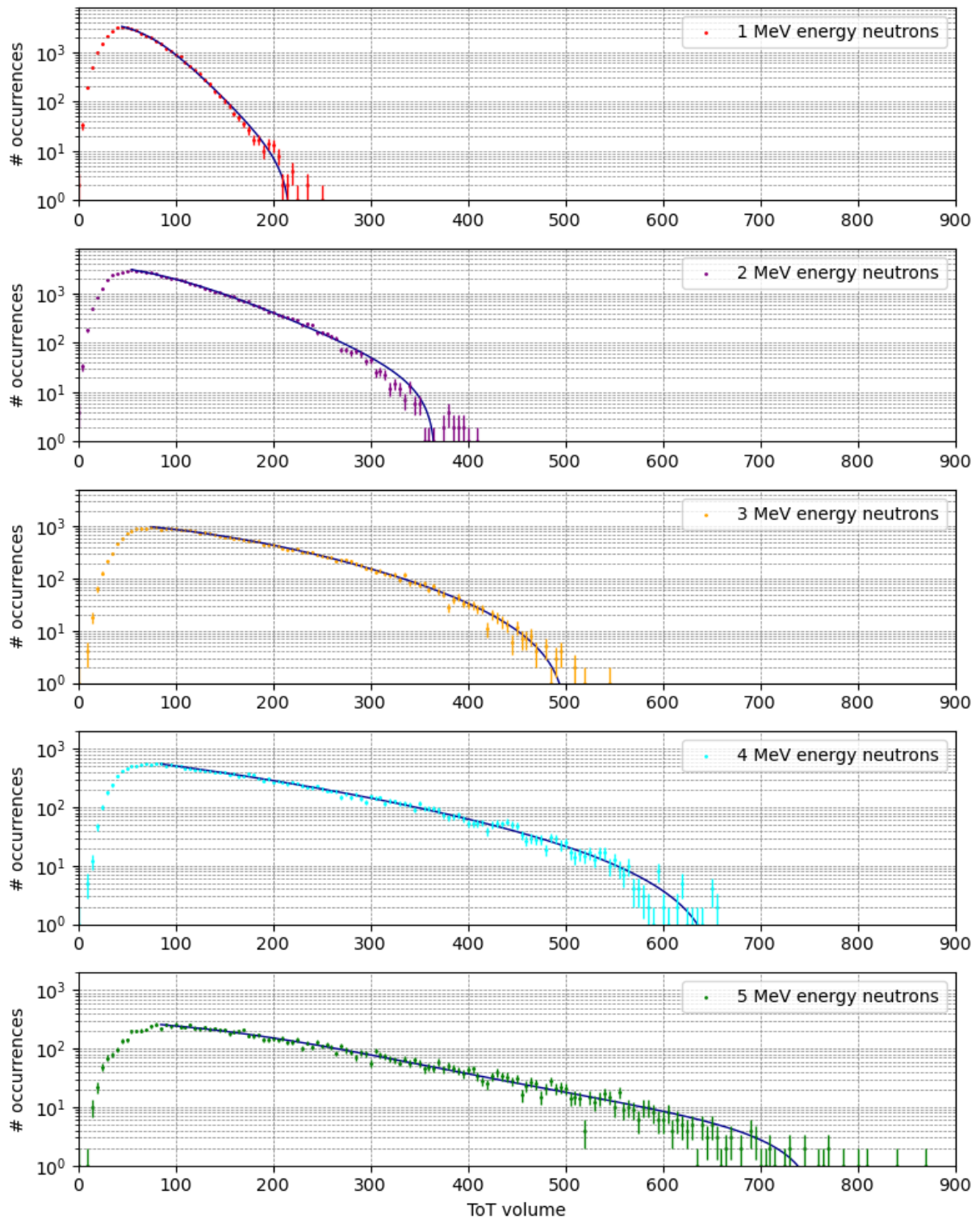
Figure 57: ToT distribution at five neutron energies selected from the measured n_TOF spectrum. For the first four values, the neutron energies range from -0.25 to +0.25 MeV to the specified value. For the last value, the range is from -0.5 to +0.5 to increase statistics. The fits also show the estimated maximum ToT values.

As observed, the maximum measured charge in ToTv increases proportionately to the neutron energy. As expected, these distributions follow the statistical distribution of energy released by recoil carbon ions. The kinetic energy of the ion (E_c) is related to the neutron energy (E_n) and the neutron scattering angle (θ) by the following well-known scattering relation:

$$E_C = \frac{2m_n M_C}{(m_n + M_C)^2}(1 - cos\theta)E_n$$

where $m_n \approx 940.6 \, MeV/c^2$ and $M_C \approx 11{,}187.9 \, MeV/c^2$ are the masses at rest of a neutron and carbon ion, respectively. The maximum recoil energy is obtained for a backscattering neutron recoil ($\theta = 180°$) and, in this case, the kinetic energy of the carbon ion is $E_C = 0.284 \cdot E_n$. The maximum ToT value is expected to correspond to the maximum recoil energy. Then, it is possible to obtain a charge calibration curve based on the correlation between the maximum measured ToT versus the maximum energy recoil of carbon ions, as shown in the plot of Figure 58.
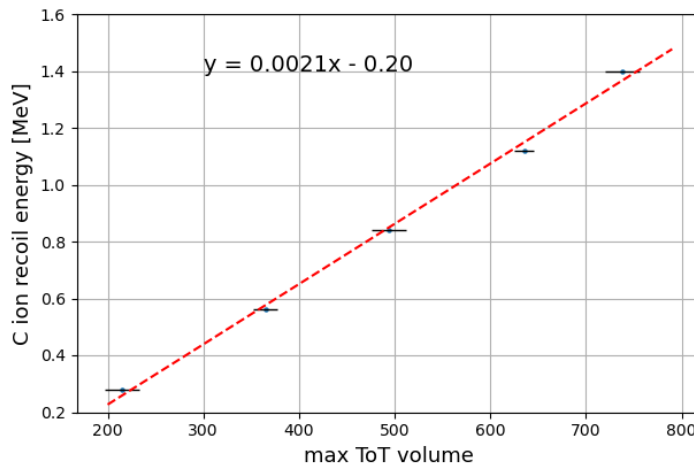
Figure 58: Maximum recoil energy of ^{12}C ions versus maximum measured ToT values. The linear fit provides an energy/ToT calibration curve. Errors have been calculated as the standard deviation of the mean of all ToT values with single occurrences around the maximum ToT value calculated using the fit function.

This procedure provides a calibration curve for higher charge values like for the standard semiconductor Timepixes with alpha particles.

## 5.3 Analysis of the Diamondpix charge response

An important point to focus on is the charge response of the Diamondpix to different neutron energies, particularly the energies of interest in fusion research (2.5 and 14 MeV). For a neutron source such as a tokamak plasma, time-of-flight (ToF) measurements are not possible, and the detector response must be studied at defined neutron energies in terms of track morphology and charge. Consequently, neutron spectrum reconstruction is complicated and often based on unfolding a set of detector responses to different neutron energies. In this work, it is necessary to verify if the charge detector response, after the above-defined cuts, is reproducible and if it is possible to identify specific reactions $^{12}C(n,3\alpha)$ and $^{12}C(n,\alpha)^9Be$ that can further improve the charge response of Diamondpix, in particular the second reaction.

5.3.1 Comparison between FNG and n_TOF results

In order to check the reproducibility of the detector charge responses, at least in terms of the maximum measured values, and to acquire further feedback on the experimental results obtained with the FNG and n_TOF neutron sources, a comparison of the charge response profiles at the two defined energies of the FNG facility was performed. Figure 60 shows the comparison at 14 MeV after the appropriate cuts were applied in the CS versus Rnd plane, as explained in paragraph 5.5.2. In this case, however, the FNG spectrum (Figure 59a) has a mean value that is higher than the nominal value because neutrons receive an additional energy contribution from the deuteron beam.
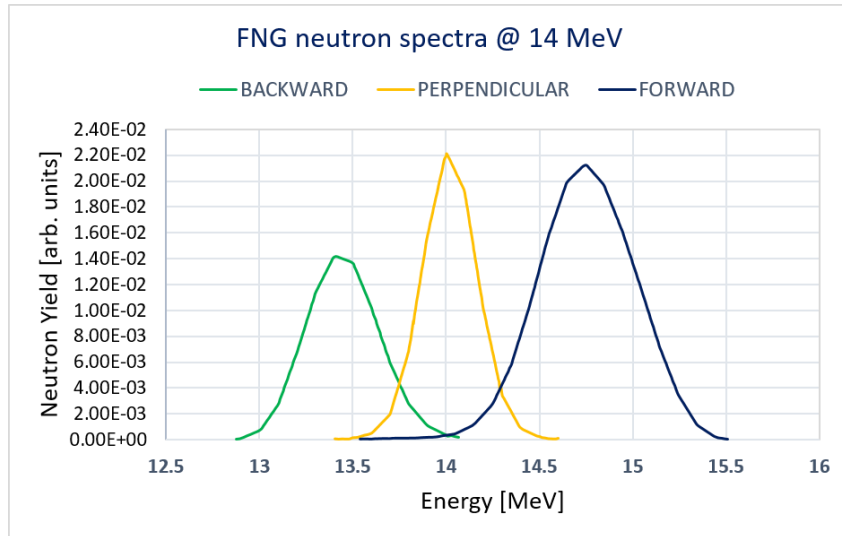
(a)
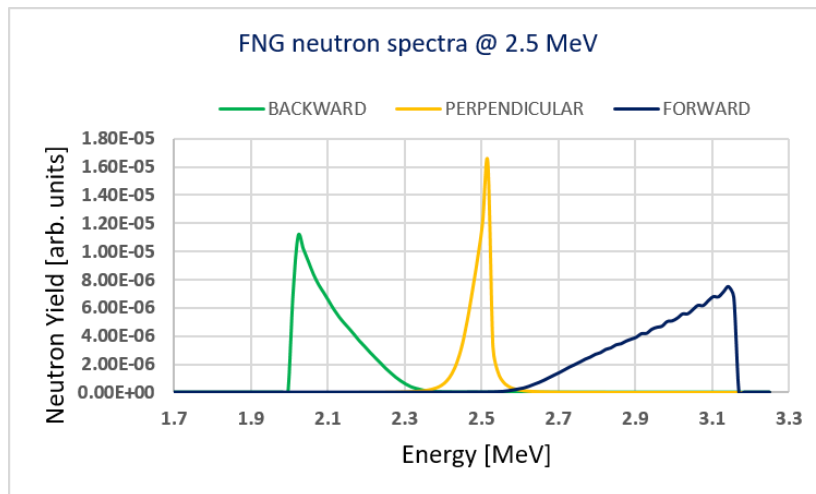
(b)

Figure 59: Measured neutron spectra at the FNG facility in the forward, perpendicular, and backward positions with respect to the accelerated deuteron beam for 14 MeV (a) and 2.5 MeV (b) neutron energies.

As can be observed, the spectra are Gaussian with different full widths at half maximum (FWHMs) and the energy peaks depend on the measurement position. In this case, the Diamondpix was located in a forward position. Then, in order to obtain a more reliable comparison, a similar energy range was selected on the n_TOF

spectrum. The characteristic shoulders of the charge released by neutrons are shown in Figure 60.
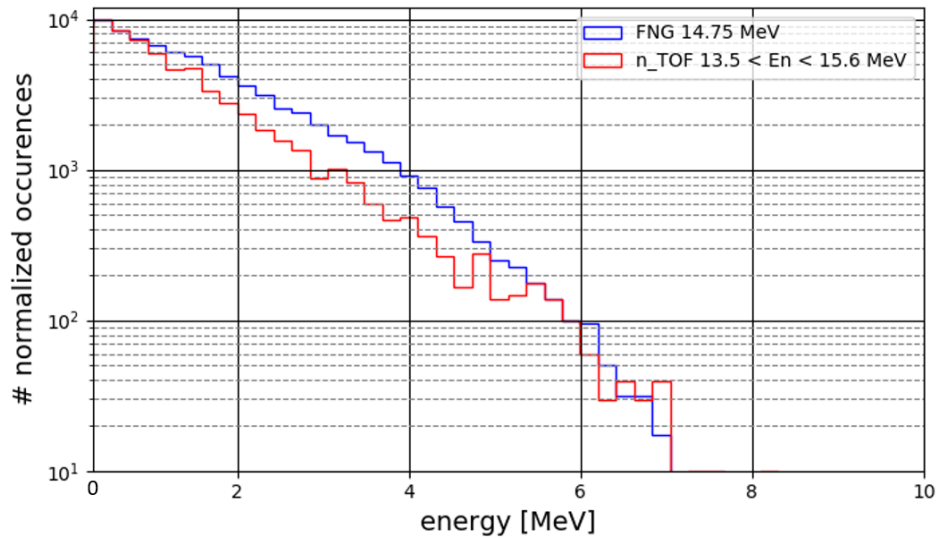
Figure 60: Comparison of the charge responses between the FNG and n_TOF facilities at 14 MeV neutron energy after applying the appropriate line cut to select neutrons.

The comparison shows that the maximum measured energies at the two facilities are consistent. However, a discrepancy can be observed in the energy range from 1 to 5 MeV. These results are expected due to the different shapes of the neutron spectra: Gaussian spectrum for FNG and an almost flat trend for n_TOF. Consequently, different neutron spectra give rise to different charge distributions, even if the energy limits are the same. These results can effectively correlate the charge distribution to the spectrum. This mathematical analysis will be the subject of future studies and will be investigated in the next prototypes. A similar comparison has been performed for 2.5 MeV neutrons (Figure 61). The energy range on the n_TOF data was selected to obtain the optimal matching with the FNG-measured energy spectrum in the forward position concerning the accelerated deuteron beam (Figure 59b).
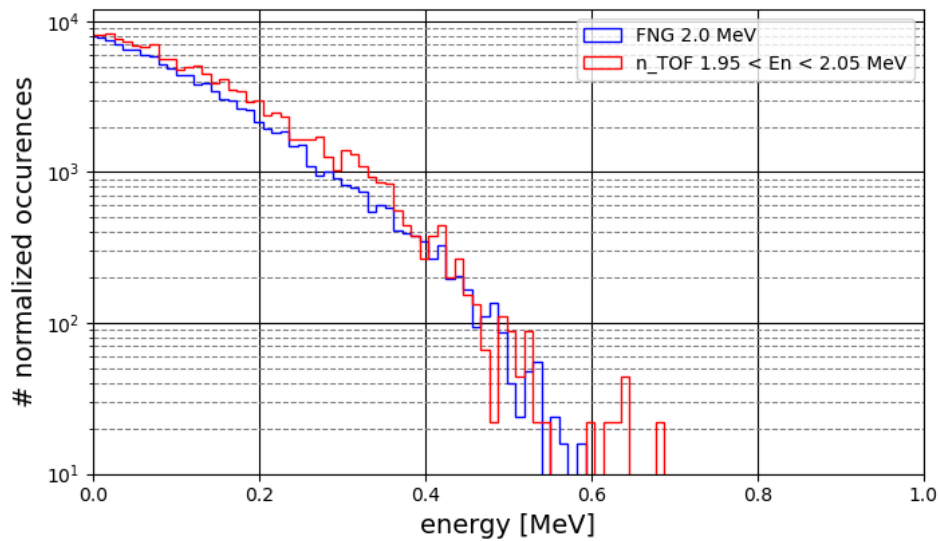
Figure 61: Comparison of the charge responses between the FNG and n_TOF facilities at 2 MeV neutron energy after applying the appropriate line cut to select neutrons.

As can be observed, the best-measured energy spectrum corresponds to a neutron energy of 2 MeV, about 0.5 MeV lower than the expected value of 2.5 MeV. This observed difference is justified by the operational condition of the accelerator that produced deuteron beams with an energy of 200 keV, a value lower than the conventional one at about 300 keV that produce neutrons at 2.5 MeV or higher. As a consequence, the produced neutrons have an energy lower than the nominal value of 2.5 MeV. In addition, there can also be the effect of few mm of cooling water around the target that that can further slowdown the neutrons. This effect is more pronounced for 2.5 MeV neutrons because the scattering cross section in water is about one order of magnitude higher than for 14 MeV neutrons.

5.3.2 Analysis of charge profiles and comparison with Monte Carlo simulations

Once the calibration curve has been obtained, it is possible to study the charge response for higher energy neutrons, where some characteristic reactions are expected,

particularly the $^{12}C(n,\alpha)^9Be$ and $^{12}C(n,3\alpha)$ reactions. Figure 62 shows the responses in terms of energy after applying the charge calibration curve. The distributions refer to 2.5, 14, and 20 MeV neutron energy values selected on the measured n_TOF spectrum.
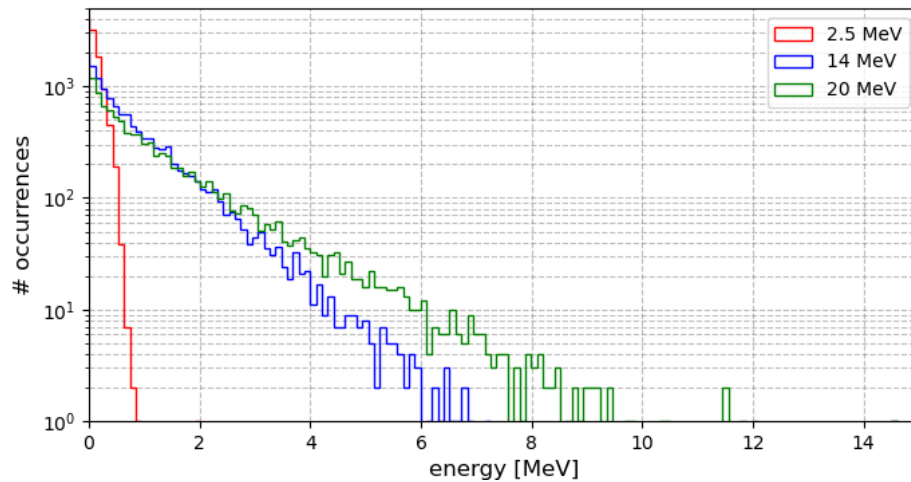
Figure 62: Comparison of deposited energy distributions at different neutron energies. The values have been selected from the measured n_TOF spectrum by selecting an energy range from -1 to +1 MeV with respect to the specified value.

As expected, a general trend of increasing energy is observed due to reaction products. In the case of higher neutron energies, there is also a contribution in addition to the recoil of carbon ions. Regarding 14 MeV neutrons, the maximum energy recoil from carbon ions is expected to be about 3.9 MeV. Therefore, it is expected that higher energy values are due to other reactions. A Monte Carlo simulation with the Fluka code was performed. The main components of the detector were modeled: a 14 × 14 mm2 diamond plate, the chip, and bump-bonding, which were drawn as simple layers of silicon and tin, respectively. The PCB support was modeled as an epoxy board. A more accurate reconstruction was unnecessary to evaluate the possible contribution to the diamond response. According to these simulations, the expected charge response for 14 MeV neutrons is shown in Figure 63.
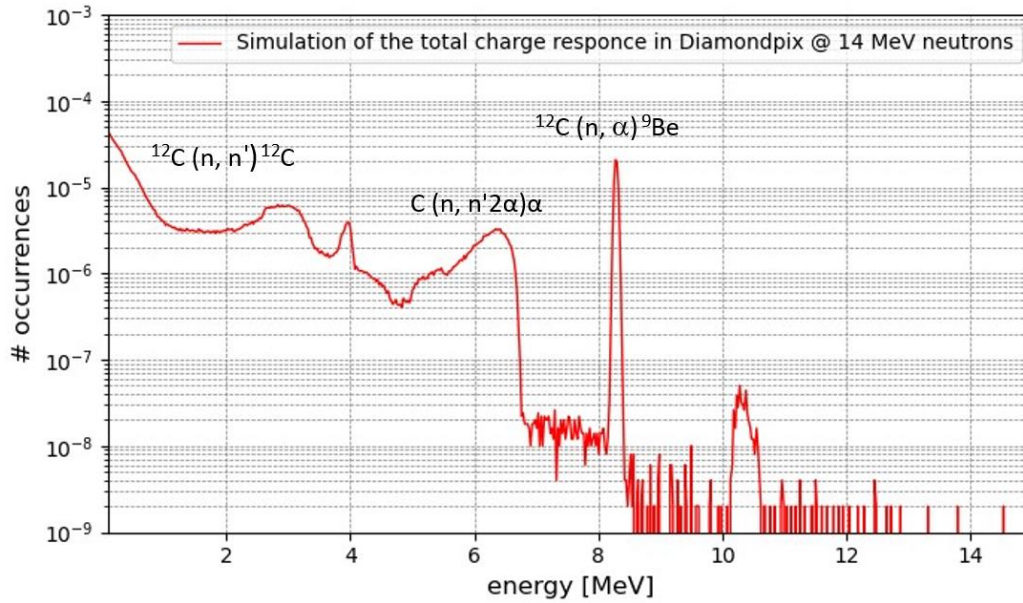
Figure 63: Energy spectrum for 14 MeV neutrons simulated for the Diamondpix and its support. The contributions of the main reactions have been highlighted.

The following expression has modeled the line broadening FWHM(ΔE):

$$FWHM(\Delta E) = a + b\sqrt{\Delta E + c(\Delta E)^2}$$

where ΔE is energy deposition scored at the end of each event. a, b, and c coefficients have been calculated using a standard procedure like for conventional HPGe detectors [56]. In the present case, this procedure involves a plot of the errors of Figure 58 converted to energy units (FWHM) versus the maximum deposited energies of the recoil carbon ions (ΔE). The coefficients a, b, and c are then obtained by fitting this plot with the previous expression. The experimental points are not sufficient to determine with certainty the shape of the fitting function in this energy range. However, the fitting function that was found is consistent with a horizontal line as the main contribution to the measurement comes from the coefficient a (6.4×10^{-5} GeV); the non-

linear part is more important for higher energies even if no data are available in this range. The values found for b and c are 1.2×10^{-5} GeV$^{1/2}$ and 10^{-4} GeV^{-1}, respectively.

As shown in Figure 63, the simulated charge response, after applying the expected line broadening, differs from the measured one, particularly close to the edge values due to the maximum carbon recoil energy (3.9 MeV) and the ^{12}C(n,3α) reaction (about 6.7 MeV). One would expect to observe broadened peaks upstream of edge energy values. However, a continuous decreasing trend is observed. Only the extreme measured values are consistent with the maximum energy value of 6.7 MeV for the 3α reaction. In addition, the expected peak at 8.3 MeV for the ^{12}C(n,α)^{9}Be reaction is not observed. A simulation of the fluence energy spectrum of carbon ions shows that the experimental values follow the trend of the simulated spectrum in the energy range from 0.1 to 3.9 MeV (Figure 64).
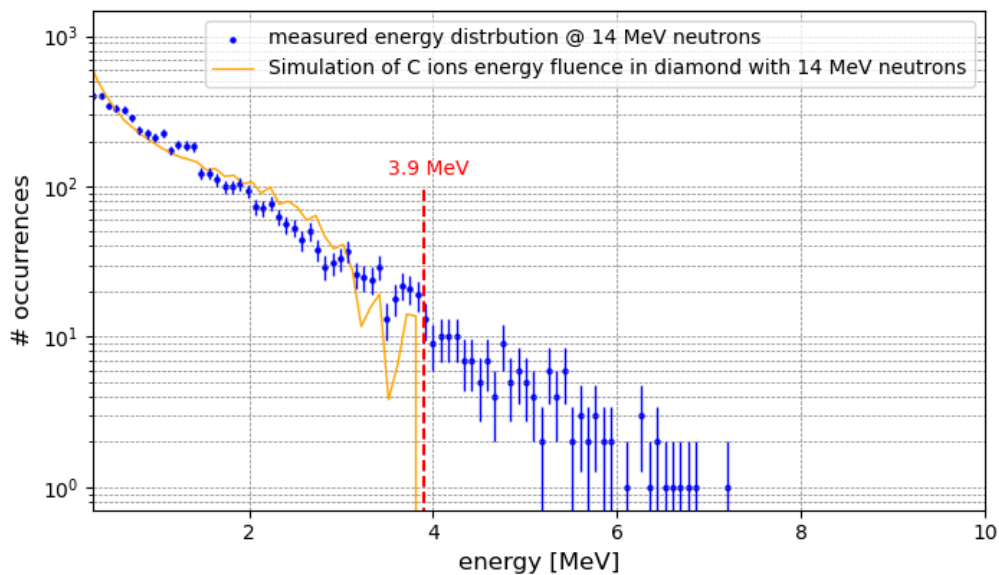
Figure 64: Deposited energy spectrum measured with 14 MeV neutrons and energy fluence simulated for carbon ions only. The red line highlights the maximum recoil energy of carbon ions with 14 MeV neutrons.

These results show that, for higher energy neutrons, the main contribution to the charge response of Diamondpix comes from carbon ion recoils, and the additional

contribution comes from 3α reactions and ^{12}C inelastic reactions. As the ^{12}C(n,α)^{9}Be reaction is not observed, a possible explanation is that Diamondpix probably underestimated the measured charge due to this reaction, and the tracks for this reaction fall in the lower energy-populated region of the 3α tracks (Figure 65).
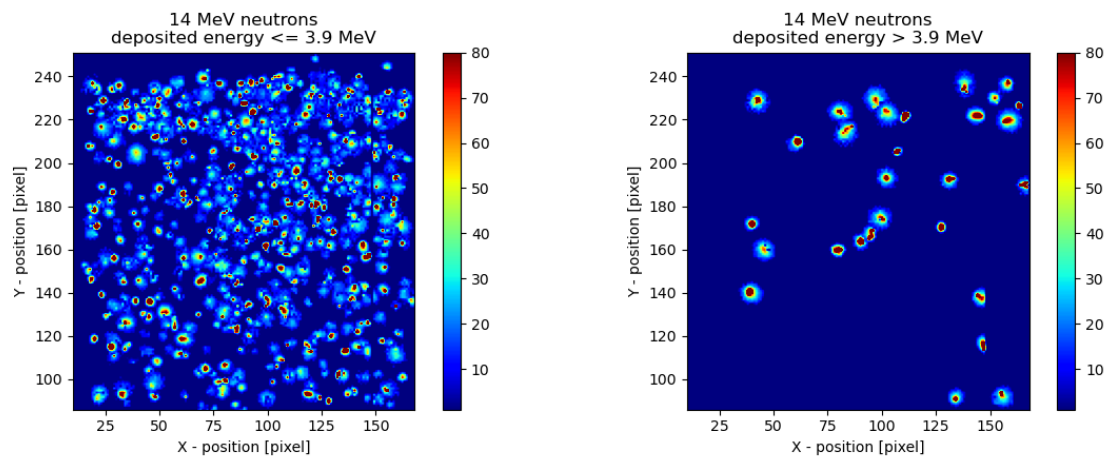
Figure 65: Tracks observed due to 14 MeV neutrons selected on the n_TOF facility after 6000 triggers in the region of recoil energy deposition and the higher energy range.

However, it is important to outline that charge underestimation can also occur for some 3α and carbon inelastic reactions. This behavior is due to polycrystalline diamond: not all pixels transport charge similarly, and some pixels lose a certain amount of charge depending on the local *ccd* characteristics and the electric drift field. In addition, higher energy charges experience greater electrostatic repulsion and, along with charge diffusion in diamonds, are distributed over a larger number of pixels. Therefore, the total measured charge can be underestimated by an amount that cannot be quantified with this type of measurement. Further confirmation of this charge response observed with Diamondpix has been obtained with higher energy neutrons. Figure 66 shows a similar plot after selecting events from the n_TOF data corresponding to 20 MeV neutrons.
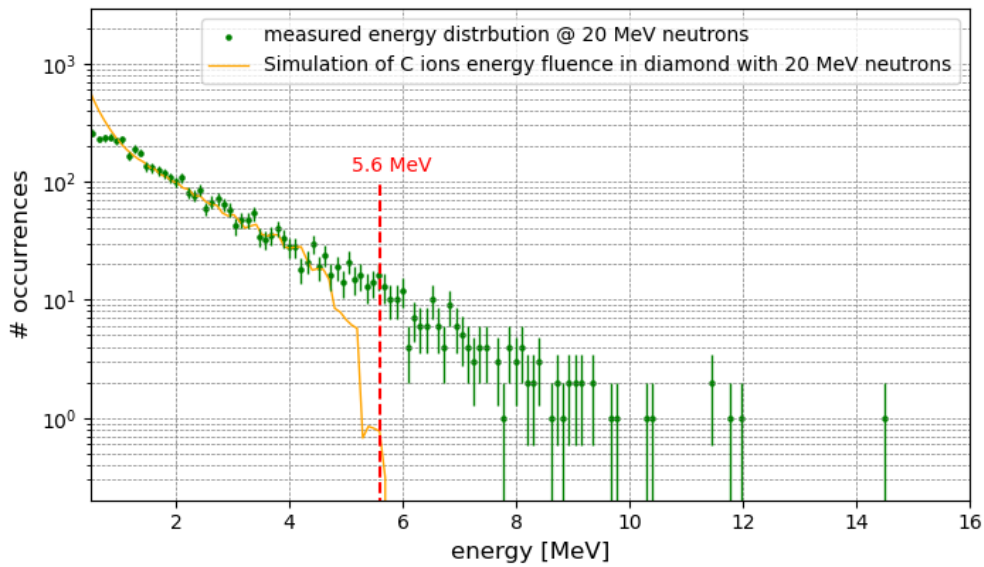
Figure 66: Deposited energy spectrum measured with 20 MeV neutrons and energy fluence simulated for carbon ions only. The red line highlights the maximum recoil energy of carbon ions with 20 MeV neutrons.

As can be observed, again, there is a population of events with energy deposition higher than the maximum carbon recoil energy of 5.6 MeV (Figure 67), and the expected peak for $^{12}C(n,\alpha)^9Be$ reaction at 14.3 MeV has not been observed. Figure 67 shows the tracks due to neutrons with energies less than or equal to 5.6 MeV and greater than 5.6 MeV, respectively.

Figure 67: The observed tracks due to 20 MeV neutrons as selected on the n_TOF facility after 6000 triggers in the region of recoil energy deposition and in the higher energy range.
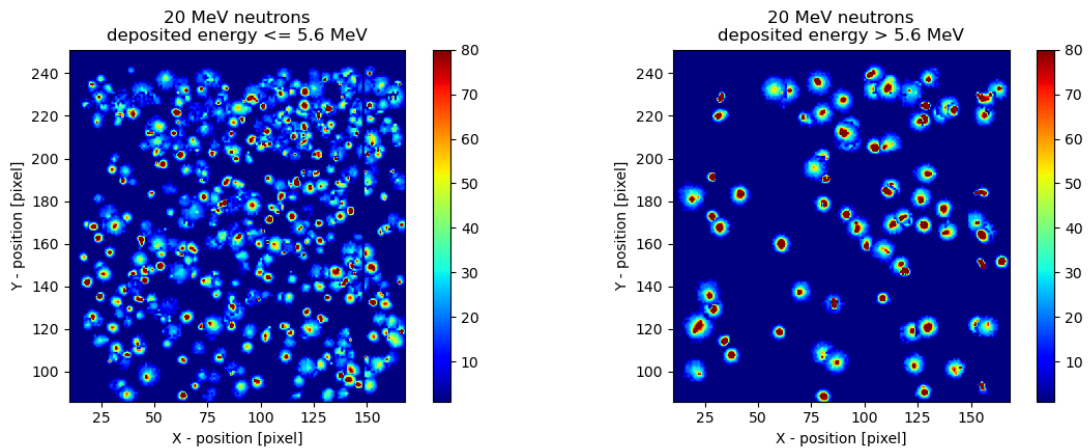
As observed, the expected tracks with higher deposition energies have higher charge sharing (and then higher CS). This means more pixels are involved, with an increasing probability of underestimating the measured charge. Indeed, the maximum deposited energy values are inconsistent with the edge value of 12.7 MeV expected for 3α reactions. This confirms that the detector's measurements become less accurate for higher released charges. Then, a subset of the ^{12}C(n,3α) and ^{12}C(n,n)^{12}C inelastic reactions and all the ^{12}C(n, α)^{9}Be reactions fall into the regions with lower energy deposition. These reactions contribute to the typical observed charge response for neutron energies higher than 6.2 MeV. This is the minimum energy threshold under which the characteristic diamond reaction channels are not triggered.

Chapter 6

Overall summary and conclusions

## 6.1 Summary of the obtained results

This research focuses on characterizing a novel diamond detector based on TPX3 chip technology. In Chapter 3, we delve into the key advantages of TPX3-based test detectors, which offer precise spatial information, charge measurements, and timing data for interacting particles. Specifically, we demonstrate their unique capabilities through two intriguing applications: monitoring radon decay products and thermal neutrons using a ^{6}LiF converter. These applications also highlight the potential of these detectors as track detectors, particularly their ability to discriminate particles through morphological track analysis. Chapter 4 introduces the Diamondpix detector, which pairs a diamond sensor with the TPX3 chip. We have characterized this detector using X-rays, gamma rays, and alpha sources, comparing its performance with the CdTe-based TPX3 detector. This comparison highlights the distinctive characteristics of diamonds as compared to semiconductors, especially in terms of the observed tracks generated by ionizing radiation sources. Chapter 5 shows Diamondpix's potential as a detector for fast neutrons and beam monitoring. A substantial portion of this research is dedicated to data analysis, which involves the implementation of algorithms for track analysis and establishing dedicated criteria for its response to neutrons. We conducted measurements at two facilities: the FNG at ENEA Frascati and the n_TOF at CERN. In the first case, we characterized Diamondpix's response to the characteristic neutron energies from D-D and D-T reactions (2.5 and 14 MeV). A criterion was established to discriminate between 14 MeV and 2.5 MeV neutron and gamma background tracks by defining a specific region in the CS-Rnd parameter space

and applying this criterion the Diamondpix efficiency was estimated. In the second case, we extended the characterization of the response of Diamondpix across the energy range of 1 to 20 MeV, leveraging a spallation source and Diamondpix's ability to measure time with nanosecond resolution. Measurements at the n_TOF facility, hence, exploited the time resolution of TPX3 chip to obtain a time of flight spectrum of the neutrons interacting on the Diamondpix. The reconstructed spectrum has been confirmed by some characteristic resonance peaks and was used to study the Diamondpix response. Additionally, we extended the discrimination criterion to neutron energies derived from the measured Diamondpix time-of-flight spectrum by applying appropriate scaling factors to the CS and Rnd parameters. We also studied ToT distributions for different neutron energies and obtained a linear calibration curve for Diamondpix by selecting neutrons with energies lower than 6.2 MeV, the threshold energy for the ^{12}C(n, α)^{9}Be reaction, which allowed us to exploit only the carbon ion recoil reactions. By fitting the ToT distributions with a function, we obtained a calibration curve associating the maximum ToT values with the maximum energies of the recoil carbon ions. The obtained calibration curve was successfully applied to study the Diamondpix charge response and this was confirmed also by the comparison of the energy deposition spectra between the FNG and n_TOF facilities at 14 and 20 MeV. It was shown that neutrons with energies higher than the 6.2 MeV energy threshold produce a charge response that is also characterized by the 3α reaction, as with single-channel diamonds, but the ^{12}C(n, α)^{9}Be reactions are not observed, unlike single-channel diamonds. This is probably because Diamondpix underestimates the charge, as demonstrated in the 14 and 20 MeV neutrons cases. These last results investigated the characteristic charge response of this type of diamond in detail, revealing both its useful response function due to the presence of additional contribution due mainly to 3α reactions, and its limits due to the fact that it is a polycrystalline diamond, which causes a spread and underestimation of the measured charge. However, despite these expected limits, Diamondpix offers several advantages

in the field of nuclear fusion: not only it discriminates neutron radiation signals from background noise in mixed radiation fields but it also measures the induced signal's time over the threshold (ToT, and consequently its charge) and time of arrival (ToA, and thus its timing) pixel by pixel. With a high count rate capability in the MHz region, Diamondpix offers nanosecond temporal resolution, which is crucial for neutron diagnostics experiments. Lightweight and compact, this detector maximizes neutron counts by safely placing it near the plasma, meeting an essential requirement for fusion reactor neutron diagnostics. The detector provides real-time information with nanosecond temporal resolution, which is indispensable for controlling and protecting fusion reactors. Furthermore, neutron diagnostics can be used to monitor neutron-induced radioactivity in surrounding materials, which helps to ensure the safety of fusion reactors. In conclusion, the results presented here demonstrate the feasibility and energy resolution of the Diamondpix detector, making it valuable for fusion applications. This research also showcases its potential for characterizing neutron beams and studying charged particle reactions induced by neutrons in carbon.

6.2 Realization of the new prototype based on monocrystalline diamond

This initial prototype of Diamondpix was realized with a polycrystalline diamond, which is not the optimal choice for charge measurements. Therefore, following the encouraging results obtained with this prototype and also wanting to exploit the measurement of charge and energy, the production of another prototype with a monocrystalline diamond detector is desirable. The largest available monocrystalline diamond detector will be used; it has a thickness of 500 μm and covers an area of 4.5 × 4.5 mm^2 (Figure 68).
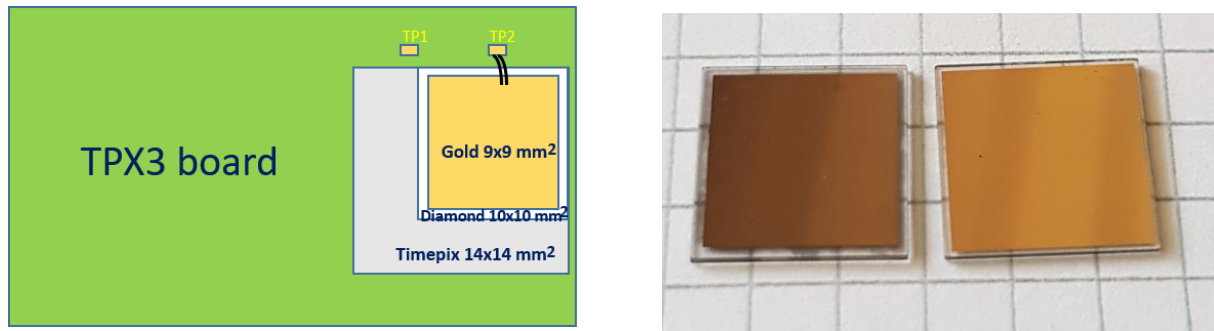
Figure 68: Schematic layout of Diamondpix that highlights the support board, the TPX3 chip, and the area with the diamond covered with the gold electrode.

Once the new prototype with four single-crystal diamonds is available, the detector will be characterized through the study of its quality to evaluate its response in terms of charge collection distance. Laboratory sources such as β, α, or X-ray will be used. Moreover, a pixel-by-pixel energy calibration will be carried out using monochromatic X-ray sources. A study of the detector response to specific neutron energies (2.5 and 14.1 MeV neutrons) will be performed to characterize the detector response to monoenergetic neutrons. Then, it will be interesting to study the detector response to neutrons coming from a tokamak through measurements of the neutron flux to assess its spectrometric capability and apply track analysis. In addition, measuring the neutron flux during the plasma discharge will be helpful to test the rate capability of the electronics and the possibility of using the detector as a feedback system. It will also be essential to test the response stability of the detector because it can be affected by the high radiation levels that are expected close to tokamak reactors.

Additionally, once the capabilities of the pixelated monocrystalline diamond have been demonstrated, and following the production times required, a second prototype can be designed, utilizing a mosaic of single 500 μm mono-crystals to cover the entire 14 × 14 mm² chip area. Similar tests may be carried out for this prototype to verify the quality of the diamond's response over the entire area. However, the primary production technique for artificial diamonds through the CVD process has limitations

regarding the dimensions of spectroscopy-grade crystals: at present, the limit is a few tens of mm^2 in area and a thickness of up to 1 mm. Increased dimensions, in particular thickness, would be important for increasing the efficiency of the detectors. Furthermore, the radiation hardness properties of diamond detector assemblies should be further investigated. A crucial point is the realization of conductive contacts on the diamond: the first tests did not show optimal stability to realize coupling with TPX3 chip. At the moment, a viable and economic alternative is the ACF (Anisotropic Conductive Film) foils [57], a film-type anisotropic conductive adhesive with uniformly dispersed conductive microparticles in heat-curing resin (Figure 69), enabling conduction in the vertical direction and insulation between terminals simultaneously. Heat and pressure are applied to connect two surfaces of interconnection pads; statistically, some conductive balls get stuck, and these crushed particles trapped on the bump surface act as conducting material and assure adhesion between the two parts. Uncoated particles not trapped on the bumps are redistributed between the terminals and fixed in place with a heat-curing binder to prevent short circuits, as shown in Figure 69 [58].
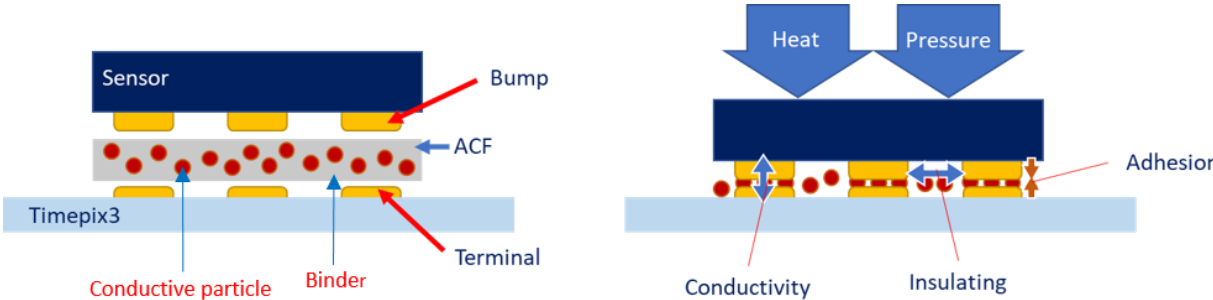
Figure 69: Structure of ACF foil and schematic illustration of the ACF flip chip bonding mechanism.

6.3 Future developments and potential applications in other research fields

Diamond detectors have been successfully used in applications such as: particle beam monitors and trackers, equipment calibration, active exposure monitoring for nuclear applications in homeland security, nuclear reactors, and fusion experiments. In particular, the characterization of the new diamond detector demonstrates its usefulness in applications beyond magnetic confinement fusion. With its high temporal resolution of 1.6 ns, this detector offers significant benefits for magnetic confinement fusion, particularly in neutron detection, time-of-flight measurements in inertial fusion, and neutron beam monitoring at spallation sources. Moreover, it can detect thermal neutrons by adding a conversion layer of ^{6}LiF and B_4C. In materials physics, time-of-flight measurements on thermal neutrons play a crucial role in diffractometric studies. Additionally, this detector can find applications in radiology and radiation therapy for detecting X-rays and γ-rays precisely, facilitating accurate dosimetry calculations. The research work, therefore, enables the development of a simple, radiation-hard, compact device with a small volume, eliminating the need for cooling or additional systems. Furthermore, by combining this detector with a silicon part, it can detect neutrons and gamma particles, hard X-rays, and soft X-rays. These advancements have significant potential for widespread adoption in various commercial applications.

LIST OF MAIN ABBREVIATIONS

TPX = Timepix

H = Hydrogen

D = Deuterium

T = Tritium

P_{br} = *Bremsstrahlung power*

Tokamak = TOroidalnaya KAmera MAgnitnaya Katushka

NBI = Neutral Beam Injection

ToF = Time of Flight

PPAC = Plate Avalanche Counters

C-MOS = Complementary Metal-Oxide Semiconductor

CCD = Charge-Coupled Device

ASIC = Application Specific Integrated Circuit

PCB = Printed Circuit Board

CSP = Charge Sensitive Preamplifier

ToT = Time over Threshold

ToA = Time of Arrival

fToA = fine ToA

Ikrum = Krummenacher current

CdTe = Cadmium Telluride

Si = Silicon

SDD = Silicon Drift Detector

ToTv = ToT volume

CS = Cluster Size

Rnd = Roundness

L = Linearity

ToTh = Cluster height

CVD = Chemical Vapor Deposition

ccd = Charge Collection Distance

MCA = Multi-Channel Acquisition

PSH = Pulse Height Spectrum

PSA = Pulse Shape Analysis

FNG = Frascati Neutron Generation

FPGA = Field Programmable Gate Array

n_ToF = Neutron Time of Flight

BIBLIOGRAPHY

1. Eddington, A.S., *The Internal Constitution of the Stars*, Cambridge University Press (1988)
2. John Hendry, *The Scientific Origins of Controlled Fusion Technology*, Annals of Science (1987)
3. James A. Mahaffey, *Fusion (Nuclear Power)*, Facts on File (2012)
4. Shalom Eliezer and Yaffa Eliezer, *The Fourth State of Matter*: *An Introduction to Plasma Science*, Institute of Physics Publishing (1989)
5. J. A. Bittencourt, *Fundamentals of Plasma Physics*, Springer (2004)
6. J. Freidberg, *Plasma physics and fusion energy*, Cambridge University Press (2010)
7. A. A. Harms, K. F. Schoepf, G. H. Miley, and D. R. Kingdon, *Principles of Fusion Energy: An Introduction to Fusion Energy for Students of Science and Engineering*, World Scientific Publishing Company (2000)
8. E.A. Azizov, *Tokamaks: from A D Sakharov to the present (the 60-year history of tokamaks)*, IOPscience (2012)
9. L. A Artsimovich et al., *Some results of research on high-temperature plasma in tokamaks. In Plasma Physics and Controlled Nuclear Fusion Research,* International Atomic Energy Agency (1968)
10. Mather I. Boulos, Pierre Fauchais , Emil Pfender, *Thermal Plasmas Fundamentals and Applications*, Springer Nature (2013)
11. Gianmaria De Tommasi, *Plasma Magnetic Control in Tokamak Devices*, Journal of Fusion Energy (2018)
12. J. Wesson, *Tokamaks*, Oxford University Press (2011)
13. F. Wagner, *Physics of magnetic confinement fusion*, EDP Sciences - SIF (2013)
14. Matthew Moynihan & Alfred B. Bortz, Fusion's Promise, Springer **(**2023)
15. G. Ericsson, *Advanced Neutron Spectroscopy in Fusion Research*, Journal of Fusion Energy (2019)
16. H. Reimerdes et al., *Assessment of alternative divertor configurations as an exhaust solution for DEMO*, Nuclear Fusion (2020)
17. B. Wolle, *Tokamak plasma diagnostics based on measured neutron signals*, Physics Report (1999)
18. G.F. Knoll, *Radiation Detection and Measurement*, John Wiley & Sons, Inc. (1999)
19. A. Breskin and N. Zwang., *Timing properties of parallel plate avalanche counters with light particles*, Nuclear Instruments and Methods (1977)

20. P. Allé, E. Wenger, S. Dahaoui, D. Schaniel and C. Lecomte, *Comparison of CCD, CMOS and Hybrid Pixel x-ray detectors: detection principle and data quality*, Physica Spectra (2016)

21. D. Pacella, *Energy-resolved x-ray detectors: the future of diagnostic imaging*, Dove Press (2015)

22. T. Poikela, J. Plosila, T. Westerlund, M. Campbell, M.D. Gaspari, X. Llopart et al., *Timepix3: a 65k channel hybrid pixel readout chip with simultaneous ToA/ToT and sparse readout*, JINST (2004)

23. X. Llopart, R. Ballabriga, M. Campbell, L. Tlustos and W. Wong, *Timepix, a 65k programmable pixel readout chip for arrival time, energy and/or photon counting measurements*, Nucl. Instrum. Meth. A (2007)

24. Medipix collaboration (2004). https://medipix.web.cern.ch/medipix/

25. P. Manek, *A system for 3D localization of gamma sources using Timepix3-based Compton cameras*, Master Thesis (2018)

26. F. Caruggi et al., *Performance of a triple GEM detector equipped with Al-GEM foils for X-rays detection*, Nucl. Instrum. Meth. A (2023)

27. G. Claps et al, *Diamondpix: A CVD diamond detector with timepix3 chip interface*, IEEE Transactions on Nuclear Science 65(10), 2743–2753 (2018)

28. P. Burian, P. Broulim, M. Jara, *Katherine: Ethernet embedded readout interface for timepix3*, Journal of Instrumentation (2017)

29. IEAP Software Repository (2021). https://software.utef.cvut.cz

30. J. Jakubek, *Precise energy calibration of pixel detector working in time-over-threshold mode*, Nucl. Instrum. Meth. (2011)

31. A. Tamburrino, G. Claps, F. Cordella, F. Murtas, D. Pacella, *Timepix3 detector for measuring radon decay products*. Journal of Instrumentation 17 (2022)

32. J. Leidner, F. Murtas, M. Silari, *Energy calibration of the gempix in the energy range of 6 kev to 2 mev*, Journal of Instrumentation (2021)

33. M. Sommer, C. Granja, S. Kodaira and O. Ploc, *High-energy per-pixel calibration of timepix pixel detector with laboratory alpha source*, Nucl. Instrum. Meth. A (2022)

34. FLUKA. https://fluka.cern

35. F. Mamedov, P. Cermak, J. Jakubek, K. Smolek, I. Stekl and J. Vlasek, *Measurement of radon activity in air using electrostatic collection to the Timepix detector*, JINST **(**2013)

36. M. Caresana, L. Garlati, F. Murtas, S. Romano, C.T. Severino and M. Silari, *Real-time measurements of radon activity with the Timepix-based RADONLITE and RADONPIX detectors*, JINST (2014)

37. A.Tamburrino et al., *Thermal neutron detection by means of Timepix3*, EPJP, accepted for publication

38. B. Bergmann et al.,*Characterization of the radiation field in the atlas experiment with timepix detectors*, IEEE TRANSACTIONS ON NUCLEAR SCIENCE 66 (2019)

39. P. Burian et al.,*Timepix3 detector network at atlas experiment*, Journal of Instrumentation (2018)

40. A. Sperduti et al., *Results of the first user program on the Homogeneous Thermal NEutron Source HOTNES (ENEA/INFN)*, Journal of Instrumentation (2017)

41. R. J. Tapper, *Diamond detectors in particle physics*, Rep. Prog. Phys. (2000)

42. https://www.e6.com/en/Home

43. M. Angelone and C. Verona, *Properties of Diamond-Based Neutron Detectors Operated in Harsh Environments*, Journal of Nuclear Engineering (2021)

44. M. Pillon et al., *Experimental response functions of a single-crystal diamond detector for 5–20.5 MeV neutrons*, Nucl. Instrum. Meth. A (2011)

45. M. Angelone et al., *Thermal and fast neutron dosimetry using artificial single crystal diamond detectors*, Radiation Measurements (2011)

46. P.Kavrigin, P.Finocchiaro, E.Griesmayer, E.Jericha, A.Pappalardo, C.Weiss, *Pulse-shape analysis for gamma background rejection in thermal neutron radiation using CVD diamond detectors*, Nuclear Instruments and Methods in Physics Research A (2015)

47. Guang-Wei Huang, *High-Performance Single-Crystal Diamond Detector for Accurate Pulse Shape Discrimination Based on Self-Organizing Map Neural Networks*, Advanced Photonics Research (2021)

48. A. Pietropaolo, F. Andreoli, M. Angelone, U. Besi Vetrella, S. Fiore, S. Loreti, G. Pagano, R. Pilotti and M. Pillon, *The Frascati Neutron Generator: A multipurpose facility for physics and engineering*, Journal of Physics:Conf. Series (2018)

49. M. Martone, M. Angelone, M. Pillon, *The 14 MeV Frascati neutron generator*, Journal of Nuclear Materials (1994)

50. https://home.cern

51. F. Gunsing et al., *Nuclear data activities at the n TOF facility at CERN*, The European Physical Journal Plus (2016)

52. C. Guerrero et al., *Performance of the neutron time-of-flight facility n TOF at CERN*, The European Physical Journal Plus (2013)

53. M. Ferrari et al., *Design development and implementation of a neutron irradiation station at the n_TOF NEAR facility at CERN*, Physical Review Accelerators and Beams (2022)

54. D. Turecek, *USB 3.0 readout and time-walk correction method for Timepix3 detector*, Journal of Instrumentation (2016)

55. S. Tsigaridas, *Timewalk correction for the Timepix3 chip obtained with real particle data*, Nuclear Instruments and Methods in Physics Research A (2019)

56. E. Eftekhari Zadeh et al., *Gaussian Energy Broadening Function of an HPGe Detector in the Range of 40 keV to 1.46 MeV*, Journal of Experimental Physics (2014)

57. P. Svihra, *Development of novel single-die hybridisation processes for small-pitch pixel detectors*, JINST (2022)

58. F. Trupp, R. Cibils and S. Goyanes, *Conductive Particles in Anisotropic Conductive Films*, Polymer Science: Peer Review Journal (2022)

Characterization of a new pixelated diamond detector for fast neutron diagnostics on fusion reactors
Ph.D. thesis. Sapienza University of Rome

Version: January the 9th, 2024
Author's email: antonella.tamburrino@uniroma1.it